

# SUPERFLUID $^3\text{He}$ : A LABORATORY MODEL SYSTEM OF QUANTUM FIELD THEORY

V.B. Eltsov<sup>ab</sup>, M. Krusius<sup>a</sup>, and G.E. Volovik<sup>ac</sup>

<sup>a</sup> Low Temperature Laboratory, Helsinki University of Technology, Box 2200, FIN-02015 HUT, Finland

<sup>b</sup> Kapitza Institute for Physical Problems, 117334 Moscow, Russia

<sup>c</sup> L.D. Landau Institute for Theoretical Physics, 117334 Moscow, Russia  
(December 2, 2024)

## Abstract

*The early Universe is believed to have undergone a sequence of very rapid phase transitions. Defect formation in these transitions has been suggested as the source for the anisotropy in the cosmic background radiation and the large-scale structure in the distribution of visible mass. So far controlled laboratory experiments have not been performed on homogeneous second order phase transitions as a function of transition speed and a freeze-out of topological defects has not been convincingly demonstrated. Recently a new phenomenon was discovered in rotating superfluid  $^3\text{He-B}$ : the formation of quantized vortices within bulk superflow in the presence of ionizing radiation. This “mini bang” allows one to explore the superfluid transition within the clean bulk medium on the microsecond time scale. The experiment appears to provide the first quantitative test of the theories on defect formation in a time-dependent second order phase transition. This is one example among several analogies, such as baryogenesis or generation of primordial magnetic fields, where quantized vortices and other defects in the  $^3\text{He}$  superfluids provide a connection to quantum field theory and its applications to cosmology.*

PACS: 67.57.Fg, 05.70.Fh, 98.80.Cq.

## Contents

<b>I</b>	<b>SUPERFLUID <math>^3\text{He}</math> AND QUANTUM FIELD THEORY</b>	<b>3</b>
<b>II</b>	<b>QUENCH-COOLED SUPERFLUID TRANSITION: A MODEL OF DEFECT FORMATION IN RAPID PHASE TRANSITIONS</b>	<b>3</b>
1	RAPID PHASE TRANSITIONS . . . . .	3
2	COSMIC LARGE-SCALE STRUCTURE . . . . .	3
3	KIBBLE-ZUREK MECHANISM . . . . .	4
4	PRINCIPLE OF EXPERIMENTS IN $^3\text{He-B}$ . . . . .	5
a	Experimental outline . . . . .	5
b	Vortex lines in rotating $^3\text{He-B}$ . . . . .	7
c	NMR measurement of $^3\text{He-B}$ . . . . .	8
5	VORTEX FORMATION IN NEUTRON IRRADIATION . . . . .	8
6	THRESHOLD VELOCITY FOR VORTEX LOOP ESCAPE . . . . .	11
a	Properties of threshold velocity . . . . .	11
b	Mechanisms of vortex-ring formation . . . . .	12
7	INFLUENCE OF $^3\text{He-A}$ ON THRESHOLD VELOCITY . . . . .	12
8	KZ INTERPRETATION OF VORTEX FORMATION . . . . .	13
9	BIAS DEPENDENCE OF LOOP EXTRACTION . . . . .	15
a	Experimental velocity dependence . . . . .	15
b	Analytic model of vortex loop escape . . . . .	15
10	CALORIMETRY OF VORTEX NETWORK . . . . .	17
11	SIMULATION OF LOOP EXTRACTION . . . . .	18
a	Initial loop distribution . . . . .	19
b	Network evolution under scaling assumptions . . . . .	21
c	Direct simulation of network evolution . . . . .	22
12	SUPERFLUID TRANSITION AS A MOVING PHASE FRONT . . . . .	25
a	Neutron bubble and heating . . . . .	25
b	Thermal gradient and velocity of phase front . . . . .	26
13	QUENCH OF PREEXISTING VORTICES . . . . .	27
a	Vortices on microscopic and macroscopic scales. . . . .	27
b	Scaling in equilibrium phase transiton. . . . .	28
c	Nonequilibrium phase transiton. . . . .	29
14	IMPLICATIONS OF THE QUENCH-COOL EXPERIMENTS . . . . .	29
<b>III</b>	<b>OTHER ANALOGUES IN QUANTUM FIELD THEORY RELATED TO VORTICES</b>	<b>30</b>
1	THE THREE TOPOLOGICAL FORCES ACTING ON A VORTEX AND THEIR ANALOGUES	30
2	IORDANSKII FORCE . . . . .	30
a	Superfluid vortex vs spinning cosmic string . . . . .	30
b	Gravitational Aharonov-Bohm effect . . . . .	32
c	Asymmetric cross section of scattering on a vortex . . . . .	32
d	Iordanskii force: vortex and spinning string . . . . .	33
3	SPECTRAL FLOW FORCE AND CHIRAL ANOMALY . . . . .	34
a	Chiral anomaly . . . . .	34
b	Anomalous force acting on a continuous vortex and baryogenesis from textures . . . . .	35
c	Anomalous force acting on a singular vortex and baryogenesis with strings . . . . .	36
4	ANALOG OF MAGNETOGENESIS: VORTEX TEXTURES GENERATED BY NORMAL-SUPERFLUID COUNTERFLOW . . . . .	38
5	VORTEX MASS: CHIRAL FERMIONS IN STRONG MAGNETIC FIELD . . . . .	40
a	"Relativistic" mass of the vortex . . . . .	40
b	Bound states contribution to the mass of singular vortex. . . . .	40
c	Kopnin mass of continuous vortex: connection to chiral fermions in magnetic field. . . . .	41
d	Associated hydrodynamic mass . . . . .	42
	<b>CONCLUSION</b>	<b>43</b>

## I. SUPERFLUID $^3\text{He}$ AND QUANTUM FIELD THEORY

In recent times condensed matter and elementary particle physics have been experiencing remarkable convergence in their developments as many-body aspects have become increasingly more important in particle physics: The Early Universe is the ultimate testing ground where theories on interacting particle systems can be worked out for different energy regimes, or epochs of the expansion after the Big Bang. Compact astro-physical objects provide other laboratories with a narrower range of conditions in which to test theories. Finally actual collider experiments are being set up to study interacting particle systems, such as the quark-gluon plasma in heavy ion collisions or the pion condensate.

Collective phenomena in interacting many-body systems is of course what condensed matter physics is all about, but elementary particle systems are adding to the picture extreme quantum behavior plus relativistic motion. So far such systems are not available in the laboratory, where both of these features would be of importance. During the last few years it has turned out that valuable analogues can nevertheless be constructed from comparisons with nonrelativistic quantum systems of the condensed matter. The best examples of stable coherent quantum systems are the superfluids and superconductors. Of these, by far, the system with the best possibilities are the various phases of liquid  $^3\text{He}$ .

The  $^3\text{He}$  liquid phases provide attractive advantages as a model system for the study of various general concepts in quantum field theory: Here we have the most complex symmetry breaking, which gives rise to a multi-dimensional order parameter space – well described by a detailed microscopic theory. Experimentally they are generally devoid of extrinsic imperfections: The superfluid phases, for instance, are the purest of all condensed matter systems with respect to any kind of impurities or external defects. The superfluid coherence length is large such that surface roughness can be reduced sufficiently to transform the container walls to ideally behaving boundaries. Many phase transitions of both first and second order exist, which allow the investigation of defect formation. There are topologically stable defects of different dimensionality and type, which often can be detected with NMR methods with single-defect sensitivity.

However the most important advantage of  $^3\text{He}$  is that it closely resembles the complicated physical vacuum of quantum field theory — the modern ether. The bosonic and fermionic excitations in  $^3\text{He}$  are in many respects similar to the excitations of the physical vacuum — the elementary particles. In particular this allows us to model in  $^3\text{He}$  the interactions of elementary particles with the evolving strings and domain walls formed in a rapid phase transition, which may have important cosmological consequences.

This review attempts to illustrate to what extent gen-

eral physical principles of quantum field theory can be verified from analogues, constructed on the basis of measurements and calculations on  $^3\text{He}$  superfluids. The review has been split in two parts: The first part deals with a detailed description of defect formation in a rapidly quenched second-order phase transition. The second part gives a unified, but less detailed account of several other examples where analogues to  $^3\text{He}$  superfluids seem to provide useful answers.

## II. QUENCH-COOLED SUPERFLUID TRANSITION: A MODEL OF DEFECT FORMATION IN RAPID PHASE TRANSITIONS

### 1. RAPID PHASE TRANSITIONS

A rapid phase transition is generally associated with a large degree of inhomogeneity. After all, this is the process by which materials like steel or amorphous solids are prepared. This disorder we attribute to heterogeneous extrinsic influence which is usually present in any system which we study: impurities, grain boundaries, and other defects depending on the particular system. To avoid disorder and domain formation, we generally must examine phase transitions in the adiabatic limit, as close to equilibrium as possible. But suppose we had an ideally homogeneous infinite system with no boundaries. It is rapidly cooling from a symmetric high temperature state to a low temperature phase of lower symmetry, which we call the broken-symmetry phase, for example through expansion. What would happen in such a transition? Are defects also formed in this case?

Such a measurement, as a function of the transition speed, is difficult and has not been carried out in the laboratory so far. Nevertheless, if we believe in the standard theory of cosmology then one experiment exists and we know the answer. In the “Big Bang” the Universe started off in a homogeneous state. Then it rapidly cooled through a sequence of phase transitions, in which the four fundamental forces of nature separated out. We know today that the Universe must have settled down in an inhomogeneous state with large scale structure.

### 2. COSMIC LARGE-SCALE STRUCTURE

The clumped distribution of the visible mass in the Universe has become evident from galaxy surveys – maps which show that galaxies form clusters and these in turn superclusters, such as the “Great Wall”, which are the largest structures discovered to date [1]. The clustering takes the form of long and narrow chains or filaments, which are separated by large voids, regions empty of visible mass. It is not yet known how these filaments are organized – whether they form a random network or are

ordered in a more regular pattern. The most recent extended galaxy surveys indicate that there exists a repeating length scale, the separation between filaments, which is on the scale of 100 Mpc or more [2,3].

Another image of large-scale structure has been preserved in the cosmic microwave background radiation, from the time when the Universe had cooled to a few eV, when the nuclei and electrons combined to form atoms and the Universe became transparent to photons. Since then the background radiation has cooled in the expanding Universe and matches to within 3 parts in  $10^5$  the spectrum of a black body at 2.728 K, as measured with the Far InfraRed Absolute Spectrometer (FIRAS) on board of the satellite Cosmic Background Explorer (COBE) in 1990. A second instrument on COBE, the Differential Microwave Radiometer (DMR), revealed in 1992 that the background radiation shows a spatial variation, an anisotropy of  $30 \mu\text{K}$  in amplitude, when probed with an angular resolution of  $7^\circ$ . The anisotropy corresponds to density fluctuations in the structure of the Universe when it was only 300 000 years old and, although small, it is thought to be sufficient to explain the large-scale structure visible today. Cosmic background radiation is one of the few solid foundations of the standard theory of cosmology. It is not surprising that satellite missions are planned for early next century to survey the anisotropy with an angular resolution better than  $1^\circ$ .

### 3. KIBBLE-ZUREK MECHANISM

Large-scale structure and the anisotropy of cosmic background radiation are thought to be evidence for the inhomogeneity created in the phase transitions of the early Universe. In 1976 Tom Kibble proposed that a homogenous second order phase transition will form defects, if it proceeds faster than the order parameter of the broken-symmetry phase is able to relax [4]. In such a transition the new low-temperature phase starts to form, due to quantum mechanical fluctuations in the order parameter, simultaneously and independently in many parts of the system. Subsequently during further cooling, these regions grow together to form the new broken-symmetry phase. At the boundaries, where different causally disconnected regions meet, the order parameter does not necessarily match and a domain structure is formed. If the broken symmetry is the U(1) gauge symmetry, then domains with a random phase of the order parameter are formed. Such a domain structure reduces to a network of linear defects, which are vortex lines in superfluids and superconductors or perhaps cosmic strings in the early Universe. If the symmetry break is more complicated, as in the  $^3\text{He}$  superfluids, then defects of different dimensionality and structure are formed.

Indeed, numerical simulations of a rapid quench through a phase transition indicated that defects seemed to form. In 1985 Wojciech Zurek proposed a conceptually

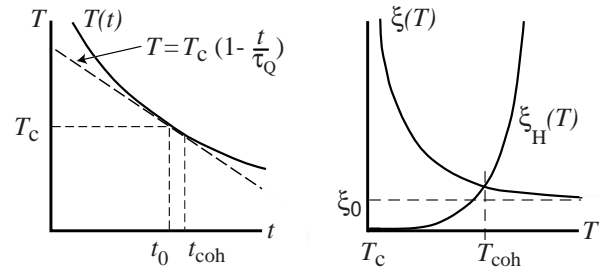


FIG. 1. Rapid cool down through  $T_c$  at constant pressure: (Left) Temperature  $T(t)$  and its linear approximation  $T = T_c(1 - t/\tau_Q)$  during the quench, as a function of time  $t$ . (Right) Superfluid coherence length  $\xi(T)$  and order parameter relaxation time  $\tau(T)$  diverge at  $T_c$ . At the freeze-out point  $t_{\text{Zurek}}$ , when phase equilibrium is achieved, the edge of the correlated region, the causal horizon, has moved out to a distance  $\xi_H(t_{\text{Zurek}})$ , which has to equal the coherence length  $\xi(t_{\text{Zurek}})$ .

powerful phenomenological approach how to understand a phase transition far out of equilibrium, when the outcome from the transition becomes time dependent [5]. He characterizes the transition speed with a quench time

$$\tau_Q = \left( \frac{1}{T_c} \left| \frac{dT}{dt} \right|_{T=T_c} \right)^{-1}, \quad (1)$$

which allows him to approximate temperature and time with a linear dependence during the thermal quench.

The quench time  $\tau_Q$  is compared to the order parameter relaxation time  $\tau$ , which in a Ginzburg-Landau system at a second order phase transition is of the general form  $\tau(T) = \tau_0(1 - T/T_c)^{-1}$ . In superfluid  $^3\text{He}$ ,  $\tau_0$  is on the order of  $\tau_0 \sim \xi_0/v_F$ , where  $\xi_0$  is the zero temperature limiting value of the temperature ( $T$ ) and pressure ( $P$ ) dependent superfluid coherence length  $\xi(T, P)$ . Close to  $T_c$ , it is of the form  $\xi(T, P) = \xi_0(P)(1 - T/T_c)^{-1/2}$ . The second quantity,  $v_F$ , is the velocity of the thermal quasiparticle excitations which are excited above the superfluid energy gap.

As sketched in Fig. 1, this means that below  $T_c$  the order parameter coherence spreads out with the velocity  $c(T) \sim \xi/\tau = \xi_0(1 - T/T_c)^{1/2}/\tau_0$ . Freeze-out of defects corresponds to the point when the causally disconnected regions grow together and superfluid coherence becomes established in the whole volume. At the freeze-out temperature  $T_{\text{coh}} = T(t_{\text{Zurek}}) < T_c$ , the causal horizon has travelled the distance  $\xi_H(t_{\text{Zurek}}) = \int_0^{t_{\text{Zurek}}} c(T) dt = \xi_0\tau_Q(1 - T_{\text{coh}}/T_c)^{3/2}/\tau_0$  which should be equal to the coherence length  $\xi(T_{\text{Zurek}})$ . This condition establishes the freeze-out temperature  $tT_{\text{coh}}/T_c = 1 - \sqrt{\tau_0/\tau_Q}$  at the freeze-out time  $t_{\text{Zurek}} = \sqrt{\tau_0\tau_Q}$ , when the domain size has reached the value

$$\xi_v = \xi_H(t_{\text{Zurek}}) = \xi_0(\tau_Q/\tau_0)^{1/4}. \quad (2)$$

In superfluid  $^3\text{He}$ ,  $\xi_0 \sim 20 \text{ nm}$ ,  $\tau_0 \sim 1 \text{ ns}$ , and in the best cases a cool-down time of  $\tau_Q \sim 1 \mu\text{s}$  can be reached.

From these values we expect the domain structure to display a characteristic length scale of order  $\xi_v \sim 0.1 \mu\text{m}$ . In a  $U(1)$ -symmetry-breaking transition, vortex lines are formed at the domain boundaries, which leads to a whole network of vortices, where the average inter-vortex distance and radius of curvature are on the order of the domain size  $\xi_v$ .

The Kibble-Zurek (KZ) mechanism has been studied in numerous numerical simulations [6], to examine whether vortex freeze out can be demonstrated. The model has also been compared to experiments on liquid crystals [7] and on superfluid  $^4\text{He}$  [8–10], but so far the only quantitative comparisons with measurements have been achieved in the case of superfluid  $^3\text{He}$  [11,12]. Three features have been most valuable in the last category of experiments: The absence of defects and extrinsic influence, the high speed of the phase transition front [13], and the resolution in detecting single vortex lines.

The KZ model describes a second order transition where the energy barrier separating the high-temperature symmetric and the low-temperature broken-symmetry states vanishes at  $T_c$  and the transition becomes an instability. A first order transition is different: Here the barrier remains finite and the low temperature phase has to be nucleated. Nucleation may occur in different regions nearly simultaneously, depending on the system, the quench time  $\tau_Q$ , and the nucleation mechanism. This then also leads to domain formation and to a final state which is qualitatively similar to that after the second order transition and the KZ mechanism. The liquid crystal experiments have been performed in this situation [7].

#### 4. PRINCIPLE OF EXPERIMENTS IN $^3\text{He-B}$

In order to study defect formation in a rapid phase transition, two basic requirements should be met: First, one should be able to produce the transitions in a reproducible way. Second, one should have the means to stabilize defects after their formation and to detect them. Both these requirements can be conveniently satisfied in the experiments on  $^3\text{He-B}$ .

##### a. Experimental outline

A schematic illustration of one set of experiments [11] is depicted in Fig. 2. The top part displays the events which are observed by the experimentalist in the laboratory. Here a long cylindrical container filled with superfluid  $^3\text{He-B}$  is rotated at constant velocity  $\Omega$ . The velocity of rotation is maintained below the critical value at which vortex lines are spontaneously nucleated. In other words, the initial state is one of metastable vortex-free counterflow under constant conditions.

Next a weak source of slow thermal neutrons is placed in the vicinity of the  $^3\text{He}$  sample. If the rotation velocity

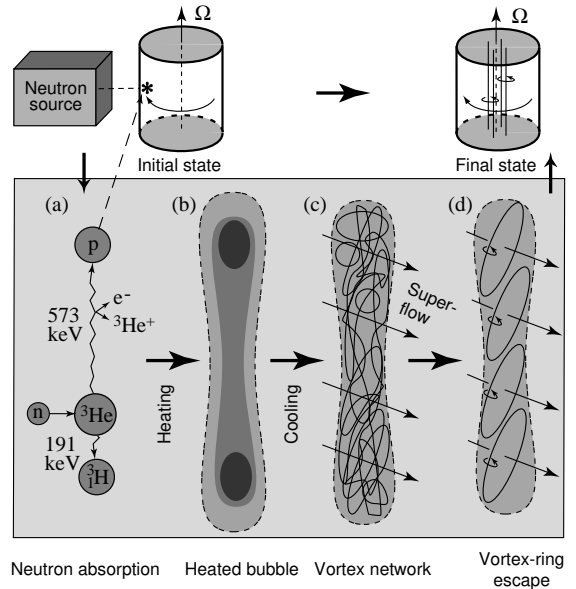


FIG. 2. Principle of the experiment with a rapid thermal quench from the normal phase to the superfluid: (Top) A cylindrical sample container with superfluid  $^3\text{He-B}$  is rotated at constant angular velocity  $\Omega$  and bulk liquid temperature  $T$ , while the NMR absorption is monitored continuously. When the sample is irradiated with neutrons, vortex lines are observed to form. (Bottom) Interpretation of the processes in the superfluid, see the text for details. (From Ref. [11].)

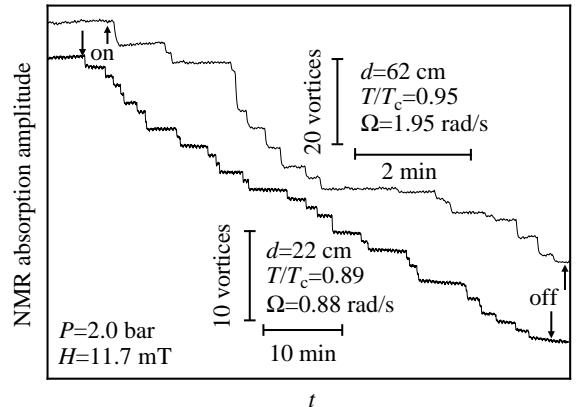


FIG. 3. Height of the counterflow peak in the NMR absorption spectrum as a function of time  $t$  during neutron irradiation at low (lower trace) and high  $\Omega$  (upper trace). The vertical arrows indicate when the neutron source was turned on/off. Each step corresponds to one neutron absorption event and its height, when compared to the adjacent vertical calibration bar, gives the number of vortex lines formed per event. The distance of the neutron source from the sample is denoted with  $d$ . (From Ref. [24].)

is sufficiently high then vortices start to appear at a rate which is proportional to the neutron flux. The neutron source is positioned at a convenient distance from the

cryostat so that vortex lines are observed to form in well-resolved individual events. The experimental signal for the appearance of a new vortex line is an abrupt jump in NMR absorption. An example, measured at low rotation, is shown by the lower recorder trace in Fig. 3.

The lower part of Fig. 2 shows in more detail what is thought to happen within the superfluid. Liquid  $^3\text{He}$  can be conveniently locally heated with the absorption reaction of a thermal neutron:  $n + ^3_2\text{He} \rightarrow p + ^3_1\text{H} + E_0$ , where  $E_0 = 764$  keV. The reaction products, a proton and a triton, are stopped by the liquid and produce two collinear ionization tracks [14]. The ionized particles, electrons and  $^3\text{He}$  ions, diffuse in the liquid to recombine such that 80 % or more of  $E_0$  is spent to heat a small volume with a radius  $R_b \sim 50 \mu\text{m}$  from the superfluid into the normal phase. The rest of the reaction energy escapes in the form of ultraviolet emission [15] and, possibly, in the form of long-living molecular  $^3\text{He}_2^*$  excitations, which mostly relax at the walls of the container.

For rotating  $^3\text{He}$  measurements neutron absorption is an ideal heating process: The large absorption cross section for slow neutrons corresponds to a mean free path of about  $100 \mu\text{m}$  and thus most neutrons are absorbed within a close distance from the wall. This means that the reactions occur within bulk liquid, but close to the cylindrical wall, where the velocity of the applied counterflow is accurately known. In other parts of the refrigerator neutron absorption is negligible and thus the temperature of the  $^3\text{He}$  sample can be maintained stable during the irradiation. Subsequently, the heated volume of normal liquid cools back through  $T_c$  in microseconds.

The measurements demonstrate that indeed vortices can be formed in the neutron absorption events. Vortex loops, which are formed in the heated neutron bubbles within the bulk superfluid, would normally contract and disappear in the absence of rotation. Here the driving force is provided by the intervortex interactions between the vortex filaments while the dissipation is brought about by the mutual friction between the normal and superfluid components. In the zero temperature limit mutual friction becomes vanishingly small and the life time of the vorticity sufficiently long such that its existence can be resolved as a deficit in the energy balance of the neutron absorption reaction [12]. In rotating experiments the externally applied counterflow provides a bias which causes sufficiently large loops to expand to rectilinear vortex lines and maintains them for detection [11].

Several different suggestions can be offered to explain these observations. The KZ model is one of them. However, whatever the mechanism, the phenomenon is associated with what appears to be the fastest 2nd order phase transition which has been probed to date. The superfluid transition in a localized bubble, heated by the absorption of ionizing radiation, represents a new process for creating quantized vortex rings inside the bulk superfluid and is not restricted to the container wall, as is usually the case in the presence of applied counterflow.

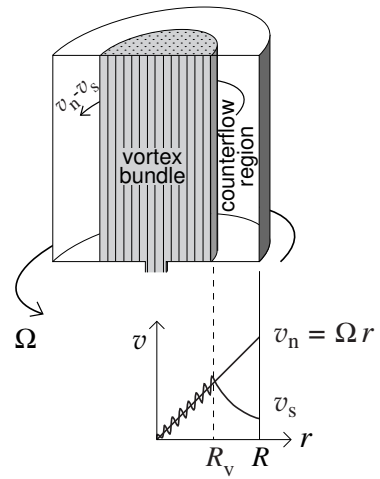


FIG. 4. (Top) Schematic view of rectilinear quantized vortex lines in a rotating cylinder in a metastable counterflow state. (Bottom) Radial distribution of the velocities of the normal component,  $v_n$ , which corotates with the container, and the superfluid component,  $v_s$ . (From Ref. [18].)

The interpretation of the later stages of the experiment is contained in the two illustrations marked as (c) and (d) in Fig. 2. It is based on studies of the number of vortex lines, which are formed per neutron absorption event, as a function of the various external variables and, foremost, as a function of the velocity of the applied counterflow. First a random vortex network (c) is created while cooling through  $T_c$ . Next the network starts to evolve under the influence of intervortex interactions and the applied counterflow. The evolution is dissipative due to the mutual friction force which connects the superfluid and normal components of the liquid and acts on a moving vortex. The average intervortex distance increases, small loops are smoothened out, and the network becomes rarefied or “coarse grained”. Also reconnection, which takes place when two lines cross each other, contributes to the increase. The applied counterflow favors the growth of loops with the right winding direction and orientation. It causes sufficiently large loops to expand, while others contract and disappear. A somewhat similar situation has been studied in the stationary state turbulent flow of superfluid  $^4\text{He}$  through a pipe [16,17]. The final outcome is that correctly oriented loops (d), which exceed a critical threshold size, will start expanding spontaneously as vortex rings, until they meet the chamber walls. There the superfluous sections of the ring will annihilate and only a rectilinear vortex line will finally be left over. It is pulled to the center of the container, where it remains in stationary state parallel to the rotation axis, stretched between the top and bottom surfaces.

The distinctive feature of this explanation is the fact that very different time scales are at work in this process of vortex formation. The initial vortex network forms during the quench through  $T_c$ , for which the relevant

time scale is microseconds. In contrast, the later evolution of the vortex network and the loop escape happen on a much slower time scale, the mutual-friction-dependent superfluid hydrodynamics with processes which take milliseconds or even seconds to complete. It appears that the KZ mechanism may be the fastest process available for vortex creation, such that it bypasses all other possible mechanisms which might become effective later on the much slower hydrodynamic time scale.

*b. Vortex lines in rotating  $^3\text{He-B}$*

There are two major phases of superfluid  $^3\text{He}$ , the A and B phases (see Fig. 12). The neutron measurements have been performed in the quasi-isotropic  $^3\text{He-B}$ . In the present context we may think of vortices in  $^3\text{He-B}$  as being similar to those in superfluid  $^4\text{He-II}$ , where only the U(1) symmetry is broken and the order parameter is of the general form  $\Psi = |\Psi(T)| e^{i\Phi(\mathbf{r})}$ : These vortices are topologically stable, have a singular core, inside of which  $|\Psi|$  deviates from its bulk value, while outside the phase  $\Phi$  changes by  $2\pi\nu$  on a closed path. A persistent superfluid current is trapped as a single-quantum circulation  $\nu = 1$  around the core, with the circulation quantum  $\kappa = h/(2m_3) \simeq 0.067 \text{ mm}^2/\text{s}$  and a superflow velocity  $\mathbf{v}_{\text{s,vort}} = \kappa/(2\pi) \nabla\Phi = \kappa/(2\pi r) \hat{\phi}$ .

The energy of a single vortex placed in the center of the cylindrical container of radius  $R$  and height  $Z$  is the hydrodynamic kinetic energy of the superfluid trapped by the vortex:

$$E_v = \frac{1}{2} \int \rho_s v_{\text{s,vort}}^2 dV = \frac{\rho_s \kappa^2}{4\pi} Z \ln \frac{R}{\xi} . \quad (3)$$

Here the ultraviolet divergence is cut-off by the core radius of the vortex which is of order the coherence length  $\xi$ . In the container rotates with the angular velocity  $\Omega$  the state with one single vortex line becomes energetically favorable when the quantity  $E_v - \Omega L_z$  becomes negative, where  $L_z$  is the hydrodynamic angular momentum of the superflow around the vortex:

$$L_z = \int \rho_s r v_{\text{s,vort}} dV = \rho_s \kappa R^2 Z . \quad (4)$$

This happens when the velocity  $\Omega R$  of the wall exceeds the Feynman critical velocity  $v_{c1} = \kappa/(2\pi R) \ln(R/\xi)$ . With a container radius  $R$  of a few mm and a circulation quantum  $\kappa = h/(2m_3) = 0.066 \text{ mm}^2/\text{s}$  this velocity is only  $10^{-2} \text{ mm/s}$ . However if we exclude extrinsic mechanisms of vortex formation, then the vortex-free state will persist metastably to much higher velocities because of a nucleation energy barrier. In  $^4\text{He-II}$  the barrier is ultimately surmounted by thermal activation, while at low temperature the quantum tunneling can become more important.

In  $^3\text{He-B}$  the barrier is unpenetrable at practically all temperatures. The vortex is nucleated on the cylindrical wall as a segment of a vortex ring. The energy of the smallest possible vortex ring, which has the radius of order coherence length, is of order  $E_v \sim \rho_s \kappa^2 \xi$ . This energy constitutes the nucleation barrier. On dimensional grounds we may write  $E_v/T \sim (\xi/a)(T_F/T)$ , where  $T_F = \hbar^2/2m_3 a^2 \sim 1 \text{ K}$  is the degeneracy temperature of the quantum fluid and  $a$  the interatomic distance. For superfluid  $^4\text{He-II}$ , where the coherence length  $\xi \sim a$ , while  $T$  can be of order  $T_F$ , we find that  $E_v/T$  can be of order 1 and thus the vortex loops can be thermally activated. In contrast in  $^3\text{He-B}$  the coherence length  $\xi$  is 10 to 100 nm and we get that  $E_v/T$  is typically of order  $10^5$  at the appropriate millikelvin temperatures. This huge barrier means that in  $^3\text{He-B}$  both thermal activation and quantum tunneling are out of the question. The only way to create the vortices is the development of the hydrodynamic instability, which happens at rather high velocity of rotation when the superfluidity collapses near the walls of container [19].

Since in  $^3\text{He-B}$  the energy barrier for creating a new vortex is exceedingly high, the metastable rotating states, where the number of vortex lines is less than the equilibrium value, can be formed and maintained. In this case the existing rectilinear vortex lines are organized in the rotating container as shown in Fig. 4 [18]. If the number of lines  $N$  is smaller than in the equilibrium state, they are confined by the Magnus force from the superfluid counterflow to a central cluster or bundle, around which the vortex-free counterflow circulates. Within the bundle their mutual repulsion keeps the vortex lines apart such that they form an array with the equilibrium value of the density,  $n_v = 2\Omega/\kappa$ . At this line density the bundle corotates with the container at constant  $\Omega$ , like a solid body. The total number of lines is given by  $N = \pi n_v R_v^2$ , where  $R_v^2$  is the radius of the bundle.

If there are no vortex lines in the container, the superfluid component remains at rest in the laboratory frame and its velocity  $v_s = 0$  in the whole container while the normal excitations corotate with the container,  $v_n = \Omega r$ . With  $N$  vortex lines in the central bundle,  $v_s = \kappa N/(2\pi r)$  outside the bundle. This is equivalent to the superflow velocity around a giant vortex with  $N$  circulation quanta  $\kappa$ . The Magnus force acting on a vortex line is driven by the counterflow velocity,  $v = v_n - v_s$ , which vanishes inside the bundle (measured on length scales which exceed the inter-vortex distance), while outside it increases from zero at  $r = R_v$  to its maximum value at the cylinder wall,  $r = R$ :

$$v(R) = \Omega R - \frac{\kappa N}{2\pi R} . \quad (5)$$

In the absence of the neutron source new vortex lines are only formed if  $v(R)$  is increased to its container-dependent critical value  $v_c(T, P)$  [19]. For a quartz glass cylinder  $v_c$  is a factor of three or more larger than the lowest velocity  $v_{\text{cn}}(T, P)$  at which vortices start to appear

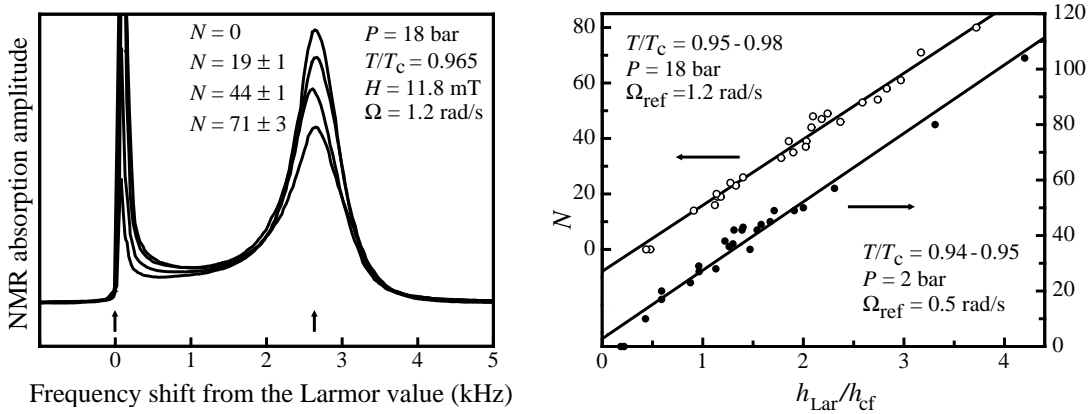


FIG. 5. NMR measurement of vortex lines in superfluid  $^3\text{He-B}$ , when rotated in a long cylinder with the magnetic field oriented axially: (Left) NMR spectra recorded at a reference velocity  $\Omega_{\text{ref}} = 1.2$  rad/s with different number of vortex lines  $N$ . The Larmor frequency is at the left and the counterflow peak at the right vertical arrow. (Right) Two calibration measurements of the number of vortex lines  $N$  as a function of the ratio of the Larmor and counterflow peak heights,  $h_{\text{Lar}}/h_{\text{cf}}$ , measured at the rotation velocity  $\Omega_{\text{ref}}$ . (From Ref. [21].)

in neutron irradiation (see Fig. 11).

### c. NMR measurement of $^3\text{He-B}$

The NMR properties of the  $^3\text{He}$  superfluids are exceptional due to a spin-orbit coupling, which is weak but, nevertheless, responsible for the many peculiar features of the NMR spectra. It is generated by the dipole-dipole interaction in Cooper pairs and typically gives rise to additional absorption peaks with large shifts from the Larmor frequency [20].

In the left panel of Fig. 5 cw NMR absorption spectra are shown for  $^3\text{He-B}$ , measured at the same  $\Omega$ , but with a different number  $N$  of vortex lines in the container. The asymmetric peak on the left close to the Larmor frequency originates from that part of the container where the average counterflow is zero or small, which is the centre with or without the vortex bundle. Outside the bundle the macroscopic normal-superfluid counterflow shifts the NMR absorption to higher frequencies into a “counterflow peak”, which is shown on the right. The frequency shift of the counterflow peak increases monotonically with decreasing temperature and may be used as a measure of the temperature. When the number of vortices in the container is changed, the size of the bundle changes, and the relative amount of absorption in the Larmor and counterflow peaks changes accordingly. This is because the total integrated absorption in the NMR spectrum is proportional to the B phase susceptibility  $\chi_B(T, P)$ , which is constant if only  $N$  undergoes a change. Thus by monitoring the peak height of either one of the absorption maxima, one can detect a change in  $N$ , as was shown in Fig. 3.

In the right panel of Fig. 5 the ratio of the two peak heights has been calibrated to give the vortex number

at two different constant angular velocities  $\Omega_{\text{ref}}$ , when only a relatively small number of vortex lines exist ( $N \ll \pi n_v R^2$ ), such that a large absorption maximum is produced by the vortex-free counterflow [21]. This calibration plot was measured starting from an initially vortex-free state rotating at  $\Omega_{\text{ref}}$  into which a given number of vortex lines  $N$  are with neutron absorption reactions, as in Fig. 3. After that the whole NMR spectrum was recorded (by sweeping the magnetic polarization field  $H$ ). By measuring the ratio of the heights of the two absorption peaks from the spectrum and by plotting it versus  $N$ , the linear relationship in Fig. 5 was obtained.

In favorable conditions, which appear to be low magnetic fields ( $H \sim 10$  mT) close to  $T_c$  ( $T \geq 0.8 T_c$ ), the single-vortex signal can be discerned with good resolution, like in the case of Fig. 3. As shown in Fig. 6, the reduction in the height of the counterflow peak is only visible at higher counterflow velocities ( $\Omega > 0.6$  rad/s) [22], where the counterflow peak is well developed. In this regime the absolute magnitude of the single-vortex signal decreases with increasing rotation and height of the counterflow peak. In the measurements to be explained below, the vortex number is determined directly from records like the two traces in Fig. 3. The plot in Fig. 6 provides a gauge of the single-vortex step size, to estimate the number of new lines when multiple lines are created in one neutron absorption event.

## 5. VORTEX FORMATION IN NEUTRON IRRADIATION

A measurement of vortex-line formation in neutron irradiated normal-superfluid counterflow is performed at constant ambient conditions. The externally controlled variables include the rotation velocity  $\Omega$ , temperature  $T$ ,



pressure  $P$ , magnetic field  $H$ , and neutron flux  $\phi_n$ . The initial state is one of vortex-free counterflow:  $N = 0$ . When stable conditions have been reached, a weak neutron source is placed at a distance  $d$  from the  $^3\text{He}$ -B sample and the output from the NMR spectrometer is monitored as shown in Fig. 3. From NMR absorption record as a function of time the vortex lines can be counted

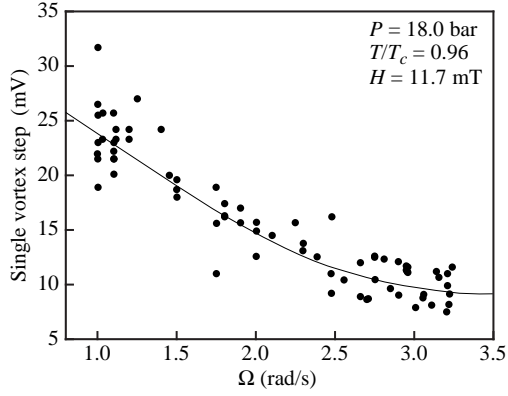


FIG. 6. Absolute magnitude of the single-vortex steps (as in Fig. 3), measured in the vortex-free counterflow state at different  $\Omega$ . The reduction in the height of the counterflow peak is given here in millivolts at the output of the cooled preamplifier inside the vacuum jacket of the cryostat, which has a gain of  $\approx 10$ . The scatter in the data illustrates the signal-to-noise ratio. This plot is used as a calibration to figure out the number of vortex lines responsible for large steps when many vortex lines appear simultaneously. More details on the NMR spectrometer can be found in Ref. [19].

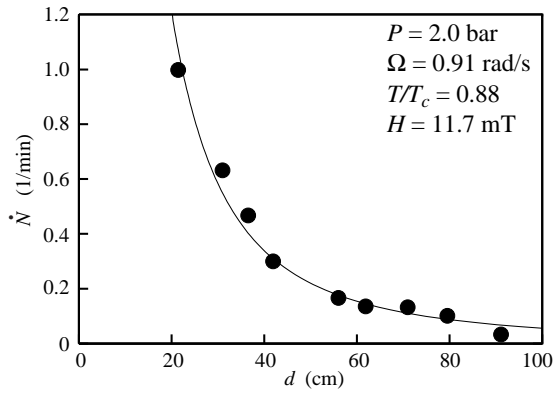


FIG. 7. Rate of vortex-line formation in neutron irradiated counterflow,  $\dot{N}$ , as a function of the distance  $d$  between neutron source and  $^3\text{He}$ -B sample. The initial state is vortex-free counterflow at a rotation velocity of 0.91 rad/s. The neutron irradiation time is 30 min. The fitted curve is of the form  $\ln[1 + (R_s/d)^2]$ , where  $R_s$  is the radius of the circular front surface of the paraffin moderator box (perpendicular to  $\mathbf{d}$ ), in which the Am-Be source is embedded.

which are formed during a given irradiation period.

The process evidently exhibits statistical behaviour. Therefore to measure the vortex-formation rate  $dN/dt = \dot{N}$ , records with a sufficiently large number of detected neutron absorption events should be averaged, to smoothen out statistical variation and to obtain a reasonably accurate result. After that one of the experimental parameters is changed and a new run is performed. In this way the dependence of the vortex formation process on the external variables can be identified and studied. It was found that the rate varies as a function of all the external parameters, i.e. neutron flux, rotation velocity, temperature, pressure and magnetic field. In the following we shall first describe these empirically established dependences.

The rate of vortex-line formation is proportional to the neutron flux. The latter is varied by changing the distance of the source from the cryostat. In this way individual absorption events can be studied, which are well separated in time. A calibration plot of the measured rate of vortex-line formation  $\dot{N}$ , as a function of the distance between sample and source, is shown in Fig. 7. By means of this plot the results can be scaled to correspond to the same incident neutron flux, for example to the minimum distance  $d = 22$  cm, which is given by the outer radius of the liquid He dewar.

The most informative feature has been the dependence of the rate  $\dot{N}$  on rotation [11,23,24]. Rotation produces the applied counterflow velocity  $v$ : It is controlled by both the rotation velocity  $\Omega$  and the number of vortex lines  $N(t)$  which are already present in the container. Clearly the counterflow provides the force which allows vortex rings to escape from the heated neutron bubble and to expand to rectilinear vortex lines, which are then preserved in stable state in the central vortex bundle. But in addition we face the question whether it is the velocity  $v(R)$  of the counterflow, given by Eq. (5), or that of the normal component,  $v_n(R) = \Omega R$ , which is the important variable controlling the rate  $\dot{N}$ .

This question is illustrated by Fig. 8 where the number of vortex lines  $N(t)$  is shown during neutron irradiation at constant external conditions over a time span of six hours. The irradiation is started from the vortex-free state:  $N(t = 0) = 0$ . The rate  $\dot{N}(t)$ , at which vortex lines accumulate in the centre of the container, is not constant: Initially both the counterflow velocity and the rate of vortex formation are the highest. When more vortex lines collect in the central bundle, both the velocity  $v$  and the rate  $\dot{N}$  fall off. Finally the vortex number  $N$  approaches a saturation value, beyond which no more lines are formed. This means that there exists a lower limit, a threshold value for the counterflow velocity, below which the neutron absorption events produce no vortex lines at all.

In principle all dependence of  $\dot{N}$  on the counterflow velocity can be extracted from experiments like that shown in Fig. 8. However, more efficient is to measure only the

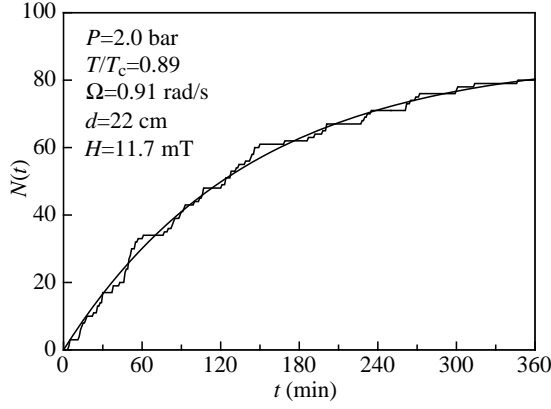


FIG. 8. Cumulative number of vortex lines  $N(t)$  as a function of time  $t$ , after turning on the neutron irradiation at constant flux on an initially vortex-free  $^3\text{He-B}$  sample rotating at constant  $\Omega$ . The continuous curve represents a fit with  $\alpha = 1.1 \text{ min}^{-1}$  and  $v_{\text{cn}} = 1.9 \text{ mm/s}$ . (From Ref. [24].)

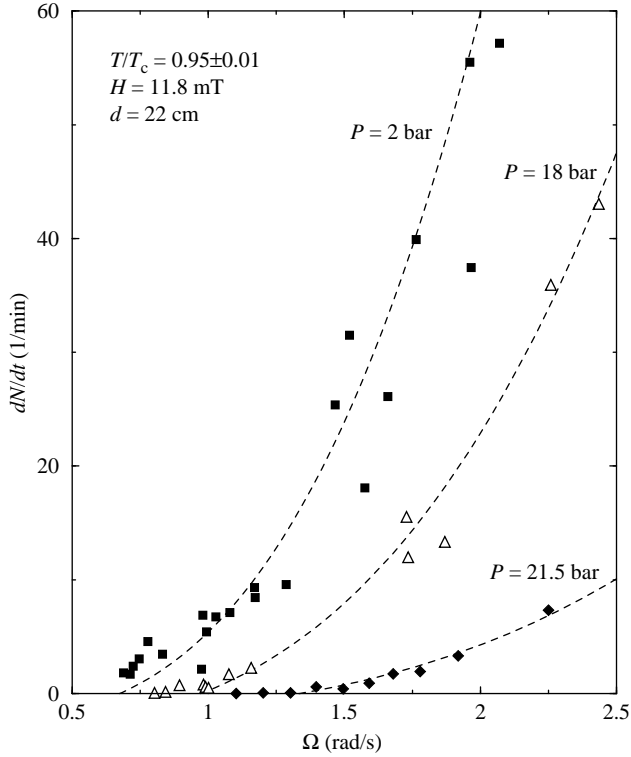


FIG. 9. Rate  $\dot{N}$  of vortex line formation at different rotation velocities  $\Omega$ .  $\dot{N}$  has been measured as the average of all vortex lines formed during an accumulation period of 15–30 min. The fitted curves are of the form  $\text{const} \cdot ((\Omega/\Omega_{\text{cn}})^3 - 1)$ . Their low velocity end points determine the threshold velocity  $v_{\text{cn}} = \Omega_{\text{cn}} R$ . (From Ref. [23].)

initial linear part of  $\dot{N}(t)$  at different  $\Omega$ . Typically 15–30 min accumulation periods are used. Only a small number of vortices are formed during such a run, compared to the corresponding equilibrium number of vortices. Thus the

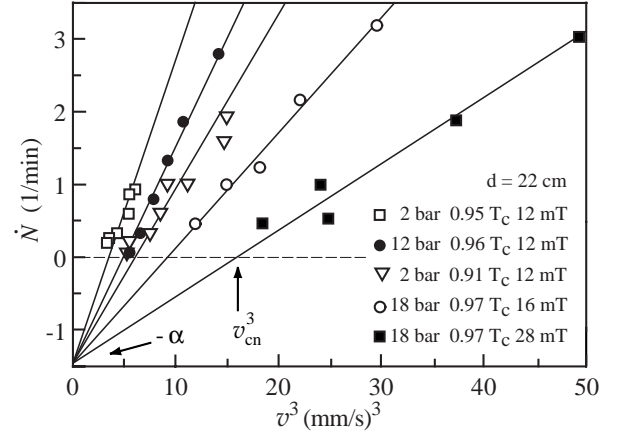


FIG. 10. Vortex-formation rate  $\dot{N}$  plotted versus the cube of the counterflow velocity  $v$ . This plot is used to determine the threshold velocity  $v_{\text{cn}}$ . A line has been fit to each set of data, measured under different external conditions, to identify the horizontal intercept  $v_{\text{cn}}^3$  and the common vertical intercept  $-\alpha = -1.4 \text{ min}^{-1}$ . (From Ref. [11].)

decrease in the counterflow velocity as a function of time is minor and can be accounted for by assigning the average of the velocities before and after irradiation as the appropriate value of counterflow velocity. An example of such raw data is shown in Fig. 9. Here each data point represents accumulation of vortex formation events for a short period at a constant value of  $\Omega$ .

Such measurements reveal a vortex-formation rate  $\dot{N}(v)$  as a function of the counterflow velocity  $v$  which has an onset at a threshold velocity  $v_{\text{cn}}$ , followed by a rapid non-linear increase. Initially the increase arises partly because the fraction of absorption events which produce a new vortex line increases. Eventually this effect is limited by the neutron flux, when all neutrons produce at least one new vortex. The second part of the increase in the vortex-formation rate with counterflow velocity is brought about by the fact that more and more vortex lines are produced, on an average, in each absorption event.

In Fig. 10 the vortex-formation rate is shown as a function of the counterflow velocity. The dependence is approximated by the empirical expression

$$\dot{N}(v) = \alpha \left[ \left( \frac{v}{v_{\text{cn}}} \right)^3 - 1 \right], \quad (6)$$

This expression also describes the results in Fig. 8: If the counterflow velocity at the container wall in the initial vortex-free state  $v(t=0)$  is only slightly larger than the critical velocity  $v_{\text{cn}}$  then Eq. (6) can be written in the linearized form  $\dot{N} \simeq 3\alpha(v/v_{\text{cn}} - 1)$ . Thus  $N(t)$  is given by the equation

$$\dot{N}(t) = 3\alpha \left( \frac{v(0) - \kappa N(t)/(2\pi R)}{v_{\text{cn}}} - 1 \right) \quad (7)$$

with the solution

$$N(t) = \frac{2\pi R}{\kappa} [v(0) - v_{\text{cn}}] \left[ 1 - \exp\left(-\frac{3\alpha\kappa t}{2\pi R v_{\text{cn}}}\right) \right]. \quad (8)$$

This equation has been fitted to the measurements to give the two parameters  $\alpha$  and  $v_{\text{cn}}$  (see Fig. 8). The resulting values agree with those of the horizontal and vertical zero intercepts in Fig. 10.

In fact, it could be guessed from Fig. 10 that Eq. (6) has wider applicability than is apparent from the present examples: The same equation holds universally under different externally applied conditions with all dependence on external variables contained in  $v_{\text{cn}}(T, P, H)$ , while  $\alpha$  is proportional to the neutron flux but does not depend on the temperature, pressure or magnetic field. Hence  $N(v/v_{\text{cn}})$  is a universal function for all performed measurements, which so far have been restricted to the temperature regime  $T > 0.8 T_c$ .

To summarize, the experimental result displays two distinguishing properties: 1) the cubic dependence on the bias  $v$  and 2) the universality feature that all dependence of the vortex formation properties on the experimental variables  $T$ ,  $P$ , and  $H$  is contained in the threshold velocity  $v_{\text{cn}}$ .

## 6. THRESHOLD VELOCITY FOR VORTEX LOOP ESCAPE

The dependence on the counterflow bias can be studied from the threshold  $v_{\text{cn}}$  up to the critical limit  $v_c$  at which a vortex is spontaneously nucleated at the cylindrical wall in the absence of the neutron flux [19]. The threshold velocity  $v_{\text{cn}}(T, P, H)$  is one of the features of the experiment which can be analyzed to learn about the mechanism of vortex formation. Both velocities  $v_{\text{cn}}$  and  $v_c$  are shown in Fig. 11 as a function of temperature.

### a. Properties of threshold velocity

The threshold  $v_{\text{cn}}$  by definition represents the smallest velocity at which a vortex ring can escape from the heated bubble after the neutron-absorption event. It can be connected with the bubble size in the following manner. A vortex ring of radius  $r_o$  is in equilibrium with the counterflow  $v$  if it satisfies the equation

$$r_o(v) = \frac{\kappa}{4\pi v} \ln\left(\frac{r_o}{\xi(T, P)}\right). \quad (9)$$

A larger ring will expand in the flow while a smaller will contract. Since vortex loops are situated inside the heated bubble this impose restrictions on their size. The threshold, i.e. minimum velocity corresponds to the maximum possible vortex-ring size. It must be of similar size as the diameter of the heated bubble. Exact relation

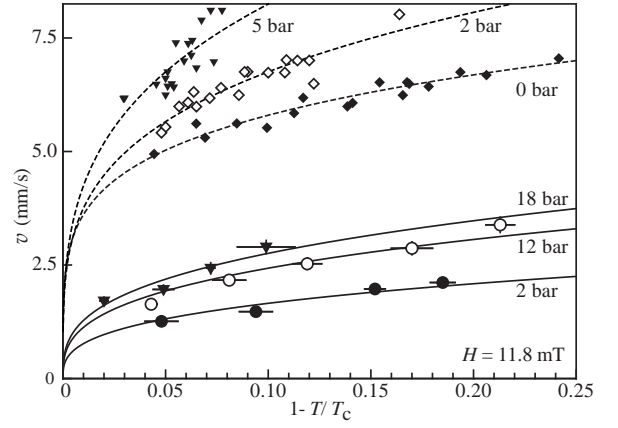


FIG. 11. Critical counterflow velocity vs. normalized bulk liquid temperature  $1 - T/T_c$  at different pressures: (Solid lines) Threshold velocity  $v_{\text{cn}} \propto (1 - T/T_c)^{1/3}$ , where vortex formation starts in the presence of the neutron source [11]. (Dashed lines) Critical velocity  $v_c \propto (1 - T/T_c)^{1/4}$ , where a vortex is spontaneously nucleated in the same quartz glass container in the absence of the neutron source. (From Ref. [19].)

between the bubble radius and the critical radius  $r_o$  is not easy to obtain because generally vortex loops are of complex shape and not simple circular loops. However, for the simplest estimation we may say that a spherical bubble would be encircled by just one single vortex ring at the threshold velocity, so that its radius gives a rough estimate for the radius  $R_b$  of the heated volume:  $R_b \sim r_o(v_{\text{cn}})$ . The numerical simulations described in Sec. II-11c suggest that  $2R_b = r_o(v_{\text{cn}})$ .

A simple thermal diffusion model can be used to yield an order of magnitude estimate for the size of a bubble which has been heated to normal phase. In the temperature range covered by our experiments it cools via diffusion of quasiparticle excitations out into the surrounding superfluid with a diffusion constant  $D \approx v_F l$ , where  $v_F$  is their Fermi velocity and  $l$  their mean free path. The difference from the surrounding bulk temperature  $T_0$  as a function of the radial distance  $r$  from the centre of the bubble can be calculated from the diffusion equation

$$\frac{\partial T(r, t)}{\partial t} = D \frac{\partial^2 T}{\partial r^2} + \frac{2}{r} \frac{\partial T}{\partial r}. \quad (10)$$

With assumption that at the initial moment heat is deposited at  $r = 0$  the solution is given by

$$T(r, t) - T_0 \approx \frac{E_0}{C_v} \frac{1}{(4\pi Dt)^{3/2}} \exp\left(\frac{-r^2}{4Dt}\right), \quad (11)$$

where  $E_0$  is the energy deposited by the neutron reaction as heat and  $C_v$  is the specific heat. The bubble of normal fluid,  $T(r) > T_c$ , first expands and reaches a maximum radius

$$R_b = \sqrt{\frac{3}{2\pi e}} \left(\frac{E_0}{C_v T_c}\right)^{1/3} (1 - T_0/T_c)^{-1/3}. \quad (12)$$

It then starts cooling and rapidly shrinks with the characteristic time  $\tau_Q \sim R_b^2/D \sim 1\mu s$ . Since  $v_{cn}$  is inversely proportional to  $r_o \sim R_b$ , it has the temperature dependence  $v_{cn} \propto (1 - T_0/T_c)^{1/3}$ . This is in agreement with the solid curves in Fig. 11 which have been fitted to measurements on  $v_{cn}$ . The prefactor of these curves is in agreement with that from Eqs. (12) and (9) within a factor of  $\sim 2$ , and its increase with increasing pressure is well described by the decrease in bubble size according to Eq. (12), where  $C_v$  and  $T_c$  increase with pressure [25].

### b. Mechanisms of vortex-ring formation

In the above analysis we have assumed that the typical size of vortex loops, which escape into the bulk at the threshold velocity  $v_{cn}$ , is approximately  $R_b$ , the radius of the heated bubble. From this it is not yet clear whether vortex formation is controlled only by the boundary condition at the circumference of the heated bubble or whether the interior of the bubble is also involved. This experiment in  $^3\text{He-B}$  is not an exact replica of the ideal KZ model – namely that of a second order transition in an infinite homogeneous system. Inside the heated bubble we have a strong thermal gradient and a strict boundary condition applies at its exterior, imposed by the bulk superfluid state outside. Moreover, the cool down occurs so fast that any extrapolation from the equilibrium state theories is in doubt, whether it concerns the hydrodynamics or even the superfluid state itself.

In addition to the KZ mechanism, one can suggest alternative sources of vortex formation. One of the most evident is the superflow instability, which occurs in the heated  $^3\text{He-B}$  liquid surrounding the hot bubble. In the Ginzburg-Landau temperature regime the container-dependent spontaneous critical velocity  $v_c(T, P)$  decreases with increasing temperature (dashed curves in Fig. 11). It is related to the intrinsic instability velocity  $v_{cb}(T, P)$  of the bulk superfluid [19], which has qualitatively a similar temperature and pressure dependence, but is larger in magnitude:  $v_{cb}(T, P) \geq v_c(T, P)$ . If no other process intervenes, the superflow instability has to occur in the peripheral region of the bubble where the local temperature corresponds to that at which the applied counterflow velocity  $v$  equals the critical value  $v_{cb}(T, P)$  of the bulk superfluid. One or several vortex rings are then formed, which encircle the bubble. Their number depends on the shape and size of the bubble. In this process it does not matter what the state of the liquid is in the interior of the bubble: The rings are formed in the external cooler region, which remains throughout the process in the B phase. The rings shield the bubble volume from the external superflow. The formation of a large vortex ring of  $100\ \mu\text{m}$  in diameter is a slow process: The characteristic time scale of superfluid hydrodynamics is in the range of milliseconds to seconds. A related alternative, superfluid turbulence forming in

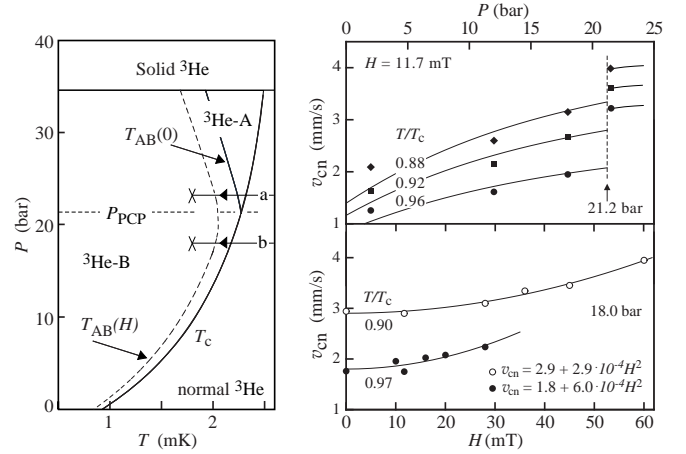


FIG. 12. Threshold velocity  $v_{cn}$  for the onset of vortex formation during neutron irradiation: (Left) Phase diagram of  $^3\text{He}$  superfluids in the pressure vs. temperature plane, with the A $\rightarrow$ B transition at  $T_{AB}(0)$  in zero field and at  $T_{AB}(H)$  in nonzero field. Two quench trajectories, distinguishing different types of measurements on the right, are marked with (a) and (b). (Right top) The pressure dependence displays a steep change at the pressure  $P_{PCP}$  of the polycritical point. (Right bottom) The magnetic field dependence is parabolic, similar to that of the equilibrium state A $\rightarrow$ B transition  $T_{AB}(H)$ . (From Ref. [23].)

the whole volume of the heated bubble, also involves the hydrodynamic time scale.

## 7. INFLUENCE OF $^3\text{He-A}$ ON THRESHOLD VELOCITY

In the above measurements there exists an interesting possibility to decide whether the interior of the heated bubble participates in vortex formation or not. In the left panel of Fig. 12 the phase diagram of  $^3\text{He}$  is shown at temperatures below 2.5 mK. In the measurements which have been discussed so far the liquid pressure has been below 21.2 bar, so that the heated bubble cools from the normal phase along a trajectory marked with (b). On the top right in Fig. 12 the results of measurements on  $v_{cn}$  are plotted as a function of liquid pressure  $P$  at constant reduced temperature  $T/T_c$ . Here the pressure dependence displays an abrupt increase at about 21.2 bar, the pressure  $P_{PCP}$  of the polycritical point: It makes a difference whether the quench trajectory follows a path denoted with (a) or with (b)! The difference in the two trajectories is that above  $P_{PCP}$  the anisotropic  $^3\text{He-A}$  phase is stable in zero field below  $T_c$  between the normal and B phases. Consequently, although the bulk liquid is well in the B phase in all of the measurements of Fig. 12, vortex formation is reduced when the quench trajectory crosses the stable A-phase regime.

The results on both the pressure and magnetic field dependences of the threshold velocity  $v_{cn}(P, H)$  in Fig. 12



are thought to demonstrate that the interior of the heated bubble participates in vortex formation and that it is not the superfluid boundary condition at the warm bubble boundary which governs  $v_{\text{cn}}$ . The steep pressure dependence of  $v_{\text{cn}}$  at  $P_{\text{PCP}}$  differs from the typical behavior of the bulk B-phase properties, which are changing smoothly with pressure. For instance, the superflow instability at the warm boundary of the heated bubble, where the liquid is still in B phase, occurs close to the  $^3\text{He}$ -B pair-breaking velocity, at  $v_{\text{cb}}(T, P) \approx v_{\text{c0}}(P) (1 - T/T_c)^{1/2}$ , where  $v_{\text{c0}}(P) = 1.61 (1 + F_1^s/3) k_B T_c / p_F$  [19]. This instability velocity is a smooth function of pressure and does not reproduce the abrupt increase of  $v_{\text{cn}}(P)$  in Fig. 12.

The fitted curves in Fig. 12, which represent  $v_{\text{cn}}(P)$  at pressures below  $P_{\text{PCP}}$ , correspond to  $v_{\text{cn}} = (\epsilon \kappa / 4\pi R_b) \ln(R_b/\xi)$ , where  $R_b = (3/2e\pi)^{1/2} (E_0/C_v T_c)^{1/3} (1 - T/T_c)^{-1/3}$ . If we assume that all of the reaction energy is transformed to heat and  $E_0 = 764$  keV, then the common fitted scaling factor  $\epsilon$  for all three curves comes out as  $\epsilon = 2.1$ . This is in agreement with the fits for the temperature dependence of  $v_{\text{cn}}$  in Fig. 11 and again suggests that the spherical thermal diffusion model is not too far off.

The largest increase in  $v_{\text{cn}}$  at  $P_{\text{PCP}}$  is observed at the highest temperature, which in Fig. 11 is  $0.96 T_c$ . This property again correlates with the notion that vortex formation is reduced and  $v_{\text{cn}}$  is increased when the stability of the A phase is boosted in the temperature and pressure range of the quench. The same reason also fits as an explanation for the dependence of  $v_{\text{cn}}$  on the applied magnetic field  $H$ , which is shown in the lower right panel of Fig. 12.

The only major influence of small fields on a quench at pressures below  $P_{\text{PCP}}$  is to make  $^3\text{He}$ -A stable in a narrow interval from  $T_c$  down to the first order AB transition at  $T_{\text{AB}}(P, H)$ . An increase in the magnetic field lowers the A-phase energy minimum with respect to that of the B phase, similar to when the pressure is increased above  $P_{\text{PCP}}$ . This translates into a reduced yield of vortex lines at any given value of the bias  $v$  and thus  $v_{\text{cn}}$  increases with magnetic field. The dependence  $v_{\text{cn}}(H)$  is reminiscent of  $T_{\text{AB}}(H)$ , the equilibrium state AB transition. Both are parabolic to first order with similar magnitudes [26]. It should perhaps be noted that the measurements in the upper right panel have not been carried out in zero magnetic field, but in 11.7 mT. This does not invalidate our conclusion since also at this field the stability regime of the A phase is much wider in temperature above  $P_{\text{PCP}}$  than below. Similarly, as shown in Fig 9, except for the increased magnitude of  $v_{\text{cn}}$ , qualitative features of vortex formation in the data of Fig. 12, such as presence of the threshold velocity and cubic increase of nucleation rate, remain essentially unchanged from the situation when the influence of the A phase is much smaller.

To summarize, we note that in the measurements the counterflow velocity  $v$  is maintained below the sponta-

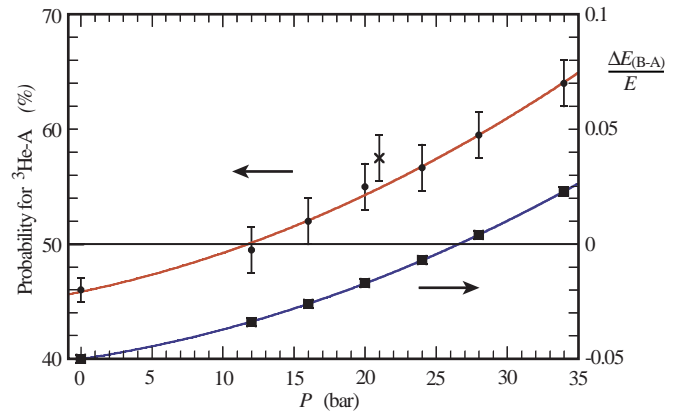


FIG. 13. Normalized energy difference,  $\Delta E/E(P)$ , between A and B phases (*right vertical axis*) and probability of A phase formation (*left vertical axis*), plotted as a function of pressure at temperatures close to  $T_c$  in the Ginzburg-Landau regime. The results have been calculated with the weak coupling  $\beta$  parameters ( $\beta_i = -1, 2, 2, 2, -2$ ), except for the data point marked with a cross ( $\times$ ) on the upper curve, for which strong-coupling parameter values have been used according to the spin fluctuation model. (From Ref. [35].)

neous critical velocity  $v_{\text{cn}}$ . At the warm boundary of the neutron bubble the bulk superflow instability velocity  $v_{\text{cb}}$  is, nevertheless, exceeded. This imposes a boundary condition which normally leads to vortex-ring formation. However, the pressure and magnetic field dependences of  $v_{\text{cn}}$  in Fig. 12 are not in accordance with this explanation of vortex-ring formation via the superfluid boundary condition.

## 8. KZ INTERPRETATION OF VORTEX FORMATION

The results in Fig. 12 suggest that the interior of the heated bubble influences the value of  $v_{\text{cn}}$ . We therefore assume that the presence of the A phase intervenes in the vortex formation process in the B-phase. This is where we need to return to the KZ argument which provides an explanation in terms of the AB interfaces which are created in the heated bubble.

Nucleation of competing phases, with different symmetries and local minima of the energy functional, has been discussed in the cosmological context [33]. It is believed that the  $SU(3) \times SU(2) \times U(1)$  symmetries of the strong, weak, and electromagnetic interactions (respectively) were united at high energy (or at high temperature). The underlying Grand Unification (GUT) symmetry ( $SU(5)$ ,  $SO(10)$ , or a larger group) was broken at an early stage during the cooling of the Universe. Even the simplest GUT symmetry  $SU(5)$  can be broken in different ways: into the phase  $SU(3) \times SU(2) \times U(1)$ , which is our world, and into  $SU(4) \times U(1)$ , which apparently corresponds to a higher energy state. However, in super-

symmetric models both phases represent local minima of almost equal depth, but are separated from each other by a high energy barrier.

In the cosmological scenario, after the symmetry break of the  $SU(5)$  GUT state both new phases are created simultaneously with domain walls between them. The calculated probability for the creation of our world — the energetically advantageous  $SO(3) \times SO(3) \times U(1)$  phase — appears to be smaller than that of the higher energy false vacuum state of  $SU(4) \times U(1)$  symmetry. Thus initially the our world state occupies only a fraction of the whole volume. Later bubbles of this energetically preferred state grow at the expense of the false vacuum state and finally completely expel it. However, before that interfaces between the two states are created in those places where blobs of both phases meet. Such interface is thus an additional topologically stable defect, which is formed in the transition process.

This situation resembles that of superfluid  $^3\text{He}$ , where the “GUT symmetry”  $SO(3) \times SO(3) \times U(1)$  can be broken to the  $U(1) \times U(1)$  symmetry of the A-phase or to the  $SO(3)$  symmetry of the B-phase, with a small energy difference between states, but separated by a high energy barrier from each other. In  $^3\text{He}$  a scenario of superfluid transition based on this analogy was discussed in Ref. [34]. It was put on quantitative ground by Bunkov and Timofeevskaya [35]. Their result shows that the energy difference between the A and B phases is small during rapid cool down through  $T_c$  and that the order parameter may settle into either the A or B-phase energy minima in different regions of the heated bubble. Blobs of size  $\xi_v$  of both A and B phases are then formed. Their relative number is not completely determined by the difference in the A- and B-phase energies: It also depends on the trajectory from the normal phase to the new energy minimum in the phase space spanned by the order parameter components. The latter aspect gives more preference to the higher energy A-phase state. The probability for the formation of the A phase state after the quench, calculated from the time dependent Ginzburg-Landau equation [35], is shown in Fig. 13. In this calculation there is no spatial dependence, an initial fluctuation is imposed at  $T_c$  into a random direction of the phase space, and the evolution towards the final state is calculated. The result shows that although the A-phase is energetically unfavorable in a wide pressure range, the probability of its formation has a value close to 50 % which is only weakly pressure dependent.

The evolution after the initial quench is similar to that in the cosmological scenario. In ambient conditions, where only B phase is stable, the A-phase blobs ultimately shrink away and only B phase remains. Before that, however, a network of AB interfaces is created which influences vortex formation. It is known from experiments on a moving AB interface that the penetration of vortex lines through the AB phase boundary is suppressed [18]. We would expect that A-phase blobs reduce the combined B-phase volume inside the bubble.

Consequently, when B-phase blobs have merged to larger units, the overall volume, into which the B-phase vortex network is confined, is smaller and B-phase vortex formation is impeded, as is shown by the increased value of  $v_{cn}$  as a function of pressure in Fig. 12.

This interpretation suggests two conclusions: First, the KZ mechanism should be the fastest process by which defects are created, before other effects of typically hydrodynamic time scale manage to switch on. In an inhomogeneous initial state with large thermal gradients the second order phase transition is turned into one where a normal-to-superfluid phase front with finite width sweeps through the heated bubble. If the velocity of the phase front,  $v_T \sim R_b/\tau_Q \sim 6$  m/s, is sufficiently high, comparable to a critical value  $v_{Tc} \sim v_F(\tau_0/\tau_Q)^{1/4}$ , then the KZ mechanism is again expected to dominate, as in the homogeneous case [13].

Secondly, the old problem [30] about the mechanism by which the first order  $A \rightarrow B$  phase transition is nucleated from supercooled  $^3\text{He-A}$  receives a new solution [34,35]. The energy barrier which separates  $^3\text{He-A}$  from  $^3\text{He-B}$  is so high that in a cool down at constant pressure, which is much above  $P_{PCP}$ , the A phase should persist down to zero temperature in a metastable state and B phase should never be formed. Nevertheless, in all experiments finally, on cooling to sufficiently low temperatures, the phase transition to  $^3\text{He-B}$  takes place, although usually much below the thermal equilibrium  $A \rightarrow B$  transition. It has been shown by Douglas Osheroff and his colleagues that the transition can be catalyzed by the localized heat input from radiation absorption [30]. From the above discussion of the KZ mechanism it is evident that in supercooled  $^3\text{He-A}$  the KZ process will lead with finite probability to the  $A \rightarrow B$  transition. Suppose that the initial state is supercooled  $^3\text{He-A}$  in ionizing radiation. The final state is the stable  $^3\text{He-B}$ , although the boundary condition favors  $^3\text{He-A}$ . The deeper the supercooling, the larger the proportion of B-phase blobs formed in the quench, and the more likely it is that many of them manage to merge together to one large bubble, which exceeds the critical diameter of about  $1 \mu\text{m}$  needed for spontaneous expansion. This then starts the  $A \rightarrow B$  transition [34,35].

To conclude, here we have a process in which a new type of defect appears: the AB interface. Normally the creation of a sizeable bubble of A phase inside bulk B liquid, for instance, requires that an AB interface of large size is formed. This is a slow and energy consuming process. Instead, in the rapid quench through  $T_c$  the AB interface appears later as a metastable defect after the freeze-out of disconnected A and B-phase blobs, which are separated by normal liquid.

## 9. BIAS DEPENDENCE OF LOOP EXTRACTION

Above we have focused on the threshold velocity, which is required to extract the first vortex loop from the heated bubble. The behavior at higher bias velocities will be described below [23]. The comparison of Eq. (6) to the KZ model allows one to make a quantitative fit, which agrees with the predicted parameter values within a factor of two. These two properties, the threshold velocity and the dependence on the bias velocity, constitute the essence in the evidence for the KZ freeze-out mechanism as the source of the observed vortices during neutron irradiation.

### a. Experimental velocity dependence

Measurements of vortex-line formation as a function of the applied counterflow velocity  $v$  allow a quantitative comparison to the KZ theory. From the NMR absorption record as a function of time during neutron irradiation at different counterflow velocities (see Fig. 3), the frequency of the discontinuities and their size can be counted: Fig. 14 shows per unit time the total number of vortex lines  $\dot{N}$  (*top*), the number of those neutron absorption events  $\dot{N}_e$  which produce at least one line and thus become observable (*middle*), and the number of lines extracted from each absorption event (*bottom*). All three rates are determined independently and directly from the absorption records.

The rates in Fig. 14 increase rapidly with the applied counterflow velocity  $v$ : At  $v/v_{cn} \approx 4.5$ , close to the maximum velocity limit imposed by the spontaneous nucleation threshold (see Fig. 11), there are almost no unsuccessful (and unobserved) absorption events left:  $\dot{N}_e(\infty) - \dot{N}_e(4.5v_{cn}) \approx 0$ . In agreement with universality property described in Sec. II-5 measurements at the two pressures of 2 and 18 bar fall on the same curves when plotted vs normalized counterflow velocity.

The rates in Fig. 14 are proportional to the intensity of the neutron flux, which is thus contained in the prefactors of the expressions in Fig. 14. For counting the rates from the NMR absorption records it is vital that absorption events do not start to overlap, when the applied counterflow velocity is increased. Therefore for the measurements in Fig. 14 three different source positions were used which were scaled to the same distance as was explained in Sec. II-5.

The most detailed information from the rate measurements is the dispersion into events in which a given number of lines is formed. In Fig. 15 we plot the rates  $\dot{N}_{ri}$  of events which produce  $i = 1-5$  lines. This data displays large statistical variation, but after averaging we get for each value of  $i$  a curve, which peaks at a maximum, and then trails off. With increasing value of  $i$  the curves shift to successively higher velocities. Starting points of each curve, threshold velocities  $v_{cni}$ , are plotted in the inset.

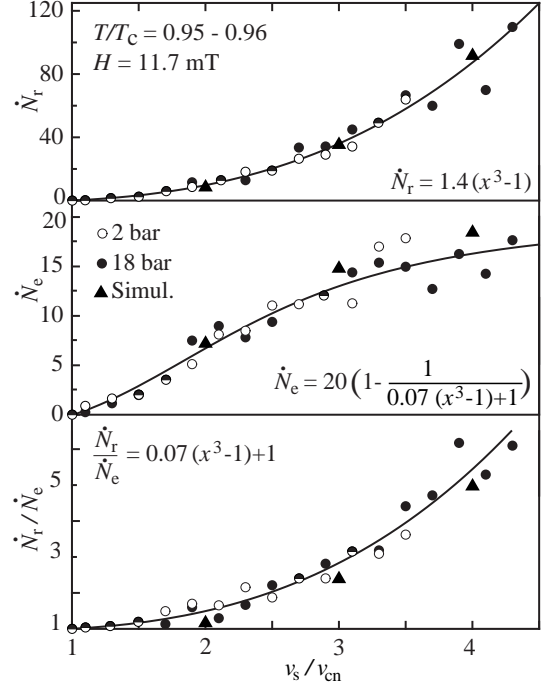


FIG. 14. Rates of vortex line formation plotted vs normalized counterflow velocity  $v/v_{cn}$ : (*Top*) the total number of lines  $\dot{N}$  formed per minute, (*middle*) the number of observed neutron absorption events  $\dot{N}_e$  per minute, and (*bottom*) the number of lines per event ( $\approx \dot{N}/\dot{N}_e$ ). All three rates have been determined *independently* from discontinuities in the NMR absorption as shown in Fig. 3. The solid curves are fits to the data, given by the expressions in each panel. (From Ref. [23].)

Their values increase with each consecutive value of  $i$ . In particular this means that at and immediately above the initial first threshold,  $v_{cn} = v_{cn1}$ , only single-vortex events occur.

A surprising finding from the measurements was the absence of a background contribution in the measured rates. A number of tests were performed to look for spontaneous events in the absence of the neutron source, to check whether a contribution from the background radiation level should be subtracted from the measured rates. For instance, a vortex-free sample was rotated for 90 min at different velocities (0.9, 1.3, and 2.1 rad/s at 2.0 bar and 0.94  $T_c$ ), but no events were ever noted.

### b. Analytic model of vortex loop escape

During the quench through the superfluid transition a random vortex network is formed, for which the length scale is the characteristic size of the order parameter inhomogeneity,  $\xi_v$ . The later evolution of the network

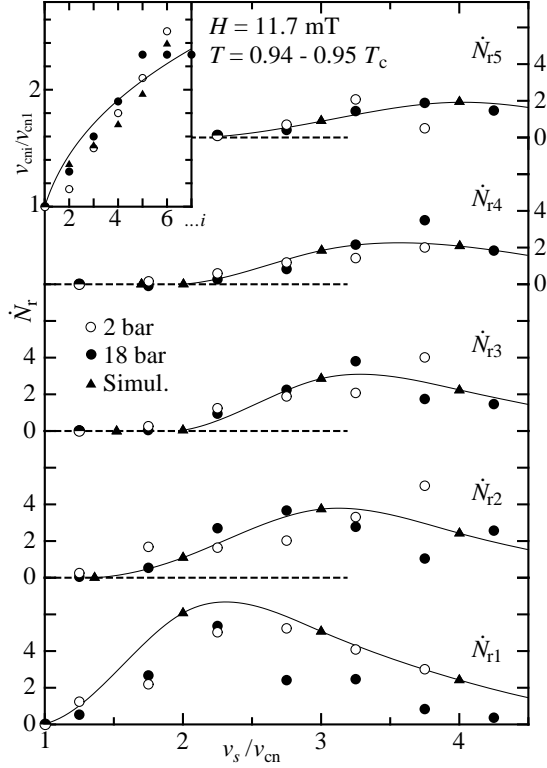


FIG. 15. Rates  $\dot{N}_i$  of vortex line formation, grouped according to the number of lines  $i$  formed per absorption event per minute, plotted vs  $v/v_{cn}$ . The solid curves are spline fits to simulation data. (*Inset*) Threshold velocity  $v_{cni}/v_{cn1}$  for the onset of an event with  $i$  lines, plotted vs the number of lines  $i$ . The solid curve represents the fit  $v_{cni}/v_{cn1} = [2.0(i-1)+1]^{1/2}$ . (From Ref. [23].)

leads to a gradual increase in this length, as have been explained in Sec. II-4a, and the average intervortex distance or the typical diameter for the curvature of the loops increases and becomes time dependent. We shall call this length  $\tilde{\xi}(t)$ . The rate of this evolution is determined by magnitude of normal-superfluid mutual friction and can be very slow at temperatures  $T \ll T_c$ . In the temperature range covered by experiments in rotating cryostat the characteristic timescale is milliseconds. Such a “coarse-graining” process may preserve the random character of the network, in other words the network remains self similar or scale invariant. Only later a change occurs in this respect, when the loops become sufficiently large to interact with the externally applied counterflow field: It causes large loops to expand, if they are oriented transverse to the flow with the correct winding direction, while in the opposite case with the wrong sign of circulation the flow causes the loops to contract.

A simple analytic calculation can be constructed for independent vortex rings in externally applied flow, which accounts for the cubic velocity dependence in the loop

escape of Fig. 14. Consider a vortex ring which is injected into homogeneous superflow. There exists a critical diameter (9) for the ring below which it contracts and above which it expands spontaneously. By comparing this diameter to the typical loop sizes in the random network, we arrive at the desired result [11].

In superfluid  $^3\text{He}$  the viscous normal component can be considered to be clamped to corotation with the container. In the rotating frame of reference we may write  $v_n = 0$  and  $v_s = v$ . The energy of a vortex loop, which is stationary with respect to the walls, is given by [17]

$$\mathcal{E} = E_{\text{kin}} + \mathbf{p} \cdot \mathbf{v} \quad , \quad (13)$$

when the loop resides in external superflow at the velocity  $\mathbf{v}$ . The hydrodynamic kinetic energy or self-energy of the loop from the trapped superfluid circulation at the velocity  $v_{s,\text{vort}}$ ,

$$E_{\text{kin}} = \frac{1}{2} \int \rho_s v_{s,\text{vort}}^2 dV = \varepsilon L \quad , \quad (14)$$

is proportional in the simple configurations to the length  $L$  of the loop and its line tension

$$\varepsilon = \frac{\rho_s \kappa^2}{4\pi} \ln \frac{\tilde{\xi}(t)}{\xi} \quad . \quad (15)$$

Here we neglect the small contribution from the core energy, use  $\tilde{\xi}(t)$  for the diameter of the loop, and the superfluid coherence length  $\xi(T, P)$  for the diameter of the core. This equation is valid in the logarithmic approximation, when  $\tilde{\xi}(t) \gg \xi(T, P)$ . While the first term in Eq. (13) is proportional to the length  $L$  of the loop, the second term involves its linear momentum,

$$\mathbf{p} = \int \rho_s \mathbf{v}_{s,\text{vort}} dV = \frac{1}{2\pi} \rho_s \kappa \int \nabla \Phi dV = \rho_s \kappa \mathbf{S} \quad , \quad (16)$$

which is proportional to the area  $S$  of the loop and oriented in the direction of the normal  $\mathbf{S}/S$  to the plane of the loop.

Thus we write for the energy of a loop

$$\mathcal{E}(l, S, t) = \rho_s \kappa \left[ L \frac{\kappa}{4\pi} \ln \frac{\tilde{\xi}(t)}{\xi} - vS \right] \quad , \quad (17)$$

where  $S$  is the algebraic area, perpendicular to the flow and of proper winding direction. This equation expresses the balance between a contracting loop due to its own line tension, which dominates at small applied velocities, and expansion by the Magnus force from the external superflow, which dominates at high applied velocities. The divide is the equilibrium condition, which was expressed by Eq. (9) and corresponds to the situation when the height of the energy barrier, which resists loop expansion, vanishes. In this extremal configuration  $\mathbf{p}$  is antiparallel to  $\mathbf{v}$ , the loop moves with the velocity  $-\mathbf{v}$  in a frame of the superfluid component, but is stationary in the rotating



frame. In a more general sense, if we consider loops in the random network which still deviate from circular shape, the extremal case degenerates to a saddle point. This is because the extremum requires also minimization with respect to deviations from circular shape, ie. the total energy is invariant under small variations of the vortex ring radius, or  $\delta\mathcal{E} = \delta E_{\text{kin}} + \mathbf{v} \cdot \delta\mathbf{p} = 0$ .

The expansion of the vortex loop should be calculated by including the mutual friction forces. In our analytic description of vortex loop escape we shall neglect such complexity. Instead we shall simply make use of three scaling relations which apply to Brownian networks in general and will be described in more detail in Sec. II-11. These expressions relate the mean values in the statistical distributions of the loop diameter  $\mathcal{D}$ , area  $S$ , and density  $n$  to the length  $l$  of the loop:

$$\mathcal{D}(L) = AL^\delta, \quad (A \approx 0.93, \delta \approx 0.47), \quad (18)$$

$$|S| = B\mathcal{D}^{2-\zeta}, \quad (B \approx 0.14, \zeta \approx 0), \quad (19)$$

$$n(L) = CL^{-\beta}, \quad (C \approx 0.29, \beta \approx 2.3). \quad (20)$$

For simplicity, these formulæ have been written in dimensionless form, by equating the common length scale to one:  $\tilde{\xi}(t) = 1$ . For a Brownian random walk in infinite space the values of  $\delta$ ,  $\beta$  and  $\zeta$  are  $1/2$ ,  $5/2$  and  $0$ .

The important assumption is that these relations are valid during whole evolution of the vortex network until sufficiently large rings are extracted by the counterflow into the bulk. Using Eqs. (18) and (19), we may write Eq. (17) for the energy of a loop in the form

$$\mathcal{E}(\mathcal{D}, t) = \rho_s \kappa \mathcal{D}^2 \left[ \frac{\kappa}{4\pi \tilde{\xi}(t) A^2} \ln \frac{\tilde{\xi}(t)}{\xi} - vB \right]. \quad (21)$$

When the mean diameter  $\tilde{\xi}(t)$  exceeds a critical size  $\tilde{\xi}_c(v_s)$ , which depends on the particular value of the applied superflow velocity  $v$ ,

$$\tilde{\xi}_c(v) = \frac{1}{A^2 B} \frac{\kappa}{4\pi v} \ln \frac{\tilde{\xi}_c}{\xi}, \quad (22)$$

the energy in Eq. (21) becomes negative and the loop starts expanding spontaneously. This is the smallest loop which will be able to expand at a given value  $v$  of the applied superflow. The upper cutoff for the loop size distribution is provided by the diameter of the entire network, or that of the heated bubble,  $2R_b$ , such that  $\tilde{\xi}_c(v_{\text{cn}}) = 2R_b$ . The total number of loops, which will be extracted from the neutron bubble, can then be obtained from

$$N = V_b \int_{\tilde{\xi}_c}^{2R_b} d\mathcal{D} n(\mathcal{D}). \quad (23)$$

Here the density distribution  $n(L) = C \tilde{\xi}^{-3/2} L^{-5/2}$ , combined with that for the average diameter  $\mathcal{D} =$

$A (L \tilde{\xi})^{1/2}$ , gives  $n(\mathcal{D}) d\mathcal{D} = 2A^3 C \mathcal{D}^{-4} d\mathcal{D}$ . On inserting this into the integral (23) we obtain

$$N = \frac{1}{9} \pi A^3 C \left[ \left( \frac{2R_b}{\tilde{\xi}_c} \right)^3 - 1 \right]. \quad (24)$$

From this equation we see that the requirement  $N(v_{\text{cn}}) = 0$  returns us the definition of the threshold velocity  $v_{\text{cn}}$ :  $\tilde{\xi}_c(v = v_{\text{cn}}) = 2R_b$ . This in turn gives us from Eq. (22) for the radius of the heated bubble

$$R_b = \frac{1}{A^2 B} \frac{\kappa}{8\pi v_{\text{cn}}} \ln \frac{2R_b}{\xi(T, P)}, \quad (25)$$

which we used in Sec. II-6a to derive the temperature dependence of the threshold velocity:  $v_{\text{cn}} \propto (1 - T/T_c)^{1/3}$ .

Eqs. (22) and (25) thus show that  $\tilde{\xi}_c \propto 1/v$  and  $R_b \propto 1/v_{\text{cn}}$ , so that we may write for the vortex-formation rate from Eq. (24)

$$\dot{N} = \frac{1}{9} \pi A^3 C \phi_n \left[ \left( \frac{v}{v_{\text{cn}}} \right)^3 - 1 \right], \quad (26)$$

where  $\phi_n$  is the neutron flux. This is the form in which the measured cubic velocity dependence was written in Eq. (6). By inserting  $A \approx 0.93$ ,  $C \approx 0.29$ , and  $\phi_n \approx 20$  neutrons/min (see panel in the middle of Fig. 14), we obtain for the prefactor in Eq. (26)  $\alpha \approx 1.6 \text{ min}^{-1}$ , which agrees with the experimental value in Figs. 10 and 14. We also realize that the definition for the threshold velocity  $v_{\text{cni}}$  follows from the requirement  $N(v = v_{\text{cni}}) \approx i$  for a process in which  $i$  rings are formed simultaneously. This gives for the threshold velocity  $v_{\text{cni}}/v_{\text{cn}} \sim i^{1/3}$ , as shown by the results in Fig. 15.

In summary, we find that the KZ model, combined with the simplest possible interpretation for the loop escape from a scale invariant random vortex network, reproduces both the measured cubic dependence on the normalized velocity,  $(v/v_{\text{cn}})^3$ , and the magnitude of the extraction rate. Similarly thermal measurements of neutron absorption events in Ref. [12], which will be discussed below, can be interpreted to yield an order of magnitude match with the KZ model.

## 10. CALORIMETRY OF VORTEX NETWORK

In Ref. [12] calorimetric measurements are described in which the amount of energy dumped into the liquid  $^3\text{He-B}$  bath is measured individually for each neutron absorption event. These measurements are performed at very low temperatures in the ballistic regime of quasiparticle motion. The measuring probe is a superconducting wire loop. It is oscillated in the liquid with a frequency of a few hundreds Hz and a high  $Q$  value, by driving the loop at resonance with an ac current in a dc magnetic field oriented perpendicular to the wire. The damping of the wire oscillation measures the density of quasiparticle

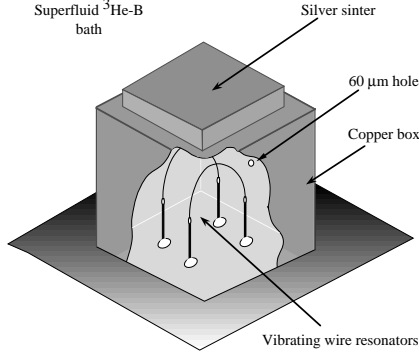


FIG. 16. Bolometer box, which is immersed in a  $^3\text{He-B}$  bath in the low temperature regime of ballistic quasiparticle motion. Two vibrating superconducting wire loops are included, one for measuring the temperature of the liquid in the box and the other as a heater to calibrate a calorimetric measurement. (From Ref. [36].)

excitations in the liquid and can be calibrated to give the temperature using the second vibrating wire loop inside the box as a heater element. It is excited with a known current pulse to heat up the liquid, by driving the wire at supercritical velocities where the break-down of Cooper pairs gives rise to a shower of quasiparticles [36].

In a calorimeter arrangement (Fig. 16) the vibrating wire resonator is built into a small closed box which is thermally connected to the surrounding liquid  $^3\text{He-B}$  bath only via a small orifice. A neutron absorption event inside the box heats up the liquid and a thermal pulse is recorded with the wire resonator. The rise time is determined by the resonator properties, while the trailing edge (with a time constant of about 1 min) monitors the much slower leakage of the quasiparticle excitations from the box through the orifice. Thus if energy is released into the helium sample with much longer time constant it won't be seen in the form of pulses by such detector.

It is found that the neutron absorption events in this setup correspond to roughly 100 keV smaller thermal pulses than 764 keV, which a slow neutron is expected to yield for the reaction with  $^3\text{He}$ . Since the various recombination channels of the ionized charge and their thermalization in liquid  $^3\text{He}$  are poorly known, it is not quite clear how large an energy deficit one should expect from these sources. Such losses include the ultraviolet radiation absorbed in the walls of the bolometer box and the retarded relaxation of excited molecular complexes. However, the authors in Ref. [12] expect that this contribution is not strongly pressure dependent and on the order of 3 % of the reaction energy. They then ascribe the remaining energy deficit to the random vortex network which is created in the neutron bubble and which in the very low temperature limit has a long life time when

mutual friction is approaching zero.

In Table I the measured missing energy at three different liquid pressures has been compared to that estimated from the KZ model. The measured result  $\Delta E_{\text{exp}}$  is recorded on the top most line while the calculated comparison proceeds stepwise from one line to the next in the downward direction of the table. The final result  $\Delta E_{\text{theor}}$  can thus be found on the lower most line. The thermal diffusion constant  $D = 3k_T/C_v = v_F^2\tau_T$  is derived from the conductivity  $k_T$ , which has been tabulated in Ref. [37] while all other basic liquid  $^3\text{He}$  values are taken from Ref. [25]. The agreement between the top and bottom lines, which is within a factor of 2, can be regarded as surprising, if we remember the many uncertain assumptions and approximations which are built into this comparison.

Table I has been included in this context to illustrate the magnitudes of the different quantities. But also, it is again indicative of the fact that rough agreement between experiment and the KZ model is apparent. In view of the many complications, which may affect the interpretation but have so far been neglected, we might wonder whether this curious agreement has some real foundation or merely happens to be fortuitous. In the next sections we shall analyze some further aspects of loop formation and escape which we now have omitted.

## 11. SIMULATION OF LOOP EXTRACTION

Although the agreement of the measured neutron-induced vortex formation with the KZ model is striking, a deeper understanding of the processes involved would be most important. Owing to its phenomenological content, the KZ model is very general and contains only few media parameters (such as the superfluid coherence length  $\xi$  or the order-parameter relaxation time  $\tau$ ). These are known in the case of superfluid  $^3\text{He}$ , hence the predictions of the model for the initial state of the vortex network can be calculated. In the rotating experiments the initial state is connected with observable quantities only through the complex evolution of the network, governed by superfluid hydrodynamics which means that numerical simulation is needed to compare quantitatively experimental results to the predictions of the model.

A number of numerical simulation studies exist today on the evolution of a network of linear defects. These apply to cosmic strings, liquid crystals, and vortices in superfluid  $^4\text{He}$ . However, these results cannot be directly transferred to neutron-induced vortex formation in  $^3\text{He-B}$ . The differences with the cosmic string and liquid crystal calculations arise from the different boundary conditions and the equations which govern the evolution of the network in the applied external bias fields. In the case of superfluid  $^4\text{He}$  studies of random vortex networks often concentrate on the properties of the normal-superfluid flow in a stationary situation [38]. In contrast, the vor-

	$P$ (bar)			Source
	0	6	19.4	
$\Delta E$ exper. (keV)	85	95	150	Ref. [12]
$T_c$ (mK)	0.93	1.56	2.22	Ref. [25]
$v_F$ ( $10^3$ cm/s)	5.95	5.04	3.94	Ref. [25]
$C_v$ [ $10^3$ erg/(cm <sup>3</sup> K)]	5.83	12.8	25.4	Ref. [25]
$\xi_0$ (nm)	65	33	18	$\xi_0 = \sqrt{7\zeta(3)/(48\pi^2)} \hbar v_F / (k_B T_c)$
$\tau_0$ (ns)	1.1	0.65	0.46	$\tau_0 = \xi_0 / v_F$
$R_b$ ( $\mu$ m)	27	17	12	$R_b = \sqrt{\frac{3}{2\pi e}} \left( \frac{E_0}{C_v(T_c - T_0)} \right)^{1/3}$
$\tau_T$ ( $\mu$ s)	0.59	0.17	0.12	Ref. [37]
$D$ (cm <sup>2</sup> /s)	21	4.3	0.94	$D = v_F^2 \tau_T$
$\tau_Q$ ( $\mu$ s)	0.16	0.31	0.69	$\tau_Q = (e/6) R_b^2 / D$
$\xi_v$ ( $\mu$ m)	0.23	0.15	0.11	$\xi_v = \xi_0 (\tau_Q / \tau_0)^{1/4}$
$N_b$	210	200	190	$N_b = \left( \frac{4}{3} \pi R_b^3 / \xi_v^3 \right)^{1/3}$
$L_v$ (cm)	79	43	28	$L_v = (4\pi/3a) R_b^3 / \xi_v^2$
$\rho_s$ (g/cm <sup>3</sup> )	0.081	0.094	0.108	$\rho_s \approx \rho$ , Ref. [25]
$\Delta E$ theor. (keV)	170	140	120	$\Delta E = (\rho_s \kappa^2 / 4\pi) L_v \ln(\xi_v / \xi_0)$

TABLE I. Comparison of measured and estimated total vortex line energies at different pressures in a random vortex network, as expected to form in a neutron absorption event according to the KZ model. The ambient temperature of the <sup>3</sup>He-B bath is taken as  $T_0 = 0.16$  mK. For value of  $\tau_Q$  the time of disappearance of normal fluid bubble is taken. Coefficient  $a = 2.1$  for calculation of the total length of vortices  $L_v$  is taken from simulations of initial vortex network (Sec. II-11a) for the value of dimensionless bubble diameter  $N_b = 200$ . (Adapted from Ref. [12].)

tex network, which is produced in <sup>3</sup>He-B in a neutron absorption event, is in a state of rapid non-stationary evolution. However, in the course of the <sup>4</sup>He studies the techniques have been developed [16] for solving accurately also the transient problem in <sup>3</sup>He-B. Here we describe preliminary calculations which concern only the universal dependence of the vortex-formation rate on the normalized counterflow velocity  $x = v/v_{cn}$  [23].

#### a. Initial loop distribution

Vachaspati and Vilenkin [6] have developed an approach for the simulation of the initial network of linear defects after a rapid phase transition, adapted for the case of cosmic strings. This technique has been used in most studies since then. Here a cubic “bubble” is subdivided into smaller cubes, such that the size of these small cubes corresponds to the characteristic length scale of the inhomogeneity in the distribution of the order parameter at the moment when the defects are formed. This length is on the order of the coherence length, in the simulation below it plays the role of a “unit” length, and is a parameter of the model, which should be calculated by other methods. In the case of the superfluid transition

this length is given by Eq. (2).

An arbitrary phase is assigned to each vertex of the grid, to model the initial random inhomogeneity of the order parameter. It is usually assumed that the distribution of the phase in each segment of the grid between two vertices corresponds to the shortest path in the phase circle, and so it is possible to determine whether a line defect pierces a given face. Then the centers of the corresponding faces are connected to form closed or open (depending upon specific boundary conditions) linear defects, strings in the cosmological case and vortices in the superfluid.

Vachaspati and Vilenkin assigned to each vertex a value of the phase from the following set:  $\{0, 2\pi/3, 4\pi/3\}$  and then studied the statistical properties of the resulting network of strings. They found that most (70%) of the strings were in the form of open segments, which extended from one boundary of the system to another. For closed loops they found two scaling relations to hold:

$$n = CL^{-\beta}, \quad (27)$$

and

$$\mathcal{D} = AL^\delta, \quad (28)$$

where  $\beta \approx -\frac{5}{2}$ ,  $\delta \approx \frac{1}{2}$ ,  $n$  is the density of loops with a

given length  $L$  and  $\mathcal{D}$  is the average spatial size of a loop, which is usually defined as an average of straight-line dimensions in  $x$ ,  $y$  and  $z$  directions. In this model both the characteristic inter-vortex distance and the radius of curvature are on the order of the length scale of the spatial inhomogeneity (i.e. the size of the small cubes, which here has been set equal to unity). Later, other variations of this model have been studied, including other types of grid and other sets of allowed phases. However, it has been found that the scaling relations (27) and (28) hold universally in each case.

The direct applicability of these results to the case of vortex formation in  $^3\text{He-B}$  is not evident. In cosmology the open lines are the most significant ones: only these strings may survive during the later evolution if no bias field exists to prevent closed loops from contracting and annihilating. In the case of a normal-liquid bubble inside a superfluid there exists an obvious boundary condition: the phase is fixed at the boundary and there are no open vortex lines at all. Thus it is of interest to find out the influence of the boundary conditions on the scaling relations (27) and (28).

Another question, which arises in the case of superfluid vortices, concerns the interaction of the loops with the external bias field due to the normal-superfluid counterflow. The energy of a tangled vortex loop in the counterflow is proportional to its algebraic area  $S = \oint y dz$  in the direction  $x$  of the counterflow velocity (17). Thus the dependence of  $S$  on the length of the loop is of interest as well.

The simulation is performed in a cubic grid with a fixed (zero) phase at the outer boundary and the set of allowed phases is not limited. It is known that such limitations affect the number of open lines in the investigations of cosmic strings, which is irrelevant for these simulations. Several vortices may pass through one cell of the grid. In this case the corresponding faces of the cell are connected in random. For calculation of the length of a loop, it is assumed that both straight and curved segments of the loop inside one cell have unit length. The size of a loop in the direction of a specific coordinate axis is measured as the number of cells in the projection of the loop along this axis.

In the case of  $^3\text{He}$  the size of the volume, which undergoes the superfluid transition in the neutron absorption event, is about  $50\text{ }\mu\text{m}$ , while the characteristic inter-vortex distance is of the order of  $1\text{ }\mu\text{m}$ . Calculations are performed for several bubble sizes: starting from  $6 \times 6 \times 6$  up to  $200 \times 200 \times 200$ . For each bubble size the loop distributions obtained from a large number of (up to 1000) realizations of the random initial phase variable in the bubble are averaged. Resulting distributions of  $n$ ,  $\mathcal{D}$  and  $S$  are shown in Fig. 17. One can see that the Vachaspati-Vilenkin relations (27) and (28) hold in the case of vortices in superfluid helium, but the exponents and prefactors are slightly different and depend on the size of the bubble. These constants also depend on the boundary conditions.

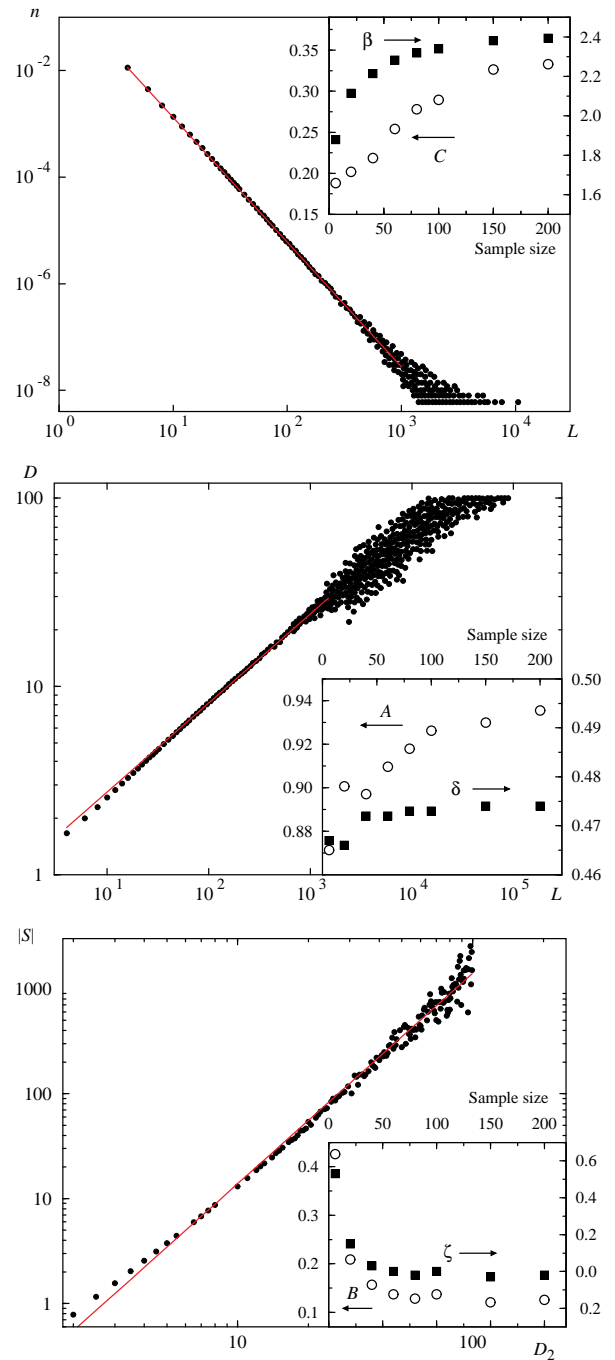


FIG. 17. Typical initial density  $n$  of vortex loops (*top*) and their average spatial size  $\mathcal{D}$  (*middle*), plotted as a function of the length  $L$  of the loops. Below their algebraic area  $|S|$  (*bottom*) is shown as a function of the 2-dimensional spatial size  $\mathcal{D}_2$  of the loop (*bottom*). The sample contains  $100 \times 100 \times 100$  cells. Solid lines are fits to the scaling laws (27), (28), and (29), respectively. The inset in each plot shows the dependences of the scaling parameters on the sample size.

For the algebraic area  $S$  of a loop as a function of the corresponding 2-dimensional diameter  $\mathcal{D}_2$  the additional scaling law is

$$|S| = B\mathcal{D}_2^{2-\zeta}, \quad (29)$$

where  $\zeta \approx 0$ . Here  $\mathcal{D}_2$  is the average of the straight-line dimensions of a loop in  $y$  and  $z$ -directions. Thus the oriented area of a tangled loop is proportional to the area of a circle of the same straight-line size. Relation (29), as well as (28), are of the form expected for a Brownian particle, for which the square of the average displacement on the  $i$ -th step is proportional to  $i$  and therefore the mean value of the square of the oriented area is given by

$$\begin{aligned} \langle S^2 \rangle &= \sum_{1 \leq i, j \leq L} \langle y_i \Delta z_i y_j \Delta z_j \rangle = \\ \sum_{i, j} \langle y_i y_j \rangle \langle \Delta z_i \Delta z_j \rangle &= \sum_i \langle y_i^2 \rangle \langle \Delta z_i^2 \rangle \propto \sum_i i \propto L^2 \end{aligned}$$

in accordance with (28) and (29).

#### *b. Network evolution under scaling assumptions*

After its formation, the dense initial vortex network evolves under the influence of the inter-vortex interactions and the normal-superfluid counterflow  $v$ , so its characteristic length scale  $\xi(t)$  increases. Vortices start to escape from the bubble only when the energy gain due to the external counterflow becomes larger than the energy of the superflow associated with the vortex itself, which corresponds to the critical value of  $\tilde{\xi}$  of about  $r_o$ , Eqs. (9), (22).

The dynamics of the vortex tangle in superfluid  $^4\text{He}$  have been studied numerically by Schwarz [16], Samuels [41], Aarts and de Waele [39], Nemirovskii [40], Barenghi [45], Tsubota [42], and others. A number of calculations have been devoted to the evolution of the initial network of cosmic strings [6] and linear defects in liquid crystals [29]. The initial state is quite similar in all three cases, but the equations controlling the evolution are different. However, their common feature is that the interaction between the loops leads to reconnections when the loops cross each other. In the most simulation works both in the case of cosmic strings and liquid crystals it was found that the scaling relations in the network of defects are preserved during the evolution. It has also been shown [28] that the scaling relations remain valid for a random vortex network if the vortices are allowed to reconnect when they cross each other, but all other interactions are neglected for simplicity.

In order to calculate the escape rate two crude assumptions are made, which are essentially the same as in analytic treatment of vortex escape problem discussed in Sec. II-9b: First, assume that in the case of vortex loops in the counterflow flow the initial scaling laws are valid until  $\tilde{\xi}$  becomes on the order of  $r_o$ . Next, assume that at this moment the influence of the external counterflow becomes immediately so significant that each loop with sufficiently small curvature expands and forms a vortex line. In the numerical simulations the state just before escape of vortices is modelled by the same method as used

to construct the initial state. It is assumed that not only the scaling relations but also the statistical properties of the vortex tangle during the evolution remain the same as in the “initial” state with the characteristic length  $\tilde{\xi}$ .

At the moment of escape,  $\tilde{\xi} \sim r_o \propto v_{\text{cn}}/v = 1/x$ , and  $\tilde{\xi}$  is used as the size of a cell in the Vachaspati-Vilenkin method. For integer values of  $x$  the bubble is represented by a grid with  $x \times x \times x$  vertices and a random phase is assigned to each vertex. In order to satisfy boundary conditions this grid is surrounded by a shell of vertices with fixed zero phase, representing the uniform bulk superfluid outside the heated bubble. Thus the whole grid contains  $(x+1) \times (x+1) \times (x+1)$  cells. Such a correspondence between the size of the grid and the velocity is not too artificial even at small values of  $x$ : for example, at the critical velocity  $v = v_{\text{cn}}$  one gets a grid with  $(x+1)^3 = 8$  cells and  $3 \times 3 \times 3$  vertices, but the phase can be non-zero only at one vertex in the middle of the grid. In this case no vortices can appear in agreement with the definition of  $v_{\text{cn}}$ .

By counting vortices for a number of random-phase distributions it is possible to calculate the probability distribution for the number of vortices escaping in one absorption event. For these calculations it is assumed that each loop, which survives until the moment when  $\tilde{\xi} \sim r_o$ , will form a detectable vortex: In the case of a tangled loop the probability is high that at least one arc is oriented favorably with respect to the counterflow and will be extracted.

The calculated probability distributions for observed neutron absorption events at different values of  $x$  ( $x = 2, 3$ , and  $4$ ) are shown in Fig. 18, expressed as the fraction of those neutron absorption events which produce a given number of vortices, normalized by the number of all events which give rise to at least one vortex. These results are in remarkably good agreement with the experimental data (without any fitting parameter). However, the agreement with the fraction of “zero” events, i.e. absorption events which produce no vortices at all, is poorer, underestimating their number especially at  $x = 2$ . Experimentally the “zero” events can be extracted from the measured data by comparing the event rate at a given rotation velocity with the saturated event rate at the highest velocity.

One reason for this discrepancy is that at low  $R_b/r_o$  ratio (i.e. at low velocities) loops with a curvature  $\sim r_o$ , which are capable of escape into the bulk superfluid, due to space constraints have a rather large probability to be oriented in such a way that they do not have sufficiently large segments oriented favorably with respect to the counterflow. Hence they would contract and wouldn't give contribution to the observed signal. Taking this into account one could develop a more elaborate technique for counting vortices than the simple “count all” method described above. In this case perfect agreement with all experimental data could be achieved (as in Fig. 14). Particularly, if only vortices with positive algebraic area with

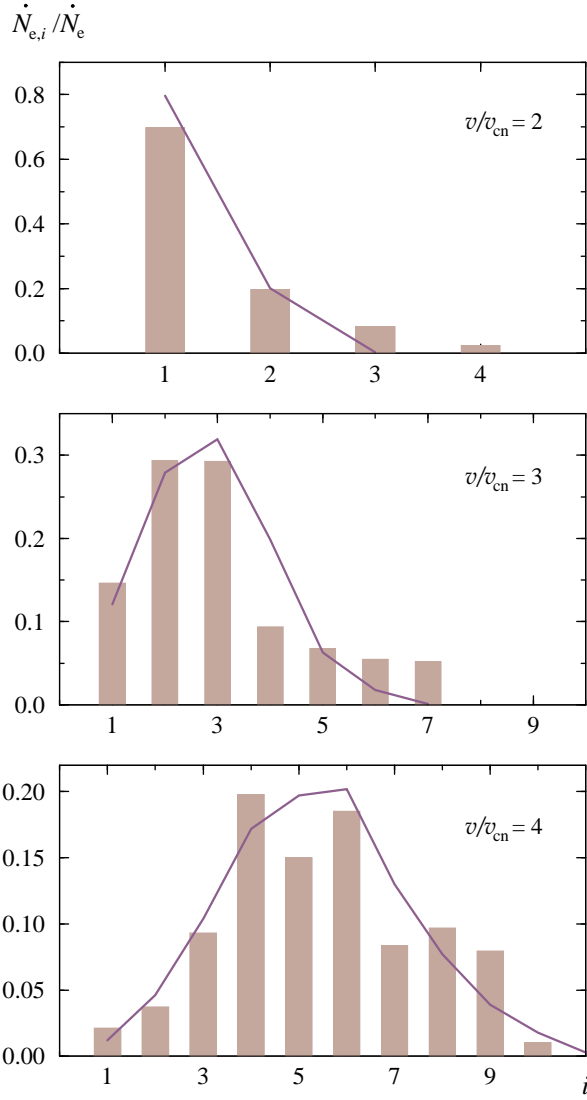


FIG. 18. The distribution of the observed neutron absorption events with respect to the number of produced vortices at different values of  $v/v_{cn}$  according to simulation (solid lines) compared to experiment (bars).

respect to the counterflow  $S = \oint y dz$  are counted, then good agreement with the amount of “zero” events would be obtained. However, all sensible modifications of the counting technique change the result by less than half of an order of magnitude. It is unreasonable to demand from the method described in this section any better accuracy.

### c. Direct simulation of network evolution

There is no direct evidence for the validity of the assumptions about the evolution of the tangle, which were made in the previous section, in particular that the network remains self-similar (i.e. scale invariant) and the

scaling laws Eqs. (27) – (29) apply during the later evolution. To verify this requires a calculation of the evolution of the vortex tangle. Some preliminary investigations in this direction based on the model developed by Schwarz for the simulation of superfluid turbulence in  $^4\text{He}$  have been carried out. This model gives good numerical agreement with experimental data in  $^4\text{He}$  [16] and have been used extensively by Schwarz and many others [39–41,45,42].

In these calculations vortices are generally considered to be 1-dimensional objects without internal structure. In  $^4\text{He}$  the diameter of the core is much smaller than other characteristic lengths, foremost the average curvature of loops or the inter-vortex distance in the tangle, and even  $\ln(\tilde{\xi}/\xi)$  can be treated as a large parameter. This is not the case in  $^3\text{He}$  due to the large coherence length, especially at the early stages of the evolution when the vortex density is the largest. However, as mentioned in Sec. II-3, the characteristic inter-vortex distance and the radius of curvature may still be several times larger than the coherence length and the diameter of the vortex core. For now, we shall continue considering the vortices as linear objects.

There are several forces acting on a vortex line in a superfluid [17]. The first contribution is the Magnus force from the superflow

$$\mathbf{f}_M = \rho_s \kappa \nu \mathbf{s}' \times (\mathbf{v}_L - \mathbf{v}_{sl}), \quad (30)$$

where  $\mathbf{s}$  is the radius vector of a point on the vortex line with the circulation quanta  $\nu$ , the prime denotes the derivative with respect to the length of the line (the natural parameter),  $\mathbf{v}_L = \dot{\mathbf{s}}$  is the local velocity of the vortex line, and  $\mathbf{v}_{sl}$  is a local superfluid velocity at this point. In the case of singular vortices in  $^3\text{He-B}$   $\nu = 1$ , but we retain it for the purpose of more general discussion later. The value of  $\mathbf{v}_{sl}$  is a sum of the superfluid velocity  $\mathbf{v}_s$  far from the vortex tangle and the velocity induced by all the vortex loops:

$$\mathbf{v}_{sl}(\mathbf{r}) = \mathbf{v}_s + \frac{\kappa}{4\pi} \int_{\text{all loops}} \frac{(\mathbf{s} - \mathbf{r}) \times d\mathbf{s}}{|\mathbf{s} - \mathbf{r}|^3}. \quad (31)$$

The Iordanskii force, which comes from the Aharonov-Bohm scattering of quasiparticles from the velocity field of the vortex, is

$$\mathbf{f}_{\text{Iordanskii}} = \rho_n \kappa \nu \mathbf{s}' \times (\mathbf{v}_L - \mathbf{v}_n) \quad (32)$$

where  $\mathbf{v}_n$  is the velocity of the normal component (heat bath of the fermionic quasiparticles). The Kopnin or spectral flow force has the same form, but it comes from the spectral flow of the quasiparticle levels in the vortex core:

$$\mathbf{f}_{\text{sf}} = m_3 \mathcal{C}(T) \kappa \nu \mathbf{s}' \times (\mathbf{v}_L - \mathbf{v}_n) \quad (33)$$

where the temperature dependent parameter  $\mathcal{C}(T)$  determines the spectral flow in the core.

All three forces above are of the topological origin: they are transverse and thus nondissipative. In the case of the Fermi superfluids and superconductors they can be related to different topological forces acting on the cosmic strings from the environment: (i) Analog of the Magnus force  $\mathbf{f}_M$  acts on the Nielsen-Olesen cosmic string from the electrically charged background; (ii) The Iordanskii force  $\mathbf{f}_{\text{Iordanskii}}$  has the same origin as the gravitational Aharonov-Bohm effect caused by spinning cosmic strings on the scattered fermions and bosons; and (iii) The spectral flow force  $\mathbf{f}_{\text{sf}}$  comes from the same effect of axial anomaly, which leads to the baryogenesis and leptogenesis mediated by electroweak strings. This analogy is explained in more details in Sec. III-1.

The nontopological friction force  $\mathbf{f}_{\text{fr}}$  is longitudinal being proportional to the vortex velocity with respect to the heat bath. It may be written in the form

$$\mathbf{f}_{\text{fr}} = -d_{\parallel} \rho_s \kappa \nu \mathbf{s}' \times [\mathbf{s}' \times (\mathbf{v}_n - \mathbf{v}_L)], \quad (34)$$

where the factor  $\rho_s \kappa \nu$ , entering Magnus force is separated.

Together with the three topological forces and neglecting the vortex mass this gives the force balance acting on vortex:

$$\mathbf{f}_M + \mathbf{f}_{\text{Iordanskii}} + \mathbf{f}_{\text{sf}} + \mathbf{f}_{\text{fr}} = 0 \quad (35)$$

It is convenient for our calculations to rewrite the balance of forces governing the dynamics of a segment of vortex line in the following form:

$$\mathbf{s}' \times [(\mathbf{v}_L - \mathbf{v}_{sl}) - \alpha'(\mathbf{v}_n - \mathbf{v}_{sl})] = \alpha \mathbf{s}' \times [\mathbf{s}' \times (\mathbf{v}_n - \mathbf{v}_{sl})] \quad (36)$$

where  $\alpha$  and  $\alpha'$  are dimensionless mutual friction coefficients. These  $\alpha$  parameters are what is actually measured experimentally in the mutual friction experiments (see e.g. [62]). The inverse  $\alpha$  parameters are the  $d$  parameters:

$$\alpha + i(1 - \alpha') = \frac{1}{d_{\parallel} - i(1 - d_{\perp})}, \quad (37)$$

where  $i = \sqrt{-1}$ . The transverse mutual friction parameter  $d_{\perp}$  is expressed via three functions of temperature which determine Magnus, Iordanskii and spectral-flow forces:

$$d_{\perp}(T) = (m_3 \mathcal{C}(T) - \rho_n(T)) / \rho_s(T) \quad (38)$$

The Eq.(36) is complicated because of the term with the integral (31). To solve it, one may follow Schwarz and neglect the influence on  $\mathbf{v}_{sl}$  of all loop segments except the one containing the point of interest (the so called local self-induced approximation). In this case  $\mathbf{v}_{sl} \approx \mathbf{v}_s + \beta \mathbf{s}' \times \mathbf{s}''$ , where  $\beta = \kappa / (4\pi) \ln(\tilde{\xi} / \xi)$ . The leading contribution to the error in this approximation comes from the nearest neglected vortex segments and can be estimated to be of

order  $\tilde{\xi} / [b \ln(\tilde{\xi} / \xi)]$ , where  $b$  is the average inter-vortex distance. In the case of vortex network in  $^3\text{He}$   $\tilde{\xi} \sim b$  and  $\ln(\tilde{\xi} / \xi) \sim 1$  at an early stage of the evolution and thus at this point the approximation is rather crude. However, the main effect at the initial stage of the evolution arises from the reconnection of crossing vortex lines. This effect is taken into account below.

Furthermore,  $\alpha' \ll \alpha$  close to  $T_c$  and we may rewrite the equation of vortex motion in the form:

$$\dot{\mathbf{s}} = \mathbf{v}_s + \beta \mathbf{s}' \times \mathbf{s}'' + \alpha \mathbf{s}' \times [(\mathbf{v}_n - \mathbf{v}_s) - \beta \mathbf{s}' \times \mathbf{s}'']. \quad (39)$$

Comparison to the experimental results is done at  $P = 18$  bar and  $T = 0.96 T_c$ , where the most detailed data have been obtained. Under these conditions  $\alpha \approx 10$  [43] and Eq. (39) can be simplified further:

$$\dot{\mathbf{s}} = \alpha \beta \mathbf{s}'' + \alpha \mathbf{s}' \times \mathbf{w} \quad (40)$$

where  $\mathbf{w} = \mathbf{v}_n - \mathbf{v}_s$  is the counterflow velocity. In the reference frame where the superfluid component is at rest one has  $\mathbf{v}_s = 0$ ,  $\mathbf{v}_n = \mathbf{w}$ . The first term on the right of Eq. (40) causes a loop to shrink while the second represents growth or shrinking, depending upon the orientation of the loop with respect to the counterflow.

In numerical calculation vortices are considered as lines in the same 3-dimensional lattice as before. The temporal and spatial coordinates are discrete and therefore the network evolves in discrete steps: On each time step a vertex of a loop can jump to one of the adjacent vertices of the lattice. The probability of a jump in any direction is proportional to the component of  $\dot{\mathbf{s}}$  (40) in this direction, so that the average velocity equals  $\dot{\mathbf{s}}$ . Other, more elaborated representations of vortex loops based on splines are known, which model the dynamics of smooth vortex lines in the continuous space. However, for this preliminary study of the evolution of the tangle it is reasonable to use the simple and crude lattice representation which, nevertheless, seems to give qualitatively correct results. At least the simple case of a circular loop in counterflow, where the result is known analytically, is reproduced correctly.

It is well known that the interactions between the close segments of vortex loops play an important role in the evolution of a dense vortex network. These interactions lead to the reconnection of loops which cross each other. The reconnections are main source for the rarefaction and smoothing out of the network and cause the characteristic inter-vortex distance  $\xi$  to increase with time. The reconnection process has been studied numerically [16,44] and was found to occur with a probability approaching unity. In these simulations the vertices are connected such a way that closed loops are obtained after each time step during the evolution. If a cell is pierced by two vortices, the two segments coming in and the two segments going out are connected in a random fashion. This corresponds to a reconnection probability of 0.5. It is reasonable to suppose that this convention leads to a slowing

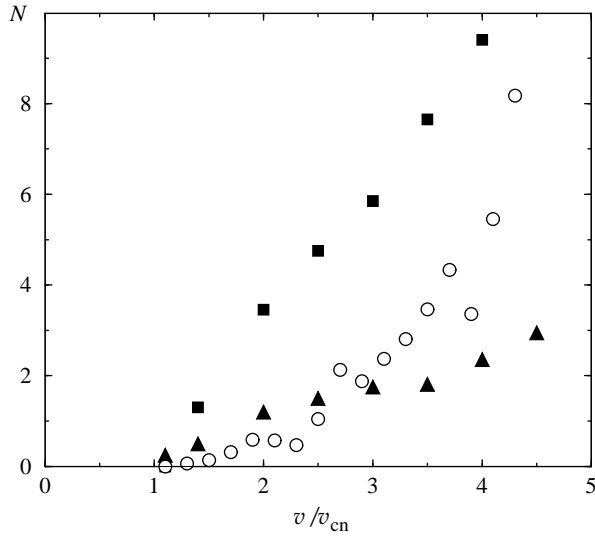


FIG. 19. The number of vortices  $\mathcal{N}$  generated by one absorbed neutron as a function of  $v/v_{cn}$ : (■) simulation of the network evolution in the local self-induced approximation and (▲) by including in addition approximately the polarization of the tangle by the superflow. The experimental data (○) represent measurements at  $P = 18$  bar and  $T = 0.96 T_c$  [11].

down in the evolution, in particular in the initial phase, but does not produce gross qualitative changes.

The vortex tangle is initially produced by the procedure described in Sec. II-11b, in a lattice  $40 \times 40 \times 40$ , and its evolution is followed until all vortices had disappeared or some loops had expanded and formed circular planar loops far from their location of origin. At this point these large loops are counted, since it is fair to assume that each one of them will produce a detectable rectilinear vortex line in the rotating container. This calculation is repeated for a large number of random initial phase distributions at any given value of  $v$ . The results are averaged to obtain the average number of vortices  $\mathcal{N}$ , produced by one neutron as a function of  $v$ , and are compared to experimental data in Fig. 19. It is also possible to study the validity of the scaling law (27), at different stages of the evolution in the course of these simulations. In the absence of counterflow ( $v = 0$ ) it is found that the relation is valid for large loops,  $L > 4\tilde{\xi}$ , at least during a large part of the early evolution (in the late phase, when  $n$  approaches zero the statistical noise exceeds  $n$ ).

Fig. 19 illustrates some results from the simulation (data points denoted with (■)): No vortices are obtained at low counterflow velocity  $v < v_{cn}$ , but when  $v > v_{cn}$ , their number  $\mathcal{N}$  starts to increase rapidly with  $v$ . The value  $v_{cn}$  of the threshold velocity corresponds to the situation when the largest radius of curvature  $r_o(v_{cn})$  becomes equal to the diameter of the initial volume of the vortex network (i.e. the diameter of the heated bubble). It then becomes possible for a loop to escape into the bulk superfluid if it has at least one arc with sufficiently large radius of curvature  $\geq r_o$ . The same calculations

have also been performed for a tangle with an initial size of  $20 \times 20 \times 20$  and found no difference has been found in the dependence  $\mathcal{N}(v/v_{cn})$ . This is additional circumstantial evidence for the fact that the scaling relations survive during the evolution of the network in the counterflow and that the network remains scale invariant.

The experimental data (denoted with (○) in Fig. 19) fit the universal dependence  $\mathcal{N}(v/v_{cn}) \approx \tilde{\alpha}[(v/v_{cn})^3 - 1]$ , where  $\tilde{\alpha}$  equals  $\alpha$  in Eq. (6) divided by neutron flux. Numerical results lie appreciably higher (note that no fitting parameters are involved) and they do not display a cubic dependence in the experimental range  $1 < v/v_{cn} < 4$ . These differences can be explained by the approximations in the expression for  $\mathbf{v}_{sl}$ : particularly neglect of a much too significant contribution from the inter-vortex interactions. The external counterflow causes the loops with unfavorable orientation to contract and loops with the proper winding direction and orientation to grow. Thus the superflow produces a polarization of the vortex tangle. The polarization in turn screens the vortex tangle from the external counterflow. In order to check whether the polarization has a significant effect on the result, the calculations have been repeated with an approximate account for the screening in the expression for  $\mathbf{v}_{sl}$ :

$$\mathbf{v}_{sl} = \mathbf{v}_s + \beta \mathbf{s}' \times \mathbf{s}'' + \frac{\kappa}{4\pi} \int_{\text{other loops}} \frac{1}{V} \int d\mathbf{r} \frac{(\mathbf{s} - \mathbf{r}) \times d\mathbf{s}}{|\mathbf{s} - \mathbf{r}|^3}. \quad (41)$$

Here the contribution from each loop to the superflow is averaged over the volume. The results (denoted with (▲) in Fig. 19) show that this effect is significant and should be more accurately taken into account for a correct simulation of the network evolution. It is likely that this can be done in the nearest future as new progress in computer hardware makes “brute force” simulations of the vortex-tangle dynamics possible in such a form that non-local interactions (31) can be accounted for in full (see eg. [45]).

To summarize we note that this preliminary simulation work shows that it is possible to obtain good numerical agreement between the KZ vortex formation mechanism and the experimental data if one assumes that the scaling relations of the initial vortex tangle remain valid also during the later evolution of the vortex tangle in the superflow. This assumption should still be checked with sufficiently accurate simulation of the network evolution with full account for non-local inter-vortex interactions. Future simulation work should then answer the question how much information about the initial state of the vortex tangle can be retrieved from the experiment, where only the final stationary state result is measured.



## 12. SUPERFLUID TRANSITION AS A MOVING PHASE FRONT

In any real laboratory system a rapid phase transition becomes inhomogeneous: The transition will be driven by a strong gradient in one or several of the externally controlled variables. In the case of the superfluid transition in the aftermath of a neutron absorption event it is a steep and rapidly relaxing thermal gradient. In this situation even a second order transition becomes spatially inhomogeneous and is localized into a phase front. In the limit of very fast transitions the order-parameter relaxation slows down the propagation of the superfluid phase and the thermal front, where the temperature drops below  $T_c$ , may escape ahead. The moving phase boundary breaks down into a leading thermal front and a trailing superfluid interface. The width of the region between these two zones is determined by the relative velocities of thermal and superfluid relaxation. Thermal fluctuations in this intermediate region are amplified in the transition process and are carried over as order-parameter inhomogeneity into the new symmetry-broken phase. This is the central claim of the KZ model. Below we shall briefly discuss the influence of the thermal gradient on defect formation, as analyzed in Refs. [13,47].

### *a. Neutron bubble and heating*

The two decay products from the neutron absorption reaction generate ionization tracks which can be estimated from a standard calculation of stopping power [14]. This leads to a cigar-shaped volume of ionized particles, with the largest concentration at the end points of the two tracks. The probabilities and relaxation times of the different recombination channels for the ionized charge are not wellknown in liquid  $^3\text{He}$ . The thermalization of the reaction energy may not produce a heated region which preserves the shape of the original volume with the ionized charge.

The majority of the recombination processes are expected to lead to particles with large kinetic energies in the eV range, which are well outside the thermal distribution and for which the recoil velocities become more and more randomly oriented. Very energetic particles suffer collisions with their nearest neighbors and the mean free path only slowly increases for atoms participating in these collisions, until all particles are slowed down and become thermalized to the ambient conditions [35]. This means that the reaction energy remains initially localized. In the calorimetric experiments at the lowest temperatures [12] the thermal mean free path exceeds the container dimensions. Nevertheless, the energy is not immediately dispersed into a large volume, but remains centralized within the bubble of limited size during cooling through  $T_c$ , when the vortex network is formed. This is the conclusion to be drawn from the comparison between

experiment and the KZ mechanism in Table I, where it is assumed that the thermal diffusion mean free path is the same as in the normal fluid at  $T_c$ .

In contrast, if the majority of the kinetic energy is assumed to be thermalized by quasiparticles with energies comparable to the high-energy tail of the thermal Maxwellian velocity distribution, then the mean free paths are long, the volume heated above the ambient becomes large and its temperature distribution may even become nonmonotonic like in a “Baked Alaska”, as has been described by Leggett [31]. The Baked Alaska scenario is also popular in high energy physics, where the formation of the false vacuum with the chiral condensate after hadron-hadron collision is considered [32]. In both cases a rather thin shell of the radiated high energy particles expands with the speed of light in a relativistic system and with the Fermi velocity  $v_F$  in  $^3\text{He}$ , leaving behind a region at reduced  $T$ . Since this interior region is separated from the exterior vacuum by the hot shell, the cooldown into the broken symmetry state in the interior region is not biased by the order parameter in the exterior region. The Baked Alaska mechanism thus can solve the problem of neutron-mediated formation of the B-phase in bulk A-phase [31], while in high energy physics it opens the possibility for the formation of the bubble of the chiral condensate in a high energy collision [32].

In such conditions, when the quasiparticle mean free path is comparable to the dimensions of the heated bubble, temperature is not a useful quantity for the description of the heating effect. Most of the analysis of the previous sections is applicable only if we assume that the reaction energy remains reasonably well localized while the hot bubble cools through  $T_c$ . In this case there is no Baked-Alaska effect: no hot shell separating the interior region from the exterior. So the exterior region can effectively fix the phase in the cooled bubble, suppressing the formation of the vacuum states, which are different from that in the bulk liquid, and in the same manner suppressing the formation of vortices. However it appears that there is an alternative mechanism: the influence of the exterior region is not effective if the phase transition front moves sufficiently rapidly [13,47]. We discuss this phenomenon below.

For the interpretation of the measurements, a sophisticated understanding of the shape and size of the constant temperature contours within the heated bubble is not vitally necessary. In the final results the bubble size does not enter, since the data can be normalized in terms of the measured threshold velocity  $v_{cn}$ . Its measurement provides an estimate of the circumference of the bubble, since the largest possible vortex ring has to be comparable in size to the neutron bubble. The diameter of this ring is at least 1 – 2 orders of magnitude larger than expected in the KZ model for the average intervortex distance  $\xi_v$  in the initial random network at freeze out.

*b. Thermal gradient and velocity of phase front*

For a rough understanding of the superfluid transition in a temperature gradient let us consider the time dependent Ginzburg-Landau (TDGL) equation for the one-component order parameter  $\Psi = \Delta/\Delta_0$ :

$$\tau_0 \frac{\partial \Psi}{\partial t} = \left(1 - \frac{T(\mathbf{r}, t)}{T_c}\right) \Psi - \Psi |\Psi|^2 + \xi_0^2 \nabla^2 \Psi \quad (42)$$

where the notations for  $\tau_0 \sim 1/\Delta_0$  and  $\xi_0$  are the same as before in Sec. III. This equation is the so called overdamped limit of the more general TDGL equation with the second time derivative, which was used for the numerical simulation [48] and analytical estimation [49] of the density of the topological defects formed after a homogeneous quench. If the quench occurs homogeneously in the whole space  $\mathbf{r}$ , the temperature depends only on one parameter, the quench time  $\tau_Q$ :

$$T(t) = \left(1 - \frac{t}{\tau_Q}\right) T_c \quad (43)$$

In the presence of a temperature gradient, say, along  $x$ , a new parameter appears, which together with  $\tau_Q$  characterizes the evolution of the temperature:

$$T(x - v_T t) = \left(1 - \frac{t - x/v_T}{\tau_Q}\right) T_c \quad (44)$$

Here  $v_T$  is the velocity of the temperature front which is related to the temperature gradient [13]

$$\nabla_x T = \frac{T_c}{v_T \tau_Q} \quad (45)$$

With this new parameter two regimes of slow and fast front propagation appear. At slow velocities,  $v_T \rightarrow 0$ , the order parameter moves in step with the transition temperature front:

$$|\Psi(x, t)|^2 = \left(1 - \frac{T(x - v_T t)}{T_c}\right) \Theta(1 - T(x - v_T t)/T_c) \quad (46)$$

Here  $\Theta$  is the step function. In this case the phase coherence is preserved behind the transition front and thus no defect formation is possible.

The opposite regime of large velocity of the temperature front,  $v_T \rightarrow \infty$ , corresponds to the homogeneous quench. In this extreme case the phase transition front cannot follow the temperature front: it lags behind [47]. In the space between these two boundaries the temperature is already below the phase transition temperature,  $T < T_c$ , but the phase transition did not yet happen, and the order parameter is still not formed,  $\Psi = 0$ . This situation is unstable towards the formation of bubbles of the new phase with  $\Psi \neq 0$ . This occurs independently

in different regions of the space, leading to vortex formation according to the KZ mechanism. At a given point of space  $\mathbf{r}$  the development of the instability can be found from the linearized TDGL equation, since during the initial growth of the order parameter  $\Psi$  from zero the cubic term can be neglected:

$$\tau_0 \frac{\partial \Psi}{\partial t} = \frac{t}{\tau_Q} \Psi \quad (47)$$

This gives an exponentially growing order parameter, which starts from some seed  $\Psi_{\text{fluc}}$ , caused by fluctuations:

$$\Psi(\mathbf{r}, t) = \Psi_{\text{fluc}}(\mathbf{r}) \exp \frac{t^2}{2\tau_Q \tau_0} \quad (48)$$

Because of the exponential growth, even if the seed is small, the modulus of the order parameter reaches its equilibrium value  $|\Psi_{\text{eq}}| = \sqrt{1 - T/T_c}$  after the Zurek time  $t_{\text{Zurek}}$

$$t_{\text{Zurek}} = \sqrt{\tau_Q \tau_0} \quad (49)$$

This occurs independently in different regions of space and thus the phases of the order parameter in each bubble are not correlated. The spatial correlation between the phases becomes important at distances  $\xi_v$  where the gradient term in Eq. (42) becomes comparable to the other terms at  $t = t_{\text{Zurek}}$ . Equating the gradient term  $\xi_0^2 \nabla^2 \Psi \sim (\xi_0^2/\xi_v^2) \Psi$  to, say, the term  $\tau_0 \partial \Psi / \partial t|_{t_{\text{Zurek}}} = \sqrt{\tau_0/\tau_Q} \Psi$ , one obtains the characteristic Zurek length scale which determines the initial distance between the defects which is the same as in Eq. (2):

$$\xi_v = \xi_0 (\tau_Q/\tau_0)^{1/4} \quad (50)$$

We can estimate the lower limit of the characteristic value of the fluctuations  $\Psi_{\text{fluc}} = \Delta_{\text{fluc}}/\Delta_0$ , which serve as a seed of the vortex formation. If there is no other sources of fluctuations, caused say by external noise, the initial seed is provided by the thermal fluctuations of the order parameter in the volume  $\xi_v^3$ . The energy of such fluctuation is  $\xi_v^3 \Delta_{\text{fluc}}^2 N_F / E_F$ , where  $E_F \sim T_F$  is the Fermi energy and  $N_F$  the fermionic density of states in the normal Fermi liquid. Equating this energy to the temperature  $T \approx T_c$  one obtains the magnitude of the thermal fluctuations of the order parameter

$$\frac{|\Psi_{\text{fluc}}|}{|\Psi_{\text{eq}}|} \sim \left(\frac{\tau_0}{\tau_Q}\right)^{1/8} \frac{T_c}{E_F} \quad (51)$$

The same small parameter  $T_c/E_F \sim a/\xi_0 \sim 10^{-3} - 10^{-2}$  enters here, which is responsible for the extremely narrow temperature region of the critical fluctuations in  $^3\text{He}$  near  $T_c$ . But in our case it only slightly increases the Zurek time by the factor  $\sqrt{\ln |\Psi_{\text{eq}}|/|\Psi_{\text{fluc}}|}$  and thus does not influence the vortex formation in the regime of the homogeneous quench, corresponding to the large velocity of the temperature front.

Now it is clear that there exists a characteristic critical velocity  $v_{T_c}$  of the propagating temperature front, which separates the fast and slow regimes, or with and without defect formation, correspondingly. The criterium for the defect formation is that the Zurek time  $t_{\text{Zurek}} = \sqrt{\tau_Q \tau_0}$  should be shorter than the time  $t_{\text{sw}}$  in which the phase transition front sweeps through the space between the two boundaries. The latter time is  $t_{\text{sw}} = x_0/v_T$ , where  $x_0$  is the lag – the distance between the transition temperature front and the region where the superfluid coherence starts (the order parameter front). If  $t_{\text{Zurek}} < t_{\text{sw}}$  the instability has time to develop. If  $t_{\text{Zurek}} > t_{\text{sw}}$  there is no instability: both fronts move coherently and phase of the coherence is continuous. Let us consider such "laminar" motion and find out how the lag  $x_0$  depends on  $v_T$ . Then from the equation  $t_{\text{Zurek}} = x_0(v_{T_c})/v_{T_c}$  we find the criterion for the threshold of the instability of laminar motion and thus for defect formation.

In the steady laminar motion the order parameter depends on  $x - v_T t$ . Introducing a dimensionless variable  $z$  and a dimensionless parameter  $a$ ,

$$z = (x - v_T t)(v_T \tau_Q \xi_0^2)^{-1/3}, \quad a = \left( \frac{v_T \tau_0}{\xi_0} \right)^{4/3} \left( \frac{\tau_Q}{\tau_0} \right)^{1/3}, \quad (52)$$

one obtains the linearized TDGL equation in the form:

$$\frac{d^2 \Psi}{dz^2} + a \frac{d\Psi}{dz} - z\Psi = 0, \quad (53)$$

or

$$\Psi(z) = \text{const} \cdot e^{-az/2} \chi(z), \quad \frac{d^2 \chi}{dz^2} - \left( z + \frac{a^2}{4} \right) \chi = 0 \quad (54)$$

This means that  $\Psi$  is an Airy function  $\chi(z - z_0)$ , centered at  $z = z_0 = -a^2/4$ , which is attenuated by the exponential factor  $e^{-az/2}$ .

If  $a \gg 1$ , then it follows from Eq. (54) that  $\Psi(z)$  quickly vanishes with  $z$  increasing above  $-a^2/4$ . So there is a supercooled region  $-a^2/4 < z < 0$ , where  $T < T_c$ , but the order parameter is absent: the solution is essentially  $\Psi = 0$ . Thus the lag between the order parameter front and the front of the transition temperature is  $|z_0| = a^2/4$ , which in conventional units is

$$x_0 = \frac{1}{4} \frac{v_T^3 \tau_Q \tau_0^2}{\xi_0^2}. \quad (55)$$

Now from the equation  $t_{\text{Zurek}} = x_0(v_{T_c})/v_{T_c}$  one can estimate the critical value of the velocity of the temperature front, at which the laminar propagation becomes unstable:

$$v_{T_c} \sim \frac{\xi_0}{\tau_0} \left( \frac{\tau_0}{\tau_Q} \right)^{1/4} \quad (56)$$

This corresponds to  $a \sim 1$  and is in agreement with the result obtained from scaling arguments in Ref. [13]. Here we cannot find an exact numerical value for the threshold of the instability, but this can in principle be done using the complete TDGL equation. This work is now in progress [47].

For the neutron bubble we might take  $v_T \sim R_b/\tau_Q$ , which makes  $v_T \sim 10$  m/s. The critical velocity  $v_{T_c}$  we can estimate to possess the same order of magnitude value. This estimation suggests that the thermal gradient should be sufficiently steep in the neutron bubble such that defect formation can be expected.

### 13. QUENCH OF PREEXISTING VORTICES

#### *a. Vortices on microscopic and macroscopic scales.*

Onsager was the first, who interpreted the superfluid-normal transition at  $\lambda$ -point in  $^4\text{He}$  in terms of quantized vortices: when the concentration of the thermally activated quantized vortices reaches the point where they form a connected tangle through the liquid, the liquid becomes normal [50] (see Fig. 20). The infinite vortex cluster destroys the superfluidity, since the phase slippage processes caused by the back reaction of vortex cluster to the superfluid current lead to decay of the superfluid current.

In the Ginzburg-Landau theory the vortices are identified as lines of zeroes of the scalar complex order parameter  $\Psi = |\Psi|e^{i\varphi}$  about which the phase winding number  $\nu$  is nonzero. Above the transition, in the symmetric phase, the thermal fluctuations of the order parameter give rise to an infinite cluster of zeroes – vortices who live in the microscopic scale but are absent on the macroscopic scale since in the symmetric phase the long range order is absent. The behavior of such microscopic vortices – topologically nontrivial zeroes – across the thermodynamic phase transition was numerically investigated in [52,53,51]. The renormalization group (RG) description of the phase transition, based on the Ginzburg-Landau free energy functional (see e.g. [58]), also contains the microscopic quantized vortices, but in the implicit form of zeroes.

There was an attempt [55,56] to reformulate the RG scheme of the 3-dimensional phase transition directly in terms of vortices, in the manner as it was made for the 2-dimensional case of Berezinskii-Kosterlitz-Thouless transition [57], i.e. avoiding the consideration of the Ginzburg-Landau free energy functional. It is possible, though it is not proven, that the Ginzburg-Landau model and the vortex model belong to the same universality class and thus give the same critical exponents for the heat capacity and superfluid density. Note that the earlier ground and space experiments [59] are consistent with the theoretical estimations, based on RG Ginzburg-Landau scheme [58], but some disagreement with theory

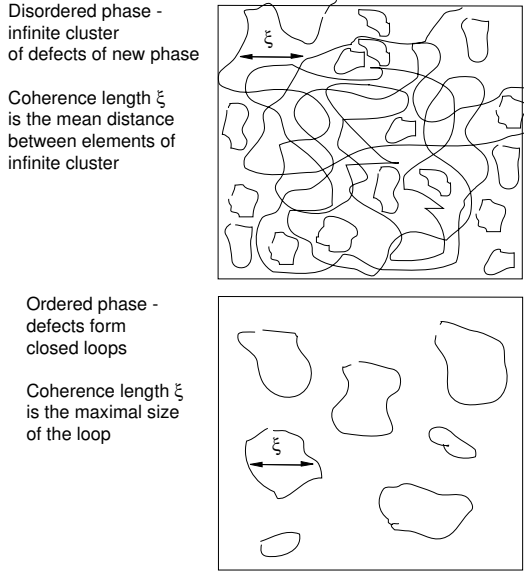


FIG. 20. Infinite-finite vortex cluster

was found in recent space experiments [60].

While in the equilibrium phase transition the infinite cluster disappears below  $T_c$ , in the nonequilibrium phase transition this cluster of microscopic vortices persists even in the ordered phase due to the critical slowing down. These vortices finally transform to the conventional macroscopic vortices, when the latter become well defined. In this language the Kibble-Zurek mechanism corresponds to the quench of the infinite cluster across the nonequilibrium phase transition from the normal to superfluid phase [54]. What is important for us is the scaling law for the distribution of vortices. According to the numerical simulation [52,53] and the phenomenological vortex model [55,56] the scaling exponent  $\delta$ , which characterizes the distribution of vortex loops in Eq.(28), is close to the value  $\delta = 2/(d+2) = 0.4$  first obtained by Flory for self-avoiding polymers. It is different from the value given by the Vachaspati-Vilenkin model of random phases. On the other hand one may expect that this is applied within the Ginzburg region of the critical fluctuations and thus is valid for  $^4\text{He}$ , rather than for  $^3\text{He}$ .

#### b. Scaling in equilibrium phase transition.

The difference between the phase transitions in  $^4\text{He}$  and  $^3\text{He}$  is important also for the other phenomena, that is why let us recall this difference. The temperature region of the critical fluctuations, where the simple Ginzburg-Landau theory does not work and one must introduce the thermal renormalization of the Ginzburg-Landau functional, can be obtained from the following simplified considerations. Let us estimate the length  $L_T$  of the thermal vortex loop, i.e. the loop which energy is comparable with the temperature:

$$\rho_s(T) \frac{\kappa^2}{4\pi} L_T \ln \left( \frac{L_T}{\xi(T)} \right) = T \approx T_c. \quad (57)$$

In the broken symmetry phase far below  $T_c$ , this length is less than the coherence length  $\xi$ , which means that there are no real vortices with the energy of order  $T$ , while the vortices with higher energy are exponentially suppressed. When the temperature increases one approaches the point, at which the length  $L_T$  approaches the coherence length  $\xi$ . This is the Ginzburg temperature,  $T_{\text{Gi}}$ , determined as  $L_T(T = T_{\text{Gi}}) \sim \xi(T = T_{\text{Gi}})$ :

$$\rho_s(T_{\text{Gi}}) \xi(T_{\text{Gi}}) \sim \frac{T_c}{\kappa^2}. \quad (58)$$

or

$$\left( 1 - \frac{T_{\text{Gi}}}{T_c} \right) \sim \left( \frac{T_c}{\rho \xi_0 \kappa^2} \right)^2 \sim \left( \frac{T_c}{T_F} \right)^4. \quad (59)$$

Here as before  $T_F \sim \hbar^2/ma^2 \sim 1\text{ K}$  is the degeneracy temperature of the quantum fluid with  $a$  being an interatomic space. The critical fluctuations region – the Ginzburg region – is broad for  $^4\text{He}$ , where  $T_c \sim T_F$ , and is extremely small for  $^3\text{He}$ , where  $T_c < 10^{-2} T_F$ .

in the Ginzburg fluctuations region,  $T_{\text{Gi}} < T < T_c$ , the scaling exponents for the thermodynamic quantities, such as  $\xi$  and  $\rho_s$ , are different from that in the Ginzburg-Landau region,  $T_c - T_{\text{Gi}} < T_c - T \ll T_c$ :

$$\frac{\xi(T)}{\xi_0} \sim \left( 1 - \frac{T}{T_c} \right)^{-\frac{1}{2}}, \quad T_c - T_{\text{Gi}} < T_c - T \ll T_c, \quad (60)$$

$$\frac{\xi(T)}{\xi_0} \sim \left( 1 - \frac{T_{\text{Gi}}}{T_c} \right)^{\nu - \frac{1}{2}} \left( 1 - \frac{T}{T_c} \right)^{-\nu}, \quad T_{\text{Gi}} < T < T_c, \quad (61)$$

$$\frac{\rho_s(T)}{\rho} \sim \left( 1 - \frac{T}{T_c} \right), \quad T_c - T_{\text{Gi}} < T_c - T \ll T_c, \quad (62)$$

$$\frac{\rho_s(T)}{\rho} \sim \left( 1 - \frac{T_{\text{Gi}}}{T_c} \right)^{1-\zeta} \left( 1 - \frac{T}{T_c} \right)^{\zeta}, \quad T_{\text{Gi}} < T < T_c \quad (63)$$

There are two relations, the scaling hypothesis, which connect the critical exponents for  $\xi(T)$  and  $\rho_s(T)$  in the Ginzburg region, with the heat capacity exponent. In the Ginzburg region  $T_{\text{Gi}} < T < T_c$ , the coherence length is determined by thermal fluctuations, or which is the same, by thermal vortices. This gives the relation between the coherence length  $\xi(T)$  and superfluid density  $\rho_s(T)$  in the Ginzburg region:

$$\rho_s(T) \xi(T) \sim \frac{T_c}{\kappa^2} \sim \rho a \left( \frac{T_c}{T_F} \right), \quad T_{\text{Gi}} < T < T_c. \quad (64)$$

This Eq.(64) gives the Josephson scaling hypothesis:  $\nu = \zeta$ .

Another relation between these exponents comes from the consideration of the free energy, which has the same scaling law as the kinetic energy of superflow:

$$F(T) \sim \left(1 - \frac{T}{T_c}\right)^{2-\alpha} \sim \rho_s v_s^2 \sim \frac{\rho_s(T)}{\xi^2(T)} \sim \frac{\rho}{\xi_0^2} \left(1 - \frac{T}{T_c}\right)^{\zeta+2\nu} \quad (65)$$

Here  $\alpha$  is the critical exponent for the heat capacity in the critical region,  $C(T) = -T\partial_T^2 F \sim (1 - T/T_c)^{-\alpha}$ . The Eqs.(64) and (65) give  $\nu = \zeta = (2 - \alpha)/3$ .

### c. Nonequilibrium phase transition.

The formation of vortices during the quench is the subject of the dynamic scaling, which is the least known problem in the critical phenomena. The dynamical scaling is characterized by an additional set of the critical exponents, which depend not only on the symmetry and topology of the order parameter, but also on the interaction of the order parameter with different dynamical modes of the normal liquid. The problem first imposed by Zurek is what is the initial density  $\xi_v$  of macroscopic vortices at the moment when they become well defined. According to the general scaling hypothesis one has

$$\xi_v \sim \xi_0(\omega\tau_0)^{-\lambda}, \quad \omega = \frac{1}{\tau_Q}, \quad (66)$$

where  $\omega$  is the characteristic frequency of the dynamical process.

In the time-dependent Ginzburg-Landau model in Eq.(42) and also in the RG scheme based on this model, the exponent  $\lambda$  is determined by the static exponents and by the exponent for the relaxation time  $\tau = \tau_0(1 - T/T_c)^{-\mu}$ :

$$\lambda = \frac{\nu}{1 + \mu}, \quad (67)$$

This follows from the following consideration. When we approach the critical temperature from the normal phase, at some moment  $t_{\text{Zurek}}$  the relaxation time  $\tau(t)$  becomes comparable with the time  $t$  left till transition. At this moment

$$t_{\text{Zurek}} = \tau_0 \left( \frac{\tau_Q}{\tau_0} \right)^{\mu/(1+\mu)}, \quad (68)$$

the vortex network is frozen out. It becomes free again after the transition when  $\tau(t)$  again becomes smaller than  $t$ . The initial distance between the vortices is determined as the coherence length  $\xi = \xi_0(t/\tau_Q)^{-\nu}$  at  $t = t_{\text{Zurek}}$ , which gives the Eq.(66) with  $\lambda = \nu/(1 + \mu)$ . For the conventional time-dependent Ginzburg-Landau model in Eq.(42) one has  $\mu = 1$ ,  $\nu = 1/2$  and thus  $\lambda = 1/4$ . In the Ginzburg regime, if one assumes that  $\mu$  remains the same, while  $\nu \approx 2/3$ , one obtains  $\lambda \approx 1/3$ .

In numerical simulations of the quench in the time-dependent Ginzburg-Landau model, the main problem is to resolve between the microscopic vortices (zeroes)

and real macroscopic vortices. This requires some coarse-graining procedure, which is not well established. Moreover, there is a speculation [61] that if the quench occurs within the Ginzburg fluctuations region, the network of microscopic vortices can effectively screen the real macroscopic vortices, so that the density of the real vortices after quench is essentially less than the Zurek estimation. This can explain the negative result of the recent quench experiments in  $^4\text{He}$  [9], where the transition occurred well in the critical fluctuations region.

## 14. IMPLICATIONS OF THE QUENCH-COOL EXPERIMENTS

It is not entirely evident that a phenomenological model like the KZ mechanism, which is based on scaling arguments, should work at all: It describes a time-dependent phase transition in terms of quantities characterizing the equilibrium properties of the system. Numerical calculations have been performed on simple quantum systems, mostly in the 1-dimensional case, where one studies the fluctuations in the amplitude of the system wave function while it is quench cooled below a second order phase transition [46]. Such calculations have provided evidence for the KZ model and appear to agree with its qualitative features.

The experiment in rotating superfluid  $^3\text{He}$  is the first to test the KZ model quantitatively in a real physical environment which suffers from deficiencies like the presence of the superfluid boundary and a thermal gradient. Evidently the experiment and the model are in good harmony, assuming that all open questions from Sec. II-11 can be answered satisfactorily, as we believe at this point. However, the good agreement leaves us with a disturbing question: What is the microscopic basis for the applicability of the KZ mechanism to this experiment? A rapid quench through the superfluid phase transition is more amenable to microscopic analysis in the case of superfluid  $^3\text{He}$  than in most other systems. The freeze out of order-parameter domains can probably be demonstrated from the time-dependent Ginzburg-Landau equations with a sophisticated 2-dimensional calculation. The consequences from this would be exciting and the prospects for a better understanding of nonequilibrium phase transitions look promising.

Are there any implications from such work to cosmological large-scale structure formation? Measurements, described in this section, shows that topological defects are expected to form in rapid second order phase transitions, most likely therefore also in the cosmological settings. It is still unclear what form these phase transitions take, what kind of defects can be formed, what traces such defects, which may have annihilated long ago, would leave behind, and whether defect formation alone or perhaps in the presence of other phenomena, like inflationary expansion, are needed to explain large-scale structure formation.

### III. OTHER ANALOGUES IN QUANTUM FIELD THEORY RELATED TO VORTICES

At closer inspection, it has turned out that other connections can be worked out between the physics of the  $^3\text{He}$  superfluid phases and various ideas in relativistic quantum field theory. At best such analogue approaches have the benefit that the known and tested  $^3\text{He}$  features can perhaps open new ways of thought on how to solve problems in quantum field theory, on which no direct experimental information yet exists. An example is the concept of the energetic physical vacuum in elementary particle physics – the modern ether. Bosonic and fermionic excitations in  $^3\text{He}$  are in many respects similar to the excitations of the physical vacuum. This similarity allows us to model, with concepts borrowed from  $^3\text{He}$  physics, the interactions of elementary particles with the evolving strings and domain walls, which are formed in a rapid phase transition. These processes become important after defect formation in the initial quench and give rise to the cosmological consequences which we are measuring today.

#### 1. THE THREE TOPOLOGICAL FORCES ACTING ON A VORTEX AND THEIR ANALOGUES

Here we consider several effects coming from these interactions, which result in the experimentally observed forces acting on the vortex moving in  $^3\text{He}$ . As we mentioned in Sec. II-11c, there are 3 different topological contributions to the force acting on the vortex. The more familiar Magnus force arises when the vortex moves with respect to the superfluid vacuum. For the relativistic cosmic string such force is absent since the corresponding superfluid density of the quantum physical vacuum is zero. However the analog of this force appears if the cosmic string moves in the uniform background charge density [86,87]. The other two forces of topological origin — the Iordanskii force and spectral flow force — also have analogs for the cosmic strings [88–91], which we discuss here.

First we start with the Iordanskii force [92,93], which arises when the vortex moves with respect to the heat bath represented by the normal component of the liquid, which consists of the quasiparticle excitations. The latter corresponds to the matter in particle physics. The interaction of quasiparticles with the velocity field of the vortex resembles the interaction of the matter with the gravitational field induced by such cosmic string, which has an angular momentum, – the so-called spinning cosmic string [94]. The spinning string induces the peculiar space-time metric, which leads to the difference of times needed for any particle to orbit around the string with the same speed, but in opposite directions [95]. This gives rise to the quantum gravitational Aharonov-Bohm effect

[94,96,97]. In this section we discuss how the same effect leads to the asymmetry in the scattering of particles on the spinning string and finally to the Iordanskii lifting force acting on the spinning string or on the moving vortex in superfluid.

The other force, arising when the vortex moves with respect to the heat bath, is the direct consequence of the chiral anomaly effect, which violates the conservation of the fermionic charge. The anomalous generation by the moving vortex of such fermionic charge as momentum (called “momentogenesis”) leads to the net force acting on the vortex, which was experimentally confirmed in  $^3\text{He}$  [62]. This phenomenon is based on the same physics as the anomalous generation of matter in particle physics and bears directly on the cosmological problem of the baryonic asymmetry of our present Universe: why the Universe contains much more matter than antimatter (“baryogenesis”).

The experimental observation of the opposite effect to momentogenesis has been reported in [76]: the conversion of quasiparticle momentum into a non-trivial order parameter configuration or “texture”. The corresponding process in a cosmological setting would be the creation of a primordial magnetic field due to changes in the matter content. Processes in which magnetic fields are generated are very relevant to cosmology as magnetic fields are ubiquitous now in the Universe. The Milky Way, other galaxies, and clusters of galaxies are observed to have a magnetic field whose generation is still not understood. One possible mechanism is that a seed field was amplified by the complex motions associated with galaxies and clusters of galaxies. The seed field itself is usually assumed to be of cosmological origin.

It has been noted that the two genesis problems in cosmology – baryo- and magnetogenesis – may be related to each other [67,69,70]. More recently, a stronger possible connection has been detailed [73,74]. In the same way they are related in  $^3\text{He}$ , where the texture is the analog of magnetic field while the normal component of the liquid represents the matter: the moving vortex texture leads to the anomalous production of quasiparticles, while an excess of the quasiparticle momentum – the net quasiparticle current of the normal component – leads to the formation of textures. This mapping of cosmology to condensed matter is not simply a picture: the corresponding effects in the two systems are described by the same equations in the low-energy regime, by quantum field theory and the axial anomaly.

#### 2. IORDANSKII FORCE

##### *a. Superfluid vortex vs spinning cosmic string*

To clarify the analogy between the Iordanskii force and AB effect, let us consider the simplest case of phonons propagating in the velocity field of the quantized vortex

in the Bose superfluid  $^4\text{He}$ . According to the Landau theory of superfluidity, the energy of quasiparticle moving in the superfluid velocity field  $\mathbf{v}_s(\mathbf{r})$  is Doppler shifted:  $E(\mathbf{p}) = \epsilon(\mathbf{p}) + \mathbf{p} \cdot \mathbf{v}_s(\mathbf{r})$ . In the case of the phonons with the spectrum  $\epsilon(\mathbf{p}) = cp$ , where  $c$  is the sound velocity, the energy-momentum relation is thus

$$(E - \mathbf{p} \cdot \mathbf{v}_s(\mathbf{r}))^2 = c^2 p^2. \quad (69)$$

The Eq.(69) can be written in the general Lorentzian form with  $p_\mu = (E, \mathbf{p})$ :

$$g^{\mu\nu} p_\mu p_\nu = 0 \quad (70)$$

where the metric is

$$g^{00} = 1, \quad g^{0i} = -v_s^i, \quad g^{ik} = -c^2 \delta^{ik} + v_s^i v_s^k. \quad (71)$$

We use the convention to denote indices in the 0–3 range by greek letters and indices in the 1–3 range by latin letters. Thus the dynamics of phonons in the presence of the velocity field is the same as the dynamics of photons in the gravity field [98]: both are described by the light-cone equation  $ds = 0$ . The interval  $ds$  for phonons is given by the inverse metric  $g_{\mu\nu}$  which determines the geometry of the effective space:

$$ds^2 = g_{\mu\nu} dx^\mu dx^\nu, \quad (72)$$

where  $x = (t, \mathbf{r})$  are physical (Galilean) coordinates in the laboratory frame.

The similar relativistic equation occurs for the fermionic quasiparticles in the superfluid  $^3\text{He-A}$  in the linear approximation close to the gap nodes. In general, i.e. far from the gap nodes, the spectrum of quasiparticle in  $^3\text{He-A}$  is not relativistic:

$$\epsilon^2(\mathbf{p}) = v_F^2(p - p_F)^2 + \frac{\Delta_A^2}{p_F^2}(\hat{\mathbf{l}} \times \mathbf{p}). \quad (73)$$

Here  $v_F(p - p_F)$  is the quasiparticle energy in the normal Fermi liquid above transition, with  $p_F$  the Fermi momentum and  $v_F = p_F/m^*$ ;  $m^*$  is the effective mass, which is of order the mass  $m_3$  of the  $^3\text{He}$  atom;  $\Delta_A$  is the so-called gap amplitude and the unit vector  $\hat{\mathbf{l}}$  shows direction to the gap nodes.

The energy in Eq. (73) is zero at two points  $\mathbf{p} = e\mathbf{A}$  with  $\mathbf{A} = p_F\hat{\mathbf{l}}$  and  $e = \pm 1$ . Close to the two zeroes of the energy spectrum one can expand equation  $(E - \mathbf{p} \cdot \mathbf{v}_s(\mathbf{r}))^2 = \epsilon^2(\mathbf{p})$  in  $\mathbf{p} - e\mathbf{A}$  and bring it to the form similar to the propagation equation for a massless relativistic particle in a curved spacetime in the presence of an electromagnetic vector potential:

$$g^{\mu\nu}(p_\mu - eA_\mu)(p_\nu - eA_\nu) = 0. \quad (74)$$

Here  $A_0 = p_F(\hat{\mathbf{l}} \cdot \mathbf{A})$  and the metric is anisotropic with the anisotropy axis along the  $\hat{\mathbf{l}}$ -vector:

$$\begin{aligned} g^{00} &= 1, \quad g^{0i} = -v_s^i, \\ g^{ik} &= -c_\perp^2(\delta^{ik} - \hat{l}^i \hat{l}^k) - c_\parallel^2 \hat{l}^i \hat{l}^k + v_s^i v_s^k, \\ c_\parallel &= v_F, \quad c_\perp = \Delta_A/v_F. \end{aligned} \quad (75)$$

Here the quantities  $c_\parallel$  and  $c_\perp$  play the part of speeds of light propagating along  $\hat{\mathbf{l}}$  and in transverse directions correspondingly.

For simplicity, let us turn back to the case of phonons and vortices in  $^4\text{He}$  which is described by Eqs. (70), (71). If velocity field is induced by one vortex with  $\nu$  quanta of circulation,  $\mathbf{v}_s = \nu\kappa\hat{\phi}/2\pi r$ , then the interval (72) in the effective space, where the phonon is propagating along geodesic curves, becomes:

$$ds^2 = \left(1 - \frac{v_s^2}{c^2}\right) \left(dt + \frac{\nu\kappa d\phi}{2\pi(c^2 - v_s^2)}\right)^2 - \frac{dr^2}{c^2} - \frac{dz^2}{c^2} - \frac{r^2 d\phi^2}{c^2 - v_s^2}. \quad (76)$$

The origin of the Iordanskii force lies in the scattering of quasiparticles for small angles, so large distances from the vortex core are important. Far from the vortex  $v_s^2/c^2$  is small and can be neglected, and one has

$$ds^2 = \left(dt + \frac{d\phi}{\omega}\right)^2 - \frac{1}{c^2}(dz^2 + dr^2 + r^2 d\phi^2), \quad \omega = \frac{2\pi c^2}{\nu\kappa} \quad (77)$$

The connection between the time and the azimuthal angle  $\phi$  in the interval suggests that there is a characteristic angular velocity  $\omega$ . The similar metric with rotation was obtained for the so-called spinning cosmic string in 3 + 1 space-time, which has the rotational angular momentum  $J$  concentrated in the string core, and for the spinning particle in the 2+1 gravity [94,97,99,100]:

$$ds^2 = \left(dt + \frac{d\phi}{\omega}\right)^2 - \frac{1}{c^2}(dz^2 + dr^2 + r^2 d\phi^2), \quad \omega = \frac{1}{4JG} \quad (78)$$

where  $G$  is the gravitational constant. This gives the following correspondence between the circulation  $\nu\kappa$  around the vortex and the angular momentum  $J$  of the spinning string

$$\kappa\nu = 8\pi JG. \quad (79)$$

Though we consider the analogy between the spinning string and vortices in superfluid  $^4\text{He}$ , there is a general statement that vortices in any superfluids have the properties of the spinning cosmic strings [86]. In particular, the spinning string generates the density of the angular momentum in the vacuum outside the string [101]. The density of the angular momentum in the superfluid vacuum outside the vortex is also nonzero and equals at  $T = 0$

$$\mathbf{r} \times \rho \mathbf{v}_s = \hbar \nu n_B \hat{\mathbf{z}}, \quad (80)$$

where  $n_B$  is the density of elementary bosons in superfluid vacuum: the density  $\rho/m_4$  of  $^4\text{He}$  atom in superfluid  $^4\text{He}$  or the density  $\rho/2m_3$  of Cooper pairs in superfluid  $^3\text{He}$ .

### b. Gravitational Aharonov-Bohm effect

The effect peculiar for the spinning string, which can be modeled in condensed matter, is the gravitational AB topological effect [94]. On the classical level the propagation of the particles is described by the relativistic equation  $ds^2 = 0$ . Outside the string the space metric, which enters the interval  $ds$ , is flat, Eq. (78). But there is the difference in the travel time for the particles propagating around the spinning string along the closed path in the opposite directions. As can be seen from (78) this time difference is [95]

$$2\tau = \frac{4\pi}{\omega}. \quad (81)$$

For the vortex at large distances from the core the same equation approximately valid due to equivalence of metrics Eqs. (77) and (78). This asymmetry between the particles orbiting in different directions around vortex implies that in addition to the symmetric part of the cross section:

$$\sigma_{\parallel} = \int_0^{2\pi} d\theta (1 - \cos \theta) |a(\theta)|^2, \quad (82)$$

where  $a(\theta)$  is a scattering amplitude, there should be an asymmetric part of the scattering cross section:

$$\sigma_{\perp} = \int_0^{2\pi} d\theta \sin \theta |a(\theta)|^2. \quad (83)$$

The latter is the origin of the Iordanskii force acting on the vortex in the presence of the net momentum of the quasiparticles. Another consequence of the Eqs. (77,78) is displayed on the quantum level: the connection between the time variable  $t$  and the angle variable  $\phi$  in the Eqs. (77), (78) implies that the scattering cross sections of phonons (photons) on the vortex (string) should be the periodic functions of the energy with the period equal to  $\hbar\omega$ .

Calculations which allow to find both symmetric and asymmetric contributions to the scattering of the quasiparticles on the velocity field of the vortex have been done by Sonin for phonons and rotons in  $^4\text{He}$  [89] and by Cleary [105] for the Bogoliubov-Nambu quasiparticles in conventional superconductors. In the case of phonons the propagation is described by the Lorentzian equation for the scalar field  $\Phi$ ,  $g^{\mu\nu} \partial_\mu \partial_\nu \Phi = 0$  with  $g^{\mu\nu}$  from Eq. (71). We are interested in large distances from the vortex core, so the quadratic terms  $\mathbf{v}_s^2/c^2$  can be neglected and this equation can be rewritten as [89]

$$E^2 \Phi - c^2 \left( -i\nabla + \frac{E}{c} \mathbf{v}_s(\mathbf{r}) \right)^2 \Phi = 0. \quad (84)$$

This equation maps the problem under discussion to the Aharonov-Bohm (AB) problem for the magnetic flux tube [106] with the effective vector potential  $\mathbf{A} = \mathbf{v}_s$ , where the electric charge  $e$  is substituted by the mass  $E/c^2$  of the particle [96,101,107]. Because of the mapping between the electric charge and the mass of the particle, one obtains the AB expression [106] for the symmetric differential cross section

$$\frac{d\sigma_{\parallel}}{d\theta} = \frac{\hbar c}{2\pi E \sin^2(\theta/2)} \sin^2 \frac{\pi E}{\hbar\omega}. \quad (85)$$

This expression was obtained for the scattering of particles with energy  $E$  in the background of spinning string with zero mass [96,97] and represented the gravitational Aharonov-Bohm effect. Note the singularity at  $\theta \rightarrow 0$ .

Returning back to vortices one finds that the analogue with the spinning string is not exact. In more accurate calculations one should take into account that as distinct from the charged particles in the AB effect, the current in the case of phonons is not gauge invariant. As a result the scattering of the phonon with momentum  $p$  and with the energy  $E$  by the vortex is somewhat different [89]:

$$\frac{d\sigma_{\parallel}}{d\theta} = \frac{\hbar c}{2\pi E} \cot^2 \frac{\theta}{2} \sin^2 \frac{\pi E}{\hbar\omega}. \quad (86)$$

The algebraic difference between the AB result Eq. (85) and Eq. (86) is  $(\hbar c/2\pi E) \sin^2(\pi E/\omega)$ , which is independent of the scattering angle  $\theta$  and thus is not important for the singularity at small scattering angles, which is present in (86) as well. For small  $E$  the result in Eq. (86) was obtained by Fetter [108]. The generalization of the Fetter result for the quasiparticles with arbitrary spectrum  $\epsilon(\mathbf{p})$  (rotons in  $^4\text{He}$  and the Bogoliubov-Nambu fermions in superconductors) was recently suggested in Ref. [109]: In our notations it is  $(\nu \kappa^2 p / 8\pi v_G^2) \cot^2(\theta/2)$ , where  $v_G = d\epsilon/dp$  is the group velocity of quasiparticle.

### c. Asymmetric cross section of scattering on a vortex

The Lorentz force, which acts on the flux tube in the presence of electric current, has its counterpart – the Iordanskii force, which acts on the vortex in the presence of the mass current carried by the normal component. The Lorentz-type Iordanskii force comes from the asymmetric contribution to the cross section [89,91], which has the same origin as singularity at the small angles in the symmetric cross section and leads to the non-zero transverse cross section.

For the phonons in the  $^4\text{He}$  with the spectrum  $E(\mathbf{p}) = cp$  the transverse cross section is [89]

$$\sigma_{\perp} = \frac{\hbar}{p} \sin \frac{2\pi E}{\hbar\omega} \quad (87)$$



At low  $E \ll \hbar\omega$  the result becomes classical:  $\sigma_{\perp} = 2\pi c/\omega$  does not contain the Planck constant  $\hbar$ . This means that in the low energy limit the asymmetric cross section can be obtained from the classical theory of scattering. In this was it can be generalized for arbitrary spectrum  $E(\mathbf{p})$  of scattering particles [89]. Let us consider the particle with the spectrum  $E(\mathbf{p})$  moving in the background of the velocity field  $\mathbf{v}_s(\mathbf{r})$  around the vortex. The velocity field modifies the particle energy due to the Doppler shift,  $E(\mathbf{p}, \mathbf{r}) = E(\mathbf{p}) + \mathbf{p} \cdot \mathbf{v}_s(\mathbf{r})$ . Far from the vortex, where the circulating velocity is small, the trajectory of the quasiparticle is almost the straight line parallel, say, to the axis  $y$ , with the distance from the vortex line being the impact parameter  $x$ . It moves along this line with the almost constant momentum  $p_y \approx p$  and almost constant group velocity  $dy/dt = v_G = d\epsilon/dp$ . The change in the transverse momentum during this motion is determined by the Hamiltonian equation  $dp_x/dt = -\partial E/\partial x = -p_y \partial v_{sy}/\partial x$ , or  $dp_x/dy = -(p/v_G) \partial v_{sy}/\partial x$ . The transverse cross section is obtained by integration of  $\Delta p_x/p$  over the impact parameter  $x$ :

$$\sigma_{\perp} = \int_{-\infty}^{+\infty} \frac{dx}{v_G} \int_{-\infty}^{+\infty} dy \frac{\partial v_{sy}}{\partial x} = \frac{\nu\kappa}{v_G}. \quad (88)$$

This result is a pure classical: the Planck constant  $\hbar$  drops out (it enters only the circulating quantum which characterizes the vortex).

#### d. Iordanskii force: vortex and spinning string

The asymmetric part of scattering, which describes the momentum transfer in the transverse direction, after integration over the distribution of excitations gives rise to the transverse force acting on the vortex if the vortex moves with respect to the normal component. This is the Iordanskii force:

$$\begin{aligned} \mathbf{f}_{\text{Iordanskii}} &= \int \frac{d^3p}{(2\pi)^3} \sigma_{\perp}(p) v_G n(\mathbf{p}) \mathbf{p} \times \hat{\mathbf{z}} = \\ &= -\nu\kappa \hat{\mathbf{z}} \times \int \frac{d^3p}{(2\pi)^3} n(\mathbf{p}) \mathbf{p} = \nu\kappa \mathbf{P}_n \times \hat{\mathbf{z}} \end{aligned} \quad (89)$$

It is proportional to the density of mass current  $\mathbf{P}_n$  carried by excitations (matter). Of the vortex parameters it depends only on the circulation  $\nu\kappa$ . This confirms the topological origin of this force. In the case of the equilibrium distribution of quasiparticles one has  $\mathbf{P}_n = \rho_n \mathbf{v}_n$ , where  $\rho_n$  and  $\mathbf{v}_n$  are the density and velocity of the normal component of the liquid. So one obtains the Eq. (32). To avoid the conventional Magnus force in this derivation, we assumed that the asymptotic velocity of the superfluid component of the liquid is zero in the vortex frame.

The Eq. (89) was obtained using the asymptotic behavior of the flow field  $\mathbf{v}_s$ , which induces the same effective metric (77) as the metric around the spinning string

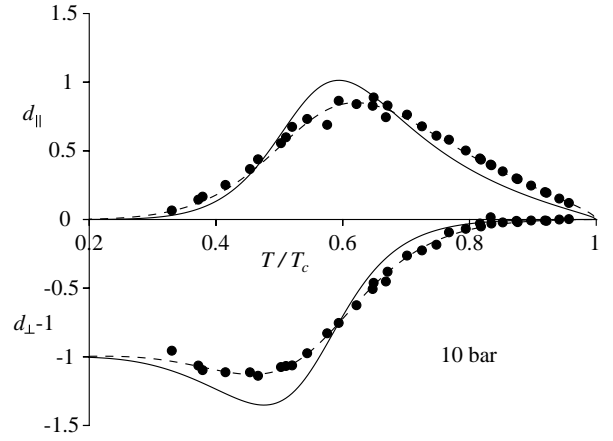


FIG. 21.  $d_{\parallel, \perp}$  as a function of temperature in  $^3\text{He-B}$  at 10 bar. Negative sign of  $d_{\perp}$  at  $T/T_c \approx 0.4-0.5$  constitutes experimental verification for the existence of Iordanskii force. From Ref. [63].

(78). So one can apply this result directly to the spinning string. The asymmetric cross-section of the scattering of relativistic particles on the spinning string is given by Eq. (87). This means that in the presence of the momentum of matter the spinning cosmic string experiences the kind of the lifting force, which corresponds to the Iordanskii force in superfluids. This force can be obtained by relativistic generalization of the Eq. (89). The momentum density  $\mathbf{P}_n$  of quasiparticles should be substituted by the component  $T_0^i$  of the energy-momentum tensor. As a result, for 2+1 space-time and for small energy  $E$ , which corresponds to the low temperature  $T$  of the matter, the Iordanskii force on spinning string moving with respect to the matter is

$$f_{\text{Iordanskii}}^{\alpha} = 8\pi J G e^{\alpha\beta\gamma} u_{\beta} u_{\mu} T_{\gamma}^{\mu}. \quad (90)$$

Here  $u_{\alpha}$  is the 3-velocity of the string and  $T_{\gamma}^{\mu}$  is the asymptotic value of the energy-momentum tensor of the matter at the spot of the string. Using the Einstein equations one can rewrite this as

$$f_{\text{Iordanskii}}^{\alpha} = J e^{\alpha\beta\gamma} u_{\beta} u_{\mu} R_{\gamma}^{\mu}, \quad (91)$$

where  $R_{\gamma}^{\mu}$  is the Riemannian curvature at the position of the string. This corresponds to the force acting on particle with the spin  $J$  from the gravitational field due to interaction of the spin with the Riemann tensor [110].

Note that previously we have shown how ideas first developed in cosmological context (such as nucleation of bubbles of different broken symmetry phases during rapid transition) could be applied to the superfluid helium. Here we have the opposite case: when the ideas originated from helium physics have application in the other systems described by the quantum field theory.

Iordanskii force has been experimentally identified in the rotating superfluid  $^3\text{He-B}$  [63]. In Eq. (38) which describes temperature dependence of  $d_{\perp}$  the term  $m_3\mathcal{C}(T)$

is due to spectral flow force which is discussed in Sec. III-3c and equals to zero at low temperatures. So at low temperatures  $d_{\perp} \approx -\rho_n/\rho$  [111], where  $\rho$  is the total density of the liquid. Negative value of  $d_{\perp}$  is solely due to the existence of the Iordanskii force. This is in accordance with the experimental data, which show that  $d_{\perp}$  does have negative value at low  $T$ , see Fig. 21. At higher  $T$  the spectral flow force becomes dominating leading to the sign reversal of  $d_{\perp}$ . Due to analogy between string and vortices outlined in this section this presents experimental verification of the analog of the gravitational Aharonov-Bohm effect on spinning cosmic string.

### 3. SPECTRAL FLOW FORCE AND CHIRAL ANOMALY

#### a. Chiral anomaly

In the standard model of electroweak interaction there are certain quantities, like the baryon number  $Q_B$ , which are classically conserved but can be violated by quantum mechanical effects known generically as “chiral anomalies”. (Each of the quarks is assigned  $Q_B = 1/3$  while the leptons (neutrino and electron) have  $Q_B = 0$ .) The process leading to particle creation is called “spectral flow”, and can be pictured as a process in which fermions flow under an external perturbation from negative energy levels towards positive energy levels. Some fermions therefore cross zero energy and move from the Dirac sea into the observable positive energy world.

The origin for the axial anomaly can be seen from the behavior of the chiral particle in a constant magnetic field,  $\mathbf{A} = (1/2)\mathbf{B} \times \mathbf{r}$ . Chiral particle we call a particle without mass but with spin  $\vec{\sigma} [=1/2]$ . Such particle could be classified to right and left according to whether its spin is parallel or antiparallel to its momentum. The Hamiltonians for the right particle with the electric charge  $e_R$  and for the left particle with the electric charge  $e_L$  are

$$\mathcal{H} = c\vec{\sigma} \cdot (\mathbf{p} - e_R\mathbf{A}), \quad \mathcal{H} = -c\vec{\sigma} \cdot (\mathbf{p} - e_L\mathbf{A}). \quad (92)$$

As usual, motion of the particles in the plane perpendicular to  $\mathbf{B} \parallel \hat{z}$  is quantized into the Landau levels and the free motion is thus effectively reduced to one-dimensional motion along  $\mathbf{B}$  with momentum  $p_z$ . Fig. 22 shows the energy spectrum; the thick lines show the occupied negative-energy states. The peculiar feature of the spectrum is that because of the chirality of the particles the lowest ( $n = 0$ ) Landau level is asymmetric. It crosses zero only in one direction:  $E = cp_z$  for the right particle and  $E = -cp_z$  for the left one. If we now apply an electric field  $\mathbf{E}$  along  $z$ , particles are pushed from negative to positive energy levels according to the equation of motion  $\dot{p}_z = e_R E_z$  ( $\dot{p}_z = e_L E_z$ ) and the whole Dirac sea moves up (down) creating particles and electric charge from the vacuum. This motion of particles along the “anomalous” branch of the spectrum is called *spectral flow*. The rate

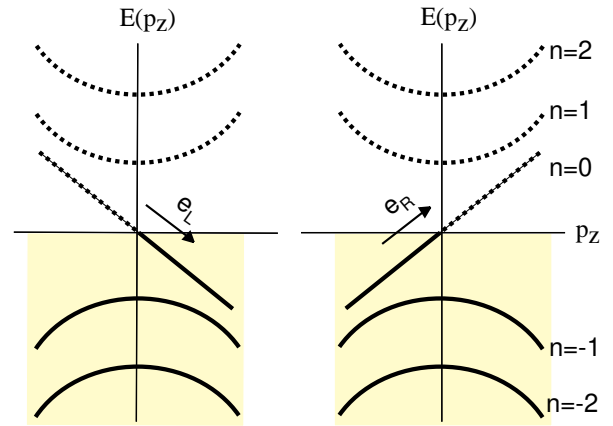


FIG. 22. The energy spectrum of a chiral particle in constant magnetic fields along  $\hat{z}$  (Landau levels). Plots on the left and the right show spectra for left and right particle respectively.

of particle production is proportional to the density of states at the Landau level, which is

$$N_R(0) = \frac{|e_R \mathbf{B}|}{4\pi^2}, \quad N_L(0) = \frac{|e_L \mathbf{B}|}{4\pi^2} \quad (93)$$

The rate of production of particle number  $n = n_R + n_L$  and of charge  $Q = n_R e_R + n_L e_L$  from the vacuum is

$$\dot{n} = \frac{1}{4\pi^2}(e_R^2 - e_L^2)\mathbf{E} \cdot \mathbf{B}, \quad \dot{Q} = \frac{1}{4\pi^2}(e_R^3 - e_L^3)\mathbf{E} \cdot \mathbf{B}. \quad (94)$$

This is an anomaly equation for the production of particles from vacuum of the type found by Adler [77] and by Bell and Jackiw [78] in the context of neutral pion decay. We see that for particle or charge creation without creation of corresponding antiparticles it is necessary to have an asymmetric branch of the dispersion relation  $E(p)$  which crosses the axis from negative to positive energy. Additionally, the symmetry between the left and right particles has to be violated:  $e_R \neq e_L$  for the charge creation and  $e_R^2 \neq e_L^2$  for the particle creation.

In the electroweak model there are two gauge fields whose “electric” and “magnetic” fields may become a source for baryonproduction: The hypercharge field  $U(1)$  and the weak field  $SU(2)$ . Anomalous zero mode branches exist in the core of a Z-string, where quarks, electrons and neutrinos are all chiral particles with known hypercharge and weak charges. If we consider a process in which one electron, two  $u$ -quarks and one  $d$ -quark are created, then lepton and baryon numbers are changed by unity while electric charge is conserved [62]. If we sum appropriate charges for all particles according to Eq. (94) the rate of this process is

$$\dot{n}_{\text{bar}} = \dot{n}_{\text{lept}} = \frac{N_F}{8\pi^2} (-\mathbf{B}_W^a \cdot \mathbf{E}_{aW} + \mathbf{B}_Y \cdot \mathbf{E}_Y) \quad (95)$$

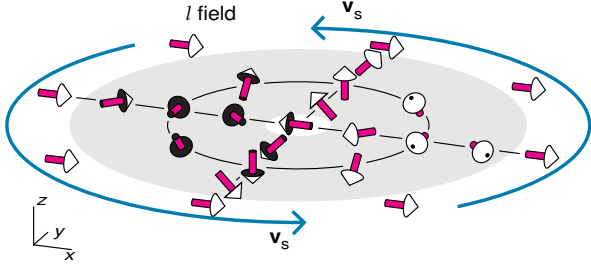


FIG. 23. The order parameter  $\hat{\mathbf{l}}$ -texture in the soft core of the continuous Anderson-Toulouse-Chechetkin vortex.

where  $N_F = 3$  is the number of families (generations) of fermions,  $\mathbf{B}_W^a$  and  $\mathbf{E}_{aW}$  are the colored  $SU(2)$  magnetic and electric fields, while  $\mathbf{B}_Y$  and  $\mathbf{E}_Y$  are the magnetic and electric fields of the  $U(1)$  hypercharge. While a color and hypercharge magnetic flux is always present in the Z-string core, a color and hypercharge electric field can also be present along the string if the string is moving across a background electromagnetic field [66] or in certain other processes such as the decoupling of two linked loops [67,68]. Thus parallel electric and magnetic fields in the string change the baryonic charge and can lead to cosmological baryogenesis [71] and to the presence of antimatter in cosmic rays [72].

In superconductors and in superfluid  $^3\text{He}$  an anomalous zero mode branch exists for fermions in the core of quantized vortices. For electrons in superconductors it was found first in Ref. [79], and for vortices in superfluid  $^3\text{He}$  in Ref. [82]. One of the physically important fermionic charges in  $^3\text{He-A}$ ,  $^3\text{He-B}$  and superconductors which, like baryonic charge in the standard model, is not conserved due to the anomaly, is linear momentum. The spectral flow of momentum along the zero mode branch leads to an additional “lift” force which acts on a moving vortex.

The analogy is clearest for the continuous vortex in  $^3\text{He-A}$ , which has two quanta of the superfluid circulation,  $\nu = 2$ . This vortex is similar to the continuous Z-vortex in electroweak theory: it is characterized by a continuous distribution of the order parameter vector  $\hat{\mathbf{l}}$ , the direction of the angular momentum of the Cooper pairs (Fig. 23). When multiplied by the Fermi wavenumber  $k_F = p_F/\hbar$ , this vector acts like an effective “electromagnetic” vector potential  $\mathbf{A} = k_F \hat{\mathbf{l}}$  on the quasiparticles. The quasiparticles in  $^3\text{He-A}$  are chiral: they are either left- or right-handed [84]. As follows from BCS theory of  $^3\text{He-A}$  the sign of the “electric” charge  $e$ , introduced in Sec. III-2a, simultaneously determines the chirality of the fermions. This is clearly seen with a simple isotropic example having  $c_{\parallel} = c_{\perp} = c$ :

$$\mathcal{H} = -ec\vec{\sigma} \cdot (\mathbf{p} - e\mathbf{A}) . \quad (96)$$

A particle with positive (negative)  $e$  at the north (south) pole is left-handed (right-handed). Here  $\vec{\sigma}$  is a Bogolubov spin.

For such gapless chiral fermions the Adler-Bell-Jackiw anomaly applies and the momentum (“chiral charge”) of quasiparticles is not conserved in the presence of “electric” and “magnetic” fields, which are defined by

$$\mathbf{E} = k_F \partial_t \hat{\mathbf{l}}, \quad \mathbf{B} = k_F \nabla \times \hat{\mathbf{l}}. \quad (97)$$

In  $^3\text{He-A}$  each right-handed quasiparticle carries the momentum  $\mathbf{p}_R = p_F \hat{\mathbf{l}}$  (we reverse sign of momentum when using it as a fermionic charge), and left-handed quasiparticle has  $\mathbf{p}_L = -\mathbf{p}_R$ . According to Eq. (94) production rates for right and left handed quasiparticles are (since  $e_R^2 = e_L^2 = 1$  in this case)

$$\dot{n}_R = -\dot{n}_L = \frac{1}{4\pi} \mathbf{E} \cdot \mathbf{B}. \quad (98)$$

As a result there is a net creation of quasiparticle momentum  $\mathbf{P}$  in a time-dependent texture:

$$\partial_t \mathbf{P} = \int d^3r (\mathbf{p}_R \dot{n}_R + \mathbf{p}_L \dot{n}_L) = \frac{1}{2\pi^2} \int d^3r p_F \hat{\mathbf{l}} (\mathbf{E} \cdot \mathbf{B}) . \quad (99)$$

What we know for sure is that the total linear momentum is conserved. Then Eq. (99) means that, in the presence of the time-dependent texture, the momentum is transferred from the superfluid motion of the *vacuum* to *matter* (the heat bath of quasiparticles forming the normal component).

#### b. Anomalous force acting on a continuous vortex and baryogenesis from textures

Let us consider this on the example of the simplest continuous-core vortex in superfluid  $^3\text{He-A}$  (Fig. 23). It has the following distribution of the unit vector  $\hat{\mathbf{l}}(\mathbf{r})$  which shows the direction of the pont gap nodes in the smooth core

$$\hat{\mathbf{l}}(\mathbf{r}) = \hat{\mathbf{z}} \cos \eta(r) + \hat{\mathbf{r}} \sin \eta(r) , \quad (100)$$

where  $z, r, \phi$  are cylindrical coordinates. The  $\hat{\mathbf{l}}$ -vector in the smooth core changes from  $\hat{\mathbf{l}}(0) = -\hat{\mathbf{z}}$  to  $\hat{\mathbf{l}}(\infty) = \hat{\mathbf{z}}$ . The circulation of the superfluid velocity along the path far outside the soft core corresponds to  $\nu = 2$ , i.e. this  $\hat{\mathbf{l}}$  texture represents the doubly quantized continuous vortex.

When such a continuous vortex as in moves in  $^3\text{He-A}$  with velocity  $\mathbf{v}_L$  it generates time dependent  $\hat{\mathbf{l}}$  texture  $\hat{\mathbf{l}} = \hat{\mathbf{l}}(\mathbf{r} - \mathbf{v}_L t)$ . Hence both an “electric” and a “magnetic” field from Eq. (97) exist and this leads to “momentogenesis”. Integration of the anomalous momentum transfer in Eq.(99) over the cross-section of the soft core of the moving vortex gives thus the additional force acting on the vortex due to spectral flow:

$$\mathbf{f}_{\text{sf}} = \partial_t \mathbf{P} = \pi \hbar \nu C_0 \hat{\mathbf{z}} \times (\mathbf{v}_n - \mathbf{v}_L) . \quad (101)$$

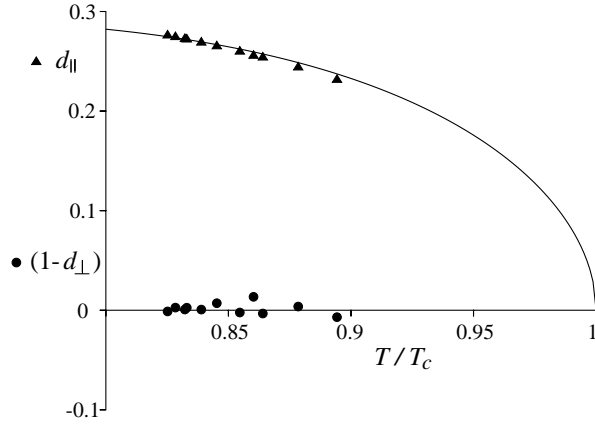


FIG. 24.  $d_{\parallel}$  and  $(1 - d_{\perp})$  in the  $^3\text{He-A}$  at 29.3 bar. From Ref. [63].

Here  $\hat{\mathbf{z}}$  is the direction of the vortex,  $\mathcal{C}_0 = k_F^3/3\pi^2$ , and  $\mathbf{v}_n$  is the heat bath velocity. Thus we obtained the Eq. (33) with the temperature independent parameter  $\mathcal{C}(T) = \mathcal{C}_0$ .

Measurements of the mutual friction coefficients in  $^3\text{He-A}$  [63] provide experimental verification for the spectral flow force. According to Eq. (38) in the A phase it should be  $d_{\perp} = (m_3\mathcal{C}_0 - \rho_n)/\rho_s$ . Value of  $m_3\mathcal{C}_0$  is the total mass density  $\rho$  in the normal phase. Its difference from  $\rho$  in superfluid phase is thus determined by the tiny effect of superfluidity on the particle density and is extremely small:  $\rho - m_3\mathcal{C}_0 \sim \rho(\Delta_0/v_F p_F)^2 = \rho(c_{\perp}/c_{\parallel})^2 \ll \rho$ . Thus one must have  $d_{\perp} \approx 1$  for all practical temperatures. The  $^3\text{He-A}$  experiments made at 29.3bar and  $T > 0.82T_c$  are consistent with this within experimental uncertainty: it was found that  $|1 - d_{\perp}| < 0.005$  as demonstrated in Fig. 24.

### c. Anomalous force acting on a singular vortex and baryogenesis with strings

The discussion of the spectral flow in the previous sections and particularly Eq. (94) can not be directly applied to the singular vortices which are found in the  $^3\text{He-B}$  and superconductors. The reason for this is that the deviation of the magnitude of the order parameter from equilibrium value in the core of such vortices create a potential well for the core quasiparticles. In this well quasiparticles have discrete energy levels with some character separation  $\hbar\omega_0$  instead of continuous (by  $p_z$ ) spectra as have been considered above. Thus the theory of spectral flow becomes more complicated but can be constructed [81].

The basic idea is that discrete levels have some broadening  $\hbar/\tau$  resulting from the scattering of core excitations by free excitations in the heat bath outside the core (or by impurities in superconductors). At low temperatures when the width of levels is much less than their separation, i.e.  $\omega_0\tau \gg 1$ , the spectral flow is essentially suppressed,  $\mathcal{C}(T) = 0$ . In the opposite case of  $\omega_0\tau \ll 1$  the

levels overlap and we have situation similar to the spectral flow with continuous spectra:  $\mathcal{C}(T) \approx \mathcal{C}_0$ . We may construct interpolation formula between these two cases:

$$\mathcal{C}(T) \sim \frac{\mathcal{C}_0}{1 + \omega_0^2\tau^2}. \quad (102)$$

In fact, both  $d_{\parallel}$  and  $d_{\perp}$  mutual friction coefficients are affected by this renormalization of the spectral flow force [81,83]:

$$d_{\parallel} - i(1 - d_{\perp}) = \frac{\rho}{\rho_s} \frac{\omega_0\tau}{1 + i\omega_0\tau} \tanh \frac{\Delta(T)}{2k_B T}. \quad (103)$$

Let us derive this equation using the Landau-type phenomenological description for the fermions in the vortex core developed by Stone [83]. For simplicity we consider the axisymmetric vortex core, the general case of the asymmetric core is discussed in [119]. The low-energy spectrum of Caroli-de-Gennes-Matricon quasiparticles around a vortex contains an anomalous branch of fermionic zero modes. For the axisymmetric vortex excitations on this branch are characterized by the angular momentum  $L_z$

$$E(L_z, p_z) = -\omega_0(p_z)L_z. \quad (104)$$

For superconductors with the coherence length  $\xi$  much larger than the inverse Fermi momentum,  $p_F\xi \gg 1$ , the electron wavelength is short compared with the core size, and the quasiclassical approximation is relevant. The quasiclassical angular momentum  $L_z$  is a continuous variable; thus the anomalous branch crosses zero as a function of  $L_z$  at  $L_z = 0$  and the spectral flow can occur along this branch between the vacuum states with  $E < 0$  to the excited states with  $E > 0$ . Such spectral flow occurs during the motion of the vortex with respect to the normal component, where it is caused by the interaction with impurities in superconductors or with the thermal scattering states in superfluids. In the quasiclassical approximation, the Doppler shifted spectrum of the fermions in the moving vortex has the form

$$E(L_z, \mathbf{p}) = -\omega_0(p_z)L_z + (\mathbf{v}_s - \mathbf{v}_L) \cdot \mathbf{p}. \quad (105)$$

Here the momentum  $\mathbf{p}$  is assumed to be at the Fermi surface:  $\mathbf{p} = (p_F \sin \theta \sin \alpha, p_F \sin \theta \cos \alpha, p_F \cos \theta)$ . An azimuthal angle  $\alpha$  is the canonically conjugated to the angular momentum  $L_z$ . This allows us to write the Boltzmann equation for the distribution function,  $n(L_z, \alpha)$  at fixed  $p_z = p_F \cos \theta$ .

$$\begin{aligned} \partial_t n - \omega_0 \partial_{\alpha} n - \partial_{\alpha}((\mathbf{v}_s - \mathbf{v}_L) \cdot \mathbf{p}) \partial_{L_z} n \\ = - \frac{n(L_z, \alpha) - n_{\text{eq}}(L_z, \alpha)}{\tau} \end{aligned} \quad (106)$$

where the collision time  $\tau$  characterizes the interaction of the bound state fermions with impurities or with the thermal fermions in the normal component outside the vortex core and equilibrium distribution function is:

$$n_{\text{eq}}(L_z, \alpha) = f(E - (\mathbf{v}_n - \mathbf{v}_L) \cdot \mathbf{p}) = f(-\omega_0 L_z + (\mathbf{v}_s - \mathbf{v}_n) \cdot \mathbf{p}) \quad (107)$$

where  $f(E) = (1 + \exp(E/T))^{-1}$  is the Fermi-function. Introducing the shifted variable

$$l = L_z - (\mathbf{v}_s - \mathbf{v}_n) \cdot \mathbf{p}, \quad (108)$$

one obtains the equation for  $n(l, \alpha)$

$$\begin{aligned} \partial_t n - \omega_0 \partial_\alpha n - \partial_\alpha ((\mathbf{v}_n - \mathbf{v}_L) \cdot \mathbf{k}) \partial_l n \\ = - \frac{n(l, \alpha) - f(-\omega_0 l)}{\tau}, \end{aligned} \quad (109)$$

which does not contain  $\mathbf{v}_s$ . To find the force acting on the vortex from the heat bath environment, we are interested in the evolution of the total momentum of quasiparticles in the vortex core:

$$\mathbf{P} = \sum \mathbf{p} = \int_{-p_F}^{p_F} \frac{dp_z}{2\pi} \mathbf{P}(p_z), \quad \mathbf{P}(p_z) = \frac{1}{2} \int dl \frac{d\alpha}{2\pi} n(l, \alpha) \mathbf{p} \quad (110)$$

It appears that the equation for  $\mathbf{P}(p_z)$  can be written in a closed form

$$\begin{aligned} \partial_t \mathbf{P}(p_z) - \omega_0 \hat{z} \times \mathbf{P}(p_z) + \frac{\mathbf{P}(p_z)}{\tau} = \\ - \frac{1}{4} p_F^2 \sin^2 \theta \hat{z} \times (\mathbf{v}_n - \mathbf{v}_L) (f(\Delta(T)) - f(-\Delta(T))). \end{aligned} \quad (111)$$

Here we take into account that  $\int dl \partial_l n$  is limited by the bound states below the gap  $\Delta(T)$  of the bulk liquid: above the gap  $\Delta(T)$  the spectrum of fermions is continuous, i.e. the interlevel distance  $\omega_0 = 0$ .

In the steady state vortex motion one has  $\partial_t \mathbf{P}(p_z) = 0$ . Then, since  $f(\Delta(T)) - f(-\Delta(T)) = \tanh(\Delta(T)/2T)$ , one obtains the following contribution to the momentum from the heat bath to the core fermions due to the spectral flow of bound states below  $\Delta(T)$

$$\begin{aligned} \mathbf{F}_{\text{bsf}} = \int_{-p_F}^{p_F} \frac{dp_z}{2\pi} \frac{\mathbf{P}(p_z)}{\tau} = \frac{\kappa}{4} \tanh \frac{\Delta(T)}{2T} \\ \int_{-p_F}^{p_F} \frac{dp_z}{2\pi} \frac{p_F^2 - p_z^2}{1 + \omega_0^2 \tau^2} [(\mathbf{v}_L - \mathbf{v}_n) \omega_0 \tau + \hat{z} \times (\mathbf{v}_L - \mathbf{v}_n)]. \end{aligned} \quad (112)$$

The spectral flow of unbound states above  $\Delta(T)$  is not suppressed, the corresponding  $\omega_0 \tau = 0$ , since the distance between the levels in the continuous spectrum is  $\omega_0 = 0$ . This gives

$$\begin{aligned} \mathbf{F}_{\text{usf}} = \\ \frac{\kappa}{4} p_F^2 \int_{-p_F}^{p_F} \frac{dp_z}{2\pi} \sin^2 \theta \left( 1 - \tanh \frac{\Delta(T)}{2T} \right) \hat{z} \times (\mathbf{v}_L - \mathbf{v}_n). \end{aligned} \quad (113)$$

Thus the total nondissipative (transverse) and frictional (longitudinal) parts of the spectral-flow force are

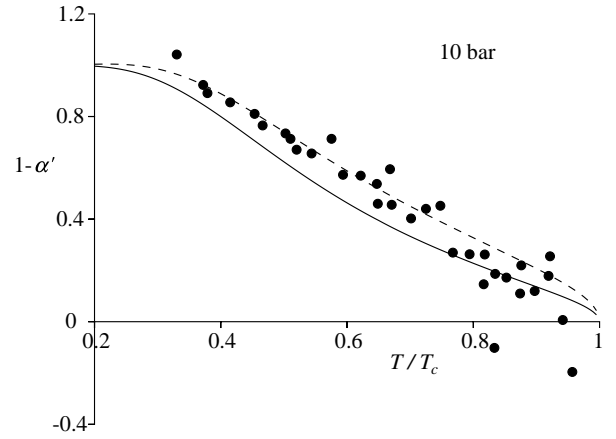


FIG. 25. Experimental values of  $1 - \alpha'$  at 10 bar compared with theoretical prediction Eq. (116). From Ref. [63].

$$\begin{aligned} \mathbf{F}_{\text{sf}}^\perp = \frac{\kappa}{4} \int_{-p_F}^{p_F} \frac{dp_z}{2\pi} (p_F^2 - p_z^2) \times \\ \left[ 1 - \tanh \frac{\Delta(T)}{2T} \frac{\omega_0^2 \tau^2}{1 + \omega_0^2 \tau^2} \right] \hat{z} \times (\mathbf{v}_L - \mathbf{v}_n), \end{aligned} \quad (114)$$

$$\begin{aligned} \mathbf{F}_{\text{sf}}^\parallel = (\mathbf{v}_L - \mathbf{v}_n) \frac{\kappa}{4} \tanh \frac{\Delta(T)}{2T} \times \\ \int_{-p_F}^{p_F} \frac{dp_z}{2\pi} (p_F^2 - p_z^2) \frac{\omega_0 \tau}{1 + \omega_0^2 \tau^2} \end{aligned} \quad (115)$$

In the limit  $\omega_0 \tau \ll 1$  the friction force disappears, while the transverse spectral flow force is maximal and coincides with that obtained for the continuous vortex in Eq.(101) with the same value of  $\mathcal{C}_0 = (1/4) \int_{-p_F}^{p_F} dp_z (p_F^2 - p_z^2) = p_F^3/3\pi^2$ . In general case the result in Eqs.(114),(115) is complicated since both  $\omega_0$  and  $\tau$  depend on  $p_z$ . However if one neglects this dependence and add the Magnus and Iordanskii forces one obtains the Eq.(103) for all  $T$ . If the temperature is not too high, so that  $\tanh \Delta(T)/2T \approx 1$ , one obtains the Eq.(102) for the renormalized spectral flow parameter.

Comparison of Eq. (103) with experiment should take into account that neither  $\omega_0$  nor  $\tau$  are known with good accuracy. However the following combination of the mutual friction coefficients does not depend on these parameters explicitly:

$$1 - \alpha' = \frac{1 - d_\perp}{d_\parallel^2 + (1 - d_\perp)^2} = \frac{\rho_s}{\rho} \left[ \tanh \frac{\Delta(T)}{2k_B T} \right]^{-1}. \quad (116)$$

This equation is compared to the experimental data on mutual friction in  $^3\text{He-B}$  [63] in Fig. 25. The agreement is excellent in view of the approximations in the theory. This shows that the chiral anomaly is relevant for the interaction of condensed matter vortices (analogue of strings) with fermionic quasiparticles (analogue of quarks and leptons). For continuous vortices in  $^3\text{He-A}$  the spectral flow of fermions between the vacuum (superfluid

ground state) and matter (heat bath of positive energy particles forming the normal component) dominates at any relevant temperature. For singular vortices in  $^3\text{He-B}$  it is important at  $T \sim T_c$  and vanishes at  $T \ll T_c$ .

It is interesting that for a homogeneous vacuum the fermionic charge (momentum) is conserved separately in the vacuum (ground state) and in the heat bath of excitations. Topological defects are thus the mediators of the transfer of momentum between these two subsystems. The motion of a vortex across the flow changes both the topological charge of the vacuum (say, the winding number of superflow in a torus geometry) and the fermionic charge (angular momentum in the same geometry). All these processes are similar to those involved in the cosmological production of baryons and can thus be investigated in detail.

However, it is important to note that although the spectral flow leads to anomalous creation of fermionic charge from the vacuum, the total fermionic charge of the vacuum plus matter remains conserved. There is also no intrinsic bias in this process for the direction of the charge transfer: from vacuum to matter or in the opposite direction. Thus, the necessary conditions for the operation of this mechanism, if the non-trivial result like the apparent positive baryonic charge of the matter in our Universe is required, are the system in non-equilibrium state plus some symmetry breaking which biases the direction of the charge transfer. How such conditions may be realized in the early Universe is not clear now. But it is strongly believed that the broken P and CP invariances play crucial role.

In the  $^3\text{He}$  case the situation is completely under control: The relevant symmetry breaking is modeled by applying rotation or a magnetic field, while the nonequilibrium case can be achieved by applying an external superflow or acceleration.

Thus the experimental verification of momentogenesis in superfluid  $^3\text{He}$  supports current ideas on cosmological baryogenesis via spectral flow and points to a future where several cosmological problems can be modeled and studied in  $^3\text{He}$ . Now let us consider the opposite effect which leads to the analog of magnetogenesis.

#### 4. ANALOG OF MAGNETOGENESIS: VORTEX TEXTURES GENERATED BY NORMAL-SUPERFLUID COUNTERFLOW

From Eq. (94) it follows that the magnetic field configuration can absorb the fermionic charge. If this magnetic field has a helicity, it acquires an excess of right-moving particles over the left-moving particles:

$$(n_R - n_L)_A = \frac{1}{2\pi^2} \mathbf{A} \cdot (\nabla \times \mathbf{A}) . \quad (117)$$

The right-hand side is the so called Chern-Simons (or topological) charge of the magnetic field.

The transformation of particles into a magnetic field configuration opens the possibility for the cosmological origin of galactic magnetic fields from a system of fermions. This is the essential step in the scenario described by Joyce and Shaposhnikov [73]. In this scenario the initial excess of the right electrons,  $e_R$ , could have been generated in the early Universe. This excess could survive until the electroweak phase transition (at about  $10^{-10}$  s after the big bang) when anomalous lepton (and baryon) number violating processes become efficient to erase the excess. However it appears that well before the electroweak transition the instability develops, at which the excess of the right electrons is transformed into a hypermagnetic field. Then, when the electroweak transition occurs, it transforms a part of the hypermagnetic field into the electromagnetic field, so that the universe contains a primordial (electromagnetic) magnetic field.

Now we discuss the corresponding process of the fermionic charge to magnetic field transformation in  $^3\text{He-A}$ . In our case it is the quasiparticle momentum, which plays the part of the relevant fermionic charge. The net quasiparticle momentum is generated by the relative flow of normal and superfluid components. This fermionic charge is transformed via the chiral anomaly into the order parameter texture, which as we have seen plays the part of the magnetic field. This transformation occurs as the instability of the excess of the momentum towards the formation of the  $\hat{\mathbf{l}}$ -textures and represents the counterflow instability in  $^3\text{He-A}$ , which has been intensively discussed theoretically and recently investigated experimentally in the Helsinki rotating cryostat [75]. Thus the  $^3\text{He-A}$  analogy closely follows the cosmological scenario described in [73].

Let us discuss this instability. In the presence of counterflow,  $\mathbf{w} = \mathbf{v}_n - \mathbf{v}_s$ , of the normal component of  $^3\text{He-A}$  liquid with respect to the superfluid, the  $\hat{\mathbf{l}}$ -vector is oriented along the flow,  $\hat{\mathbf{l}}_0 \parallel \mathbf{w}$ . We are interested in the stability condition for such homogeneous counterflow towards generation of the inhomogeneous perturbations  $\delta\hat{\mathbf{l}}$

$$\hat{\mathbf{l}} = \hat{\mathbf{l}}_0 + \delta\hat{\mathbf{l}}(\mathbf{r}, t) , \quad (118)$$

keeping in mind that the space and time dependence of  $\delta\hat{\mathbf{l}}$  correspond to “hyperclectric field”  $\mathbf{E} = k_F \partial_t \delta\hat{\mathbf{l}}$  and a “hypermagnetic field”  $\mathbf{B} = k_F \nabla \times \delta\hat{\mathbf{l}}$ .

It is important for our consideration that the  $^3\text{He-A}$  liquid is anisotropic in the same manner as a nematic liquid crystal. For the relativistic fermions this means that their motion is determined by the geometry of some effective spacetime which in  $^3\text{He-A}$  is described by the metric tensor in Eq. (75). As we have already discussed above, in the presence of counterflow the energy of quasiparticles is Doppler shifted by the amount  $\mathbf{p} \cdot \mathbf{w}$ . Since the quasiparticles are concentrated near the gap nodes, this energy shift is constant and opposite for two gap nodes:  $\mathbf{p} \cdot \mathbf{w} \approx \pm p_F (\hat{\mathbf{l}}_0 \cdot \mathbf{w})$ . The counterflow therefore produces what would be an effective chemical potential in particle physics, which has opposite sign for the right-

and left-handed particles:

$$\mu_R = -\mu_L = p_F(\hat{\mathbf{l}}_0 \cdot \mathbf{w}). \quad (119)$$

The kinetic energy of the counterflow is

$$E_{\text{kin}} = \frac{1}{2} \mathbf{w} \rho_n \mathbf{w}. \quad (120)$$

Here the density of the normal component is a tensor in the anisotropic  $^3\text{He-A}$ , and only the longitudinal component is involved.

Let us consider the low-temperature limit  $T \ll T_c$ , where  $T_c \sim \Delta_0$  is the superfluid transition temperature. Then using expression for the longitudinal density of the normal component of  $^3\text{He-A}$  [20]

$$\rho_n = \pi^2 \rho \frac{m_3^*}{m_3} \left( \frac{k_B T}{\Delta_0} \right)^2 \quad (121)$$

and also the  $^3\text{He-A}$  equivalent of the chemical potential (119) one obtains

$$E_{\text{kin}} \approx \frac{1}{6} m_3^* k_F^3 \frac{T^2}{\Delta_0^2} (\hat{\mathbf{l}}_0 \cdot \mathbf{w})^2 \equiv \frac{1}{6} \sqrt{-g} T^2 \mu_R^2. \quad (122)$$

In the last equality an over-all constant appears to be the square root of the determinant of an effective metric in  $^3\text{He-A}$ :  $\sqrt{-g} = 1/c_{\parallel} c_{\perp}^2 = m_3^* k_F / \Delta_0^2$ . In relativistic theories the rhs of Eq. (122) is exactly the energy density of the massless right-handed electrons in the presence of the chemical potential  $\mu_R$ . Thus the kinetic energy, stored by the counterflow, is exactly analogous to the energy stored by the right-handed electrons. The same analogy occurs between the net quasiparticle linear momentum,  $\mathbf{P} = \rho_n \mathbf{w}$ , along  $\hat{\mathbf{l}}_0$  and the chiral charge of the right electrons:

$$n_R \equiv \frac{1}{p_F} \mathbf{P} \cdot \hat{\mathbf{l}}_0. \quad (123)$$

The inhomogeneity which absorbs the fermionic charge, is represented by a magnetic field configuration in real physical vacuum and by a  $\delta\hat{\mathbf{l}}$ -texture in  $^3\text{He-A}$ . However, eq. (117) applies in both cases, if in  $^3\text{He-A}$  we use the standard identification  $\mathbf{A} = k_F \delta\hat{\mathbf{l}}$ .

Just as in the particle physics case, we now consider the instability towards the production of the (magnetic) texture due to the excess of chiral particles. This instability can be seen by considering the gradient energy of the inhomogeneous texture on the background of the superflow. In the geometry of the superflow, the textural contribution to the free energy of the  $\delta\hat{\mathbf{l}}$ -vector is completely equivalent to the conventional energy of the hypermagnetic field [112]

$$\begin{aligned} F_{\text{grad}} &= \ln \left( \frac{\Delta_0^2}{T^2} \right) \frac{p_F^2 v_F}{24\pi^2 \hbar} (\hat{\mathbf{l}}_0 \times (\nabla \times \delta\hat{\mathbf{l}}))^2 \\ &\equiv \frac{\sqrt{-g}}{4\pi e_{\text{eff}}^2} g^{ij} g^{kl} F_{ik} F_{jl} = F_{\text{mag}}. \end{aligned} \quad (124)$$

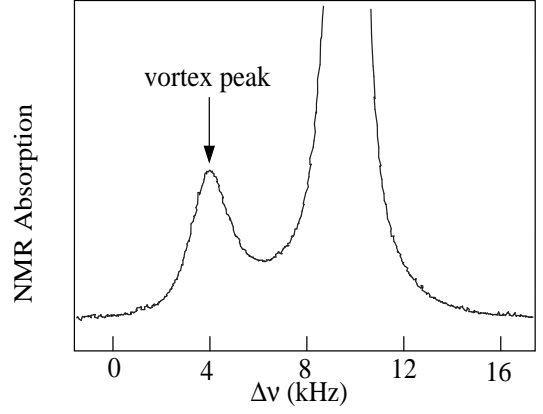


FIG. 26. The NMR signal from array of ATC vortices in the container. The position of the satellite peak indicates the type of the vortex, while the intensity is proportional to the number of vortices of this type in the cell.

Here  $F_{ik} = \nabla_i A_k - \nabla_k A_i$  and we again have included the effective anisotropic metric in Eq. (75) appropriate for  $^3\text{He-A}$ .

It is interesting that the logarithmic factor in the gradient energy plays the part of the running coupling  $e_{\text{eff}}^{-2} = (1/3\pi\hbar c) \ln(\Delta_0/T)$  in particle physics, where  $e_{\text{eff}}$  is the effective hyperelectric charge; while the gap amplitude  $\Delta_0$ , the ultraviolet cutoff, plays the part of the Planck energy scale. Now if one has the counterflow in  $^3\text{He-A}$ , or its equivalent – an excess of chiral charge produced by the chemical potential  $\mu_R$  – the anomaly gives rise to an additional effective term in the magnetic energy, corresponding to the interaction of the charge absorbed by the magnetic field with the chemical potential. This effective energy term is:

$$\begin{aligned} F_{CS} &= (n_R - n_L) \mu_R = \frac{1}{2\pi^2} \mu_R \mathbf{A} \cdot (\nabla \times \mathbf{A}) \\ &= \frac{3\hbar}{2m} \rho (\hat{\mathbf{l}}_0 \cdot \mathbf{w}) (\delta\hat{\mathbf{l}} \cdot \nabla \times \delta\hat{\mathbf{l}}), \end{aligned} \quad (125)$$

The right-hand side corresponds to the well known anomalous interaction of the counterflow with the  $\hat{\mathbf{l}}$ -texture in  $^3\text{He-A}$ , where  $\rho$  is the mass density of  $^3\text{He}$  [112] (the additional factor of 3/2 enters due to nonlinear effects).

For us the most important property of this term is that it is linear in the derivatives of  $\delta\hat{\mathbf{l}}$ . Its sign thus can be negative, while its magnitude can exceed the positive quadratic term in Eq. (124). This leads to the helical instability where the inhomogeneous  $\delta\hat{\mathbf{l}}$ -field is formed. During this instability the kinetic energy of the quasiparticles in the counterflow (analog of the energy stored in the fermionic degrees of freedom) is converted into the energy of inhomogeneity  $\nabla \times \delta\hat{\mathbf{l}}$ , which is the analog of the magnetic energy of the hypercharge field.

When the helical instability develops in  $^3\text{He-A}$ , the final result is the formation of a  $\hat{\mathbf{l}}$ -texture, which corre-



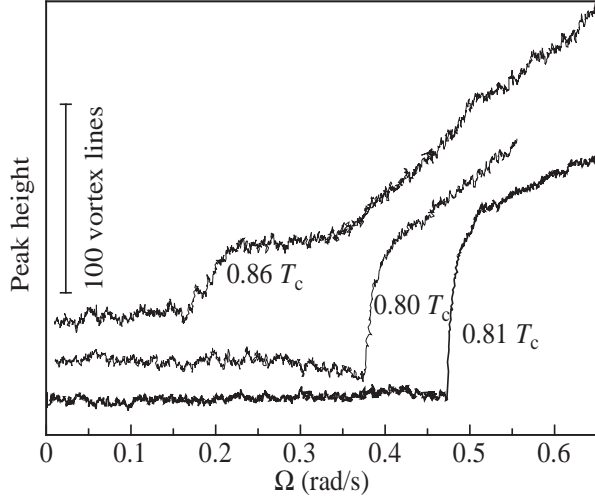


FIG. 27. Time dependence of the satellite peak height of the continuous vortices. Initially vortices are not present in the vessel. When the velocity of the counterflow  $\mathbf{w}$  in the  $\hat{\mathbf{l}}_0$  direction (corresponding to the chemical potential  $\mu_R$  of the chiral electrons) exceeds some critical value, the instability occurs and the container becomes filled with the  $\hat{\mathbf{l}}$ -texture (hypermagnetic field) forming the vortex array.

sponds to the free energy minimum in the rotating container. This is a periodic  $\hat{\mathbf{l}}$ -texture, where the elementary cell represents a so-called Anderson-Toulouse-Chechetkin (ATC) continuous vortex (Fig. 23). ATC vortices give rise to a characteristic satellite peak in the  $^3\text{He}$  NMR absorption spectrum: their number is directly proportional to the height of this peak (Fig. 26).

By accelerating the container into rotation, starting from the state with vortex-free counterflow (ie. with fermionic charge, but no hypermagnetic field), we observe the helical instability as a sudden discontinuity, when the vortex satellite is formed (Fig. 27). The peak height jumps from zero to a magnitude which almost corresponds to the equilibrium vortex state, which means that the counterflow is essentially reduced. Most of the counterflow (fermionic charge) thus becomes converted into vortex texture (magnetic field).

Together with the results in [62], this shows that the chiral anomaly is an important mechanism for the interaction of vortex textures (the analogue of the hypercharge magnetic fields and cosmic strings) with fermionic excitations (analogue of quarks and leptons). These two experiments verified both processes which are induced by the anomaly: the nucleation of fermionic charge from the vacuum in [62] and the inverse process of the nucleation of an effective magnetic field from the fermion current [76].

## 5. VORTEX MASS: CHIRAL FERMIONS IN STRONG MAGNETIC FIELD

Till now we assumed that the mass  $M_V$  of the vortex can be neglected in the vortex dynamics: The term  $M_V \partial_t \mathbf{v}_L$  in the force balance equation for the vortex contains the time derivative and thus at low frequencies of the vortex motion it can be neglected compared to the other forces, which are directly proportional to  $\mathbf{v}_L$ . Here we estimate the vortex mass in the BCS superfluids and superconductors and relate it to the peculiar phenomena in quantum field theory. There are several contributions to the mass of the vortex. We start from the contribution, which is relevant for the Bose superfluid  $^4\text{He}$ .

### a. "Relativistic" mass of the vortex

In the hydrodynamic theory the mass of the vortex is nonzero due to compressibility of the liquid. Since the sound propagation in fluids is similar to the light propagation in the vacuum, the hydrodynamic energy of the vortex, soliton or other extended object moving in the liquid is connected with its hydrodynamic mass by per unit length are connected by the "relativistic" equation,  $E = ms^2$  where the speed of sound  $s$  substitutes the speed of light [113,115,114,116]. Thus the hydrodynamic mass of the vortex loop of length  $L$  at  $T = 0$  is according to Eq.(14):

$$M_{\text{compr}} = \frac{E_{\text{kin}}}{s^2} = \frac{\rho \kappa^2 L}{4\pi s^2} \ln \frac{L}{\xi}. \quad (126)$$

For Fermi superfluids  $s$  is of order the Fermi velocity  $v_F \sim p_F/m$  ( $m$  is the mass of the electron or of the  $^3\text{He}$  atom), and the estimation for the hydrodynamic mass of the vortex loop of length  $L$  is  $\sim \rho a^2 L \ln \frac{L}{\xi}$ , where  $a$  is interatomic distance. For superfluid  $^4\text{He}$ , where the core size  $\xi \sim a$ , this hydrodynamic vortex mass is of order the mass of the liquid concentrated in the vortex core,  $\sim \rho a^2 L$ . However for superfluid phases of  $^3\text{He}$  and for superconductors, where  $\xi \gg a$ , it is much less than  $\rho \xi^2 L$  and the other contributions become important.

### b. Bound states contribution to the mass of singular vortex.

It appears that the most important contribution to the vortex mass originates from the quasiparticle occupying the bound states in the vortex core and thus forming the normal component concentrated in the core. For the vortices in conventional superconductors and in  $^3\text{He-B}$  this contribution to the vortex mass depends on  $\omega_0 \tau$  and in the clean limit case it is proportional to the mass of the liquid in the vortex core, as was first found by Kopnin in superconductors [117] and in superfluid  $^3\text{He-B}$  [118]:  $M_{\text{Kopnin}} \rho \xi^2 L$ . This core mass is essentially larger than



the logarithmically divergent contribution, which comes from the compressibility. In spite of the logarithmic divergence, the latter contains the speed of sound in the denominator and thus is smaller by factor  $(a/\xi)^2 \ll 1$ , where  $a$  is the interatomic distance. The compressibility mass of the vortex dominates in Bose superfluids, where the core size is small,  $\xi \sim a$ .

According to Kopnin theory the core mass comes from the fermions trapped in the vortex core [117,118,120,121]. This Kopnin mass of the vortex can be derived using the phenomenological approach. Let us consider the limit of low  $T$  and the superclean regime  $\omega_0\tau \gg 1$  [121]. If the vortex moves with velocity  $\mathbf{v}_L$  with respect to the superfluid component, the fermionic energy spectrum in the vortex frame is Doppler shifted and has the form in Eq.(105):  $E = E_0(\nu) - \mathbf{p} \cdot \mathbf{v}_L$ , where  $\nu$  stands for the fermionic degrees of freedom in the stationary vortex. The summation over fermionic degrees of freedom leads to the extra linear momentum of the vortex  $\propto \mathbf{v}_L$ :

$$\mathbf{P} = \sum_{\nu} \mathbf{p} \theta(-E) = \sum_{\nu} \mathbf{p} (\mathbf{k} \cdot \mathbf{v}_L) \delta(E_0) = M_{\text{Kopnin}} \mathbf{v}_L,$$

$$M_{\text{Kopnin}} = \frac{1}{2} \sum_{\nu} \mathbf{p}_{\perp}^2 \delta(E_0). \quad (127)$$

For the axisymmetric vortex, where  $E_0 = -L_z \omega_0(p_z)$  and  $\sum_{\nu} = \int dL_z dp_z dz / 2\pi$ , one has

$$M_{\text{Kopnin}} = L \int_{-p_F}^{p_F} \frac{dp_z}{4\pi} \frac{p_F^2 - p_z^2}{\omega_0(p_z)} \quad (128)$$

The Eq.(128) can be also obtained from the time dependent kinetic equation (106). It is the coefficient in the contribution to the longitudinal force, which is linear in external frequency  $\omega$ :  $\mathbf{F}_{\text{sf}}^{\parallel} = -i\omega M_{\text{Kopnin}} \mathbf{v}_L$ .

Note that this vortex mass is determined in essentially the same way as the normal component density in the bulk system. The Kopnin vortex mass is nonzero if the density of fermionic states is finite in the vortex core. The only difference is that the density of states is determined by the interlevel spacing  $\omega_0$  in the core:  $N(0) \propto 1/\omega_0$ , which gives for the Kopnin vortex mass per unit length an estimation:  $M_{\text{Kopnin}} \sim p_F^3/\omega_0 \sim \rho \xi^2$ . The more stronger connection to the normal component fraction in the core will be given in the next subsection on the example of the continuous vortex core.

### c. Kopnin mass of continuous vortex: connection to chiral fermions in magnetic field.

The continuous-core vortex in  $^3\text{He-A}$  is again the best model which helps to understand the vortex core mass. The continuous-core model can be also considered in the other Fermi superfluids and superconductors: the singular core can be smoothen, so that the  $1/r$ -singularity of the superfluid velocity is removed, by introducing the

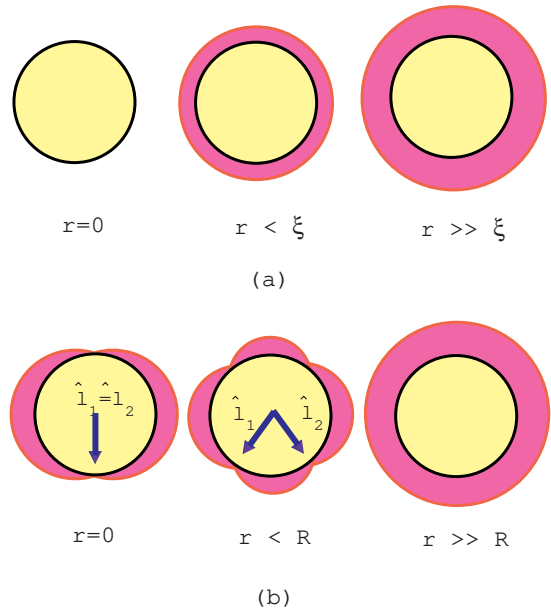


FIG. 28. Singular vortex vs soft-core vortex. (a) In the singular vortex the gap continuously decreases and becomes zero on the vortex axis (at  $r = 0$ ) (b) For some vortices it is energetically favourable to escape the nullification of the order parameter at  $r = 0$ . Instead, within the smooth core,  $r < R$ , the point gap nodes appear in the spectrum of fermions [124]. The unit vectors  $\hat{\mathbf{l}}_1$  and  $\hat{\mathbf{l}}_2$  show the directions to the nodes at different  $r$ . Close to the gap nodes the spectrum of fermions is similar to that in  $^3\text{He-A}$ .

point gap nodes in the core region. As a result the superfluid/superconducting state in the vortex core of any system acquires the properties of the A-phase of superfluid  $^3\text{He}$  with its continuous vorticity and point gap nodes [124,125]. After that one can easily separate different contributions to the vortex mass. Actually this is not only the model: The spontaneous smoothening of the velocity singularity occurs in the core of both types of vortices observed in  $^3\text{He-B}$  [125]; in heavy fermionic and high- $T_c$  superconductors such smoothening can occur due to admixture of different pairing states in the vortex core.

For the smoothened singly quantized vortices in  $^3\text{He-B}$  and superconductors one has two  $\hat{\mathbf{l}}$ -vectors:  $\hat{\mathbf{l}}_1$  and  $\hat{\mathbf{l}}_2$ , each for each of two spin projections. The simplest distribution of both fields is given by Eq.(100), where now  $\hat{\mathbf{l}}_1(0) = \hat{\mathbf{l}}_2(0) = -\hat{\mathbf{z}}$  and  $\hat{\mathbf{l}}_1(\infty) = -\hat{\mathbf{l}}_2(\infty) = \hat{\mathbf{r}}$  [125]. The region of radius  $R$ , where the texture of  $\hat{\mathbf{l}}$ -vectors is concentrated, represents the smoothened (or soft) core of the vortex.

For the continuous vortex the normal component associated with the vortex can be considered as the local quantity, determined at each point in the vortex core. Such consideration is valid for the smooth core with the radius  $R \gg \xi$ , where the local classical description of the fermionic spectrum can be applied. The main contribution comes from the point gap nodes, where the classical

spectrum has the form  $E_0 = \sqrt{v_F^2(p - p_F)^2 + \Delta_0^2(\hat{\mathbf{p}} \times \hat{\mathbf{l}})^2}$  and  $\Delta_0$  is the gap amplitude. In the presence of the gradient of  $\hat{\mathbf{l}}$ -field, which acts on the quasiparticles as an effective magnetic field, this gapless spectrum leads to the nonzero local DOS, discussed in Sec.III.3a for the relativistic chiral fermions. To apply the DOS in Eq(93) to the case of the anisotropic  $^3\text{He-A}$ , one must make the covariant generalization of DOS introducing the general metric tensor and then substitute it by the effective  $^3\text{He-A}$  metrics which describes the anisotropy of  $^3\text{He-A}$ . The general form of the DOS of the chiral fermions in the curved space is

$$N(0) = \frac{|e|}{2\pi^2} \sqrt{-g} \sqrt{\frac{1}{2} g^{ij} g^{kl} F_{ik} F_{jl}} \quad (129)$$

One now can apply this to the  $^3\text{He-A}$  where  $|e| = 1$ , and the metric tensor is given by Eq.(75). Neglecting the dependence the small velocity field  $v_s$  in the smooth core, one obtains the following local DOS for the fermions in the  $\hat{\mathbf{l}}$ -texture at  $T = 0$ :

$$N(0, \mathbf{r}) = \frac{p_F^2}{2\pi^2 \Delta_A} |(\hat{\mathbf{l}} \times (\vec{\nabla} \times \hat{\mathbf{l}}))| \quad (130)$$

This DOS can be inserted to the expression for the local density of the normal component at  $T = 0$  (see Eq.(5.24) in the review [128]):

$$(\rho_n)_{ij}(\mathbf{r}) = \hat{l}_i \hat{l}_j p_F^2 N(0, \mathbf{r}) . \quad (131)$$

For the axisymmetric continuous vortex one has

$$N(0, \mathbf{r}) = \frac{p_F^2}{2\pi^2 \Delta_A} \sin \eta |\partial_r \eta|. \quad (132)$$

The integral of this normal density tensor over the cross section of the soft core gives the Kopnin mass of the vortex in the local density representation

$$\begin{aligned} M_{\text{Kopnin}} &= \int d^2 r (\hat{\mathbf{v}}_L \cdot \hat{\mathbf{l}})^2 p_F^2 N(0, \mathbf{r}) \\ &= \frac{p_F^2}{4\pi^2 \Delta_A} \int d^2 r \sin^3 \eta(r) |\partial_r \eta| \end{aligned} \quad (133)$$

where  $\hat{\mathbf{v}}_L$  is the unit vector in the direction of vortex velocity. The same equation for the mass can be obtained from Eq.(128) using the exact expression for the interlevel distance  $\omega_0(p_z)$  [121].

Since  $v_F/\Delta_0 \sim \xi$  one obtains that the Kopnin mass of the continuous vortex  $\sim \rho \xi R$ , i.e. it is linear in the dimension  $R$  of the core [127]. Thus it follows that the area law for the vortex mass is valid only for vortices with the core size of order  $\xi$  (i.e.  $R \sim \xi$ ).

Note that the vortex mass discussed comes from the normal component trapped by the vortex and thus moving with the vortex velocity,  $\mathbf{v}_n = \mathbf{v}_L$ . In this consideration it was assumed that  $\omega_0 \tau \gg 1$ . In this limit the

normal component in the core and the normal component in the heat bath do not interact with each other and thus can move with different velocities. The local hydrodynamic energy of the normal component trapped by the vortex is

$$F = \frac{1}{2} (\rho_n)_{ij}(\mathbf{r}) (\mathbf{v}_L - \mathbf{v}_s)_i (\mathbf{v}_L - \mathbf{v}_s)_j \quad (134)$$

This can be rewritten in the form, which is valid also for the chiral fermions:

$$F = \frac{\mu_R^2 + \mu_L^2}{8\pi^2} \sqrt{-g} \sqrt{\frac{1}{2} g^{ij} g^{kl} F_{ik} F_{jl}} \quad (135)$$

where, as before in Eq.(119), the chemical potential of the left and right fermions in  $^3\text{He-A}$  are expressed in terms of the counterflow:  $\mu_R = -\mu_L = p_F(\hat{\mathbf{l}} \cdot \mathbf{w})$ . The Eq.(135) represents the magnetic energy of the chiral particles with finite chemical potential in strong magnetic field  $B \gg \mu^2$ .

#### d. Associated hydrodynamic mass

Recently the problem of another vortex mass of the hydrodynamics origin was raised in Ref. [122]. It is the so-called backflow mass discussed by Baym and Chandler [123], which also can be proportional to the core area. Here we compare these two contributions in the superclean regime and at low  $T \ll T_c$  using the model of the continuous core. The associated (or induced) mass appears when, say, an external body moves in the superfluid. This mass depends on the geometry of the body. For the moving cylinder of radius  $R$  it is the mass of the liquid displaced by the cylinder,

$$M_{\text{associated}} = \pi R^2 \rho , \quad (136)$$

which is to be added to the actual mass of the cylinder to obtain the total inertial mass of the body. In superfluids this part of superfluid component moves with external body and thus can be associated with the normal component. The similar mass is responsible for the normal component in porous materials and in aerogel, where some part of superfluid is hydrodynamically trapped by the pores. It is removed from the overall superfluid motion and thus becomes the part of the normal component.

In the case when the vortex is trapped by the wire of radius  $R \gg \xi$ , such that the vortex core is represented by the wire, the Eq.(136) gives the vortex mass due to the backflow around the moving core. This is the simplest realization of the backflow mass of the vortex discussed by Baym and Chandler [123]. For such vortex with the wire-core the Baym-Chandler mass is the dominating mass of the vortex. The Kopnin mass which can result from the normal excitations trapped near the surface of the wire is essentially less.

Let us now consider the Baym-Chandler mass for the free vortex at  $T = 0$  using again the continuous-core

model. In the wire-core vortex this mass arises due to the backflow caused by the inhomogeneity of  $\rho_s$ :  $\rho_s(r > R) = \rho$  and  $\rho_s(r < R) = 0$ . Similar but less severe inhomogeneity of  $\rho_s = \rho - \rho_n$  occurs in the continuous-core vortex due to the nonzero local normal density in Eq.(131). Due to the profile of the local superfluid density the external flow is disturbed near the core according to continuity equation

$$\nabla \cdot (\rho_s \mathbf{v}_s) = 0 \quad . \quad (137)$$

If the smooth core is large,  $R \gg \xi$ , the deviation of the superfluid component in the smooth core from its asymptotic value outside the core is small:  $\delta\rho_s = \rho - \rho_s \sim (\xi/R)\rho \ll \rho$  and can be considered as perturbation. Thus if the asymptotic value of the velocity of the superfluid component with respect of the core is  $\mathbf{v}_{s0} = -\mathbf{v}_L$ , the disturbance  $\delta\mathbf{v}_s = \nabla\Phi$  of the superflow in the smooth core is given by:

$$\rho \nabla^2 \Phi = v_{s0}^i \nabla^j (\rho_n)_{ij} \quad . \quad (138)$$

The kinetic energy of the backflow gives the Baym-Chandler mass of the vortex

$$M_{BC} = \frac{\rho}{v_{s0}^2} \int d^2r (\nabla\Phi)^2 \quad , \quad (139)$$

In the simple approximation, when the normal component in Eq.(131) is considered as isotropic, one obtains

$$M_{BC} = \frac{1}{2\rho} \int d^2r \rho_n^2(r) \sim \rho \xi^2 \quad . \quad (140)$$

The Baym-Chandler mass does not depend on the core radius  $R$ , since the large area  $R^2$  of integration in Eq.(140) is compensated by small value of the normal component in the rarified core,  $\rho_n \sim \rho(\xi/R)$ . That is why if the smooth core is large,  $R \gg \xi$ , this mass is parametrically smaller than the Kopnin mass in Eq.(133).

In conclusion, both contributions to the mass of the vortex result from the mass of the normal component trapped by the vortex. The difference between Kopnin mass and Baym-Chandler backflow mass is only in the origin of the normal component trapped by the vortex. The relative importance of two masses depends on the vortex core structure: (1) For the free continuous vortex with the large core size  $R \gg \xi$ , the Kopnin mass dominates:  $M_{Kopnin} \sim \rho R \xi \gg M_{BC} \sim \rho \xi^2$ . (2) For the vortex trapped by the wire of radius  $R \gg \xi$ , the Baym-Chandler mass is proportional to the core area,  $M_{BC} \sim \rho R^2$ , and is parametrically larger than the Kopnin mass. (3) For the free vortex core with the core radius  $R \sim \xi$  the situation is not clear since the continuous core approximation does not work any more. But extrapolation of the result in Eq.(140) to  $R \sim \xi$  suggests that the Baym-Chandler mass can be comparable with Kopnin mass.

## CONCLUSION

The quantum physical vacuum – the former empty space – is in a reality a richly structured and asymmetric medium. Because this new quantum ether is complicated material with many degrees of freedom, one can learn how to analyze it by studying other such materials – condensed matter [129]. Fermi superfluids, especially  $^3\text{He-A}$ , are the best condensed matter, which provide a rich source for such a modelling. The most pronounced property of  $^3\text{He-A}$  is that in addition to the numerous bosonic fields (collective modes of the order parameter which play the part of the gauge fields in electromagnetic, weak and strong interactions) it contains gapless fermionic quasiparticles, which are similar to the elementary excitations of quantum physical vacuum (leptons and quarks).

It is important that the quantum physical vacuum belongs to the same class of the fermionic condensed matter as  $^3\text{He-A}$ : both contain the topologically stable nodes in the energy spectrum of the fermionic excitations. As a result both fermionic systems display, for example, the gravitational and gauge fields as the collective bosonic modes of the fermionic system. The other fermionic systems belong either to the class, which is characterized by the Fermi surfaces (such as normal metals and normal Fermi liquid), or to the class with the gap in the fermionic spectrum (such as conventional superconductors and  $^3\text{He-B}$ ), while the high-temperature superconductors belong to the marginal class with the topologically unstable lines of gap nodes. Thus  $^3\text{He-A}$  (together with  $^3\text{He-A}_1$ ) remains the only condensed matter frame in which the properties of the physical vacuum can be fully probed, even with laboratory experiments.

Zeroes in the fermionic spectrum, such as Fermi surfaces (surfaces of zeroes) and Fermi points (point zeroes) play an extremely important role in the low-energy physics of the quantum vacuum and condensed matter. In condensed matter, the gapless fermions interacting with the Bose fields of the order parameter lead to the anomalous behavior of superfluids and superconductors at low temperature,  $T \ll T_c$ , such as spectral flow in the vortex dynamics, nonanalytic behavior of the current and gradient energy, nonlinear and nonlocal Meissner effect, etc. The counterpart of this behavior in high energy physics manifests itself in the axial anomaly, baryogenesis, zero charge effect, running coupling constants, photon mass, etc. It is the zeroes in the fermionic spectrum, through which the conversion of the vacuum degrees of freedom into that of the matter takes place.

Similar zeroes, but in the real space, occur in the cores of the topological defects, among which the quantized vortices (cosmic strings in the high energy physics) play an important role. Actually the real-space zeroes and the momentum-space zeroes are described by the same topology extended to the  $8=4+4$ -dimensional space. For example, from the topological point of view the Fermi-surface represents the vortex singularity of the Green's

function in the  $\omega, \mathbf{p}$  space, where  $\omega$  is the Matsubara frequency. The Green's function  $G(\omega, p) = 1/(i\omega + v_F(p - p_F))$  displays a vortex in the  $\omega, p$  plane with the winding number  $\nu = 1$ . This makes the Fermi surface topologically stable and robust under perturbations of the Fermi system. Even though the pole in the Green's function can disappear under some perturbations, the Fermi surface will survive in the marginal and Luttinger superfluids. The latter thus belong to the same class of the Fermi systems as the Landau Fermi-liquid.

In the same manner the gapped superfluids and superconductors behave in the vicinity of the vortex core as superfluid  $^3\text{He-A}$  in bulk. The point gap nodes appear to be the common feature. Due to the common topological origin of point nodes, the fermions near the gap nodes in gapless Fermi superfluids and superconductors and the low energy fermions localized in cores of vortices in conventional gapped superconductors produce similar anomalous effects.

The vortices play an important part not only at low temperature, but also in the physics of the broken symmetry phase transitions. The proliferation of vortex loops with infinite size destroys the superfluid long range order above the phase transition. In the nonequilibrium phase transition from the symmetric nonsuperfluid phase, discussed here, the infinite vortex cluster in the normal state survives after the rapid quench and becomes the origin of the remanent vorticity in the superfluid state. We believe that it is this mechanism, which leads to the observed vorticity in our experiments with neutrons.

## ACKNOWLEDGEMENTS

We are indebted to Yu. Bunkov, A. Gill, H. Godfrin, H.E. Hall, J.R. Hook, T. Kibble, N. Kopnin, A. Leggett, Yu. Makhlin, B. Plaçais, J. Ruohio, V. Ruutu, E. Thuneberg, T. Vachaspati, W. Zurek, and Wen Xu. Much of the work with these colleagues was made possible by a grant from the EU Human Capital and Mobility visitor program (no. CHGECT94-0069). The collaboration has been inspired by the European Science Foundation network on "Topological Defects in Cosmology and Condensed Matter Physics".

- 
- [1] M.J. Geller and J.P. Huchra, *Science* **246**, 897 (1989).
  - [2] 1 Mpc =  $10^6$  parsec =  $3.262 \cdot 10^6$  light years.
  - [3] J. Einasto, M. Einasto, S. Gottlöber, V. Müller, V. Saar, A.A. Starobinsky, E. Tago, D. Tucker, H. Andernach, and P. Frisch, *Nature* **385**, 139 (1997).
  - [4] T.W. Kibble, *J. Phys. A* **9**, 1387 (1976).
  - [5] W.H. Zurek, *Nature* **317**, 505 (1985); *Phys. Rep.* **276**, 177 (1996).

- [6] T. Vachaspati and A. Vilenkin, *Phys. Rev. D* **30**, 2036 (1984); M. Hindmarsh and T. Kibble, *Rep. Progr. Phys.* **58**, 477 (1995); A. Bray, *Adv. Phys.* **43**, 357 (1994).
- [7] I. Chuang, R. Durrer, N. Turok, and B. Yurke, *Science* **251**, 1336 (1991); M.J. Bowick, L. Chandar, E.A. Schiff, and A.M. Srivastava, *Science* **263**, 943 (1994).
- [8] P.C. Hendry, N.S. Lawson, R.A.M. Lee, P.V.E. McClintock, and C.D.H. Williams, *Nature* **368**, 315 (1994).
- [9] M.E. Dodd, P.C. Hendry, N.S. Lawson, P.V.E. McClintock, C.D.H. Williams, *cond-mat/9808117*.
- [10] A.J. Gill and T.W. Kibble, *J. Phys. A: Math. Gen.* **29**, 4289 (1996).
- [11] V.M. Ruutu, V.B. Eltsov, A.J. Gill, T.W. Kibble, M. Krusius, Yu.G. Makhlin, B. Plaçais, G.E. Volovik, and Wen Xu, *Nature* **382**, 334 (1996).
- [12] C. Bäuerle, Yu.M. Bunkov, S.N. Fisher, H. Godfrin, and G.R. Pickett, *Nature* **382**, 332 (1996); *J. Low Temp. Phys.* **110**, 13 (1998).
- [13] T.W. Kibble and G.E. Volovik, *JETP Lett.* **65**, 102 (1997).
- [14] J.S. Meyer and T. Sloan, *J. Low Temp. Phys.* **108**, 345 (1997).
- [15] M. Stockton, J.W. Keto, and W.A. Fitzsimmons, *Phys. Rev. A* **5**, 372 (1971); J.S. Adams, S.R. Bandler, S.M. Brouer, R.E. Lanou, H.J. Maris, T. More, and G.M. Seidel, *Phys. Lett. B* **341**, 431 (1995).
- [16] K.W. Schwarz, *Phys. Rev. B* **38**, 2398 (1988); *B* **31**, 5782 (1985); *B* **18**, 245 (1978).
- [17] R.J. Donnelly, *Quantized Vortices in Helium II* (Cambridge University Press, Cambridge, UK, 1991).
- [18] M. Krusius, E.V. Thuneberg, and Ü. Parts, *Physica B* **197**, 376 (1994).
- [19] Ü. Parts, V.M. Ruutu, J.H. Koivuniemi, Yu.M. Bunkov, V.V. Dmitriev, M. Fogelström, M. Huebner, Y. Kondo, N.B. Kopnin, J.S. Korhonen, M. Krusius, O.V. Lounasmaa, P.I. Soininen, and G.E. Volovik, *Europhys. Lett.* **31**, 449 (1995); V.M. Ruutu, Ü. Parts, J.H. Koivuniemi, N.B. Kopnin, and M. Krusius, *J. Low Temp. Phys.* **107**, 93 (1997).
- [20] D. Vollhardt, P. Wölfe, *The Superfluid Phases of Helium 3* (Taylor & Francis, 1990).
- [21] Wen Xu, B. Plaçais, V.M. Ruutu, and M. Krusius, *Czechoslovak J. Phys.* **46**-Suppl., Part S1, 11 (1996).
- [22] J.S. Korhonen, A.D. Gongadze, Z. Janu, Y. Kondo, M. Krusius, Yu.M. Mukharsky, and E.V. Thuneberg, *Phys. Rev. Lett.* **65**, 1211 (1990).
- [23] V.M. Ruutu, V.B. Eltsov, M. Krusius, Yu.G. Makhlin, B. Plaçais, and G.E. Volovik, *Phys. Rev. Lett.* **80**, 1465 (1998).
- [24] V.M. Ruutu, Ü. Parts, B. Plaçais, Wen Xu, G.E. Volovik, and M. Krusius, *Czechoslovak J. Phys.* **46**-Suppl., Part S1, 15 (1996).
- [25] D.S. Greywall, *Phys. Rev. B* **33**, 7520 (1986).
- [26] Y.H. Tang, I. Hahn, H.M. Bozler, and C.M. Gould, *Phys. Rev. Lett.* **67**, 1775 (1991). The equilibrium AB transition obeys the form  $T_{AB}(P, H) = T_c(P) (1 - \alpha H^2)$ , where  $\alpha(P) \sim (0.5 - 10) \cdot 10^{-6} (\text{mT})^{-2}$ .
- [27] P. Schiffer and D.D. Osheroff, *Rev. Mod. Phys.* **67**, 491 (1995); P. Schiffer, M.T. O'Keefe, M.D. Hildreth, Hiroshi Fukuyama, and D.D. Osheroff, *Phys. Rev. Lett.*

- 69**, 120 (1992).
- [28] Yu. Kagan and B.V. Svistunov, Zh. Exper. Teor. Fiz. **105**, 353 (1994) [Sov. Phys. JETP **78**, 187 (1994)].
  - [29] H. Toyoki, J. Phys. Soc. Japan **63**, 446 (1994); M. Zapotocky, P.M. Goldbart, and N. Goldenfeld, Phys. Rev. E **51**, 1216 (1995).
  - [30] P.E. Schiffer, D.D. Osheroff, and A.J. Leggett, in *Prog. Low Temp. Phys.*, Vol. XIV, p. 159 (Elsevier Science B.V., Amsterdam, 1995), and references therein.
  - [31] A.J. Leggett, J. Low Temp. Phys. **87**, 571 (1992).
  - [32] J.D. Bjorken, Acta Phys. Polon. **B28**, 2773 (1997); G. Amelino-Camelia, J. D. Bjorken, and S. E. Larsson, Phys. Rev. D **56**, 6942 (1997).
  - [33] A. Linde, *Particle physics and inflationary cosmology* (Harwood Acad. Publ., Switzerland, 1990).
  - [34] G.E. Volovik, Czechoslovak J. Phys. **46**-Suppl., Part S6, 3048 (1996).
  - [35] Yu.M. Bunkov and O.D. Timofeevskaya, Phys. Rev. Lett. **80**, 4927 (1998); J. Low Temp. Phys. **110**, 45 (1998).
  - [36] C. Bäuerle, Yu. M. Bunkov, S. N. Fisher, and H. Godfrin, Phys. Rev. B **57**, 14381 (1998).
  - [37] J.C. Wheatley, Rev. Mod. Phys. **47**, 415 (1975).
  - [38] J.T. Tough, in *Prog. Low Temp. Phys.*, Vol. XIII, p. 133 (Elsevier Science B.V., Amsterdam, 1982), and references therein.
  - [39] R.G.K.M. Aarts and A.T.A.M. de Waele, Phys. Rev. B **50**, 10069 (1994).
  - [40] S.K. Nemirovskii and W.M. Fiszdon, Physica B **197**, 290 (1994).
  - [41] D.C. Samuels, Phys. Rev. B **46**, 11714 (1992).
  - [42] M. Tsubota and H. Yoneda, J. Low Temp. Phys. **101**, 815 (1995).
  - [43] T.D.C. Bevan, A.J. Manninen, J.B. Cook, A.J. Armstrong, J.R. Hook, and H.E. Hall, Phys. Rev. Lett. **74**, 750 (1995).
  - [44] J. Koplik and H. Levine, Phys. Rev. Lett. **71**, 1375 (1993).
  - [45] C.F. Barenghi, D.C. Samuels, G.H. Bauer, and R.J. Donnelly, Phys. Fluids **9**, 2631 (1997).
  - [46] N.D. Antunes and L.M. Bettencourt, Phys. Rev. D **55**, 925 (1997).
  - [47] N.B. Kopnin and E.V. Thuneberg, to be published.
  - [48] P. Laguna and W.H. Zurek, Phys. Rev. Lett. **78**, 2519 (1997).
  - [49] J. Dziarmaga, preprint cond-mat/9802213; preprint cond-mat/9803185.
  - [50] L. Onsager, Nuovo Cimento **6**, Suppl. 2, 249 (1949).
  - [51] A. Rajantie, K. Kajantie, M. Karjalainen, M. Laine, J. Peisa, hep-lat/9807042; K. Kajantie, M. Karjalainen, M. Laine, J. Peisa, A. Rajantie, Phys. Lett. **B 428** 334 (1998); A. Rajantie, cond-mat/9803221.
  - [52] N.D. Antunes and L.M.A. Bettencourt, hep-ph/9807248.
  - [53] N.D. Antunes, L.M.A. Bettencourt, M. Hindmarsh, Phys. Rev. Lett. **80**, 908 (1998).
  - [54] A. Yates, and W.H. Zurek, hep-ph/9801223.
  - [55] G.A. Williams, Phys. Rev. Lett. **71**, 392 (1993); J. Low Temp. Phys. **93**, 1079 (1993); cond-mat/9807338.
  - [56] B. Chattopadhyay, M.C. Mahato, S.R. Shenoy, Phys. Rev. **B 47**, 15159 (1993).
  - [57] D.R. Nelson and J.M. Kosterlitz, Phys. Rev. Lett. **39**, 1201 (1977).
  - [58] J.C. Le Guillou and J. Zinn-Justin, Phys. Rev. **B 21**, 3976 (1980); D.Z. Albert, Phys. Rev. **B 25**, 4810 (1982).
  - [59] L.S. Goldner and G. Ahlers, Phys. Rev. **B 45**, 13129 (1992); J.A. Lipa, D.R. Swanson, J.A. Nissen, T.C.P. Chui and U.E. Israelsson, Phys. Rev. Lett. **76**, 944 (1996).
  - [60] J.A. Lipa, J.A. Nissen, D.R. Swanson, P.R. Williamson, K. Geng, D.A. Stricker, T.C.P. Chui and U.E. Israelsson, "Early Results from the Confined Helium Experiments", Talk at QFS98 - Symposium on Quantum Fluids and Solids, June 9 - 14, 1998, University of Massachusetts, Amherst, MA, USA, Abstract #12-S9.
  - [61] G. Karra, and R.J. Rivers, hep-ph/9804206.
  - [62] T.D.C. Bevan, A.J. Manninen, J.B. Cook, J.R. Hook, H.E. Hall, T. Vachaspati, and G.E. Volovik, Nature, **386**, 689 (1997).
  - [63] T.D.C. Bevan, A.J. Manninen, J.B. Cook, H. Alles, J.R. Hook, and H.E. Hall, J. Low Temp. Phys. **109**, 423 (1997).
  - [64] A.D. Dolgov, Rep. Prog. Phys. **222**, 309 (1992).
  - [65] N. Turok, in *Formation and interaction of topological defects*, eds. A.C. Davis and R. Brandenberger (Plenum Press, New York, 1995), p. 283-301.
  - [66] E. Witten, Nucl. Phys. B **249**, 557 (1985).
  - [67] T. Vachaspati and G.B. Field, Phys. Rev. Lett. **73**, 373 (1994); **74**, 1258 (1995).
  - [68] J. Garriga and T. Vachaspati, Nucl. Phys. B **438**, 161 (1995).
  - [69] A. Roberge, *Finite Density Effects in Gauge Theories*, Ph. D. thesis, University of British Columbia (1989).
  - [70] T. Vachaspati, in *Proc. NATO Workshop "Electroweak Physics and the Early Universe"*, Sintra, Portugal (1994), Series B: Physics Vol. 338 (Plenum Press, New York, 1994).
  - [71] M. Barriola, Phys. Rev. D **51**, 300 (1995).
  - [72] G.D. Starkman, Phys. Rev. D **53**, 6711 (1996).
  - [73] M. Joyce and M. Shaposhnikov, Phys. Rev. Lett. **79**, 1193 (1997).
  - [74] M. Giovannini and E.M. Shaposhnikov, Phys. Rev. Lett. **80**, 22 (1997).
  - [75] V.M.H. Ruutu, J. Kopu, M. Krusius, U. Parts, B. Plačais, E.V. Thuneberg, and W. Xu, Phys. Rev. Lett. **79**, 5058 (1997).
  - [76] M. Krusius, T. Vachaspati, and G.E. Volovik, preprint cond-mat/9802005.
  - [77] S. Adler, Phys. Rev. **177**, 2426 (1969).
  - [78] J.S. Bell and R. Jackiw, Nuovo Cim. **A60**, 47 (1969).
  - [79] C. Caroli, P.G. de Gennes, and J. Matricon, Phys. Lett. **9**, 307 (1964).
  - [80] G.E. Volovik, JETP Lett. **57**, 244 (1993).
  - [81] N.B. Kopnin, G.E. Volovik, and Ü. Parts, Europhys. Lett. **32**, 651 (1995).
  - [82] N.B. Kopnin, Phys. Rev. B **47**, 14354 (1993).
  - [83] M. Stone, Phys. Rev. B **54**, 13222 (1996).
  - [84] G.E. Volovik and T. Vachaspati, Int. J. Mod. Phys. B **10**, 471 (1996).
  - [85] G.E. Volovik, Pis'ma ZhETF **62**, 58 (1995) [JETP Lett.

- 62**, 65 (1995)].
- [86] R.L. Davis and E.P.S Shellard, Phys. Rev. Lett. **63**, 2021 (1989).
  - [87] K.-M. Lee, Phys. Rev. D **49**, 4265 (1994).
  - [88] G.E. Volovik and T. Vachaspati, Int. J. Mod. Phys. B **10**, 471 (1996); G.E. Volovik, preprint cond-mat/9802091.
  - [89] E.B. Sonin, Phys. Rev. B **55**, 485 (1997).
  - [90] C. Wexler, Phys. Rev. Lett. **79**, 1321 (1997).
  - [91] A. Shelankov, preprint cond-mat/9802158.
  - [92] S.V. Iordanskii, Ann. Phys. **29**, 335 (1964); ZhETF **49**, 225 (1965) [JETP, **22**, 160 (1966)].
  - [93] E.B. Sonin, ZhETF **69**, 921 (1975); [JETP **42**, 469 (1976)].
  - [94] P.O. Mazur, Phys. Rev. Lett. **57**, 929 (1986).
  - [95] D. Harari and A.P. Polychronakos, Phys. Rev. D **38**, 3320 (1988).
  - [96] P.O. Mazur, Phys. Rev. Lett. **59**, 2380 (1987).
  - [97] P.O. Mazur, preprint hep-th/9611206.
  - [98] W. G. Unruh, Phys. Rev. D **14**, 870 (1976); **51**, 2827 (1995).
  - [99] A. Staruszkiewicz, Acta Phys. Polon. **24**, 734 (1963).
  - [100] S. Deser, R. Jackiw, and G. 't Hooft, Ann. Phys. **152**, 220 (1984).
  - [101] B. Jensen and J. Kuvcera, J. Math. Phys. **34**, 4975 (1993).
  - [102] B. Jensen and H.H. Soleng, Phys. Rev. D **45**, 3528 (1992).
  - [103] G.N. Glushchenko, ZhETF **104**, 273 (1995); [JETP **80**, 145 (1995)].
  - [104] G.E. Volovik, Low Temp. Phys. (Kharkov) **24**, 127 (1998).
  - [105] R.M. Cleary, Phys. Rev. **175**, 587 (1968).
  - [106] Y. Aharonov and D. Bohm, Phys. Rev. **115**, 485 (1959).
  - [107] D.V. Gal'tsov and P.S. Letelier, Phys. Rev. D **47**, 4273 (1993).
  - [108] A.L. Fetter, Phys. Rev. **136A**, 1488 (1964).
  - [109] E. Demircan, P. Ao, and Q. Niu, Phys. Rev. B **52**, 476 (1995).
  - [110] K.S. Thorne, J.B. Hartle, Phys. Rev. D **31**, 1815 (1985); Y. Mino, M. Sasaki, and T. Tanaka, preprint gr-qc/9705073.
  - [111] N.B. Kopnin, G.E. Volovik, and Ü. Parts, Europhys. Lett. **32**, 651 (1995).
  - [112] G.E. Volovik, *Exotic Properties of Superfluid  $^3\text{He}$* , World Scientific, Singapore, 1992.
  - [113] R.L. Davis, Physica **B 178**, 76 (1992).
  - [114] H-c Kao and K. Lee, hep-th/9503200; R. Iengo, and G. Jug, cond-mat/9506062.
  - [115] J.M. Duan, Phys. Rev. Lett. **75**, 974 (1995).
  - [116] C. Wexler and D. J. Thouless, cond-mat/9612059
  - [117] N.B. Kopnin, Pis'ma ZhETF, **27**, 417 (1978); [JETP Lett., **27**, 390 (1978) ].
  - [118] N.B. Kopnin and M.M. Salomaa, Phys. Rev. **B 44**, 9667 (1991).
  - [119] N. B. Kopnin and G. E. Volovik, Phys. Rev. **B 57**, 8526-8531 (1998).
  - [120] A. van Otterlo, M.V. Feigel'man, V.B. Geshkenbein, and G. Blatter, Phys. Rev. Lett. **75**, 3736 (1995).
  - [121] G.E. Volovik, Pis'ma ZhETF **65**, 201 (1997) [JETP Lett. **65**, 217 (1997)].
  - [122] E.B. Sonin, V.H. Geshkenbein, A. van Otterlo and G. Blatter, Phys. Rev. **B 57**, 575 (1998).
  - [123] G. Baym and E. Chandler, J. Low Temp. Phys. **50**, 57 (1983).
  - [124] G.E. Volovik and V.P. Mineev, ZhETF **83**, 1025 (1982) [JETP **56**, 579 (1982)].
  - [125] M.M. Salomaa and G.E. Volovik, Rev. Mod. Phys. **59**, 533 (1987)
  - [126] T.D.C. Bevan, A.J. Manninen, J.B. Cook, J.R. Hook, H.E. Hall, T. Vachaspati and G.E. Volovik, Nature, **386**, 689 (1997).
  - [127] N.B. Kopnin, Physica **B 210**, 267 (1995).
  - [128] G.E. Volovik, in: *Helium Three*, eds. W.P. Halperin, L.P. Pitaevskii, Elsevier Science Publishers B.V., p. 27, 1990.
  - [129] F. Wilzcek, Physics Today, January 1998, 11.